EPFL

Thèse n° 8834

Enhancing mitochondrial quality control to fight neuromuscular degeneration in aging and disease

Présentée le 19 février 2021

Faculté des sciences de la vie
Chaire Nestlé en métabolisme énergétique
Programme doctoral en biotechnologie et génie biologique

pour l'obtention du grade de Docteur ès Sciences

par

Mario ROMANI

Acceptée sur proposition du jury

Prof. H. Lashuel, président du jury
Prof. J. Auwerx, directeur de thèse
Prof. A. Dillin, rapporteur
Prof. R. Houtkooper, rapporteur
Prof. J. Feige, rapporteur

École
polytechnique
fédérale
de Lausanne

2021

They are rage, *brutal*, *without mercy. But you...you will be worse. Rip and tear until it is done*

Acknowledgments

First of all, I am grateful to my advisor, Prof. Johan Auwerx. I thank him for giving me the chance to perform my doctoral work in his group. Importantly, he has taught me commitment and persistence to attain any goal in life. These lessons will undoubtedly help me for all my future pursuits. I would also like also to thank Prof. Kristina Schoonjans for her support and encouragement throughout my Ph.D.

My deepest gratitude goes to Dr. Vincenzo Sorrentino, my supervisor during my master project in the Auwerx lab and then during my Ph.D. time. Vincenzo is like a brother to me, he invested a tremendous amount of time in making me the scientist I am proud to be. Together we became the forerunners of the proteostasis research in the Auwerx lab, we achieved what was believed to be impossible by many, and we did that by working to our limit but always with passion and a smile on our faces.
Beside Vincenzo, I am grateful to have had the chance to be guided during the initial phases of my Ph.D. by other talented researchers who are now well established scientists. In particular, I would like to thank Dr. Davide D'Amico, Dr. Pedro M. Quirós, Dr. Olli Matilainen for sharing their deep knowledge of molecular biology with me.

A very, very special thank goes to Nadia Bresciani, who was with me through many happy adventures but more importantly during difficult times. I would not be here delivering my thesis without her, I will never be able to thank her enough for her support.

I would like to thank also the so called KN members of the lab Francesca Potenza, Pirkka-Pekka Untamo Laurila, Giovanni Sorrentino, Dina Bonazzoli, Melanie Korbelius and Marika Zi for their great attitude and contribution to the cheerful atmosphere that characterized the first years of my experience in the Auwerx lab. I am grateful to also the KN members outside of the lab, Francesco Cosentino, Simone Bonazzoli, Serena Manganelli, Alexander Ter Beek and all the others.

Ph.D. life is a tough life, but luckily I had great Ph.D. fellows fighting alongside me. I would like to thank Alexis Bachmann, with who I shared my time in the lab as both master and doctoral student. Sharing our thoughts and difficult experiences over a beer at Satellite was always very liberating and fun, I am looking forward to do the same for our future working experiences. A big thank goes to Martin Rainer Wohlwend who motivated me inside and outside of the lab, his commitment to science and sport was a great inspiration for me.

A special thank goes to the former lab manager of the Auwerx lab, Dr. Norman Moullan, for his positive attitude and his way of turning difficult situations into easy ones; but more importantly for having been my running buddy for my whole Ph.D.

I am grateful to have had the opportunity to share lab space with colleagues from the Deplancke lab. In particular, I would like to thank Marian Biocanin for the amazing events we attended together and for his personal playlist that characterized late hours in the lab for many years.

I would also like to thank the ADSV (association of Ph.D. students in SV) for which I served as communications officer for 4 years. With them I had the chance to become the coordinator of the SV Happy hours through which I meet great scientists working next door who are now wonderful friends. Having the responsibility of connecting the whole faculty through this social event was a big challenge, but it was also very rewarding.

Coming to the end, I want to thank my family for their consistent love and support. They have always believed in me and gave me the means to come to Switzerland and achieve my goals. Their advises and encouragement were pivotal in reaching this milestone.

Table of Contents

Summary

Loss of mitochondrial function and proteostasis typify aging and age-associated degenerative disorders such as Alzheimer's disease and muscle aging. To date, no cure or preventive measure is available to manage these conditions. Alterations of cellular proteostasis, such as accumulation of misfolded or aggregated proteins, can directly affect mitochondrial homeostasis leading to activation of specific mitochondrial stress pathways capable of maintaining mitochondrial function. However, the contribution of these pathways in age-associated diseases characterized by proteotoxic aggregates is largely unknown. My thesis aims to understand the connection between cellular and mitochondrial proteostasis with a particular focus on mitochondrial stress pathways involved in the response to proteotoxic stress. To this end, I performed 2 studies:

***Reduction of Amyloid-beta proteotoxicity through activation of mitochondrial quality control*:** Accumulation of Amyloid-beta (Aβ) peptidic aggregates, generated by the miscleavage of amyloid precursor protein (APP), is often associated with mitochondrial dysfunction. However, it is largely unknown how mitochondria react to these proteotoxic insults. We identified a cross-species conserved mitochondrial stress response, from nematodes to humans, activated during Aβ proteotoxic stress. This response entails key mitochondrial quality control pathways such as the mitochondrial unfolded protein response (UPR^{mt}) and mitophagy. Importantly, activation of these pathways through administration of mitochondrial regulators Doxycycline and the NAD^+ booster nicotinamide riboside (NR), was sufficient to reduce Aβ accumulation and proteotoxicity in nematodes and human cell lines. Moreover, boosting mitochondrial quality control *in vivo* in a mouse model of Alzheimer's disease with the compound NR led to a reduction of brain Aβ plaques and preservation of cognitive function.

***Skeletal muscle aging is characterized by amyloid-like protein aggregates*:** Skeletal muscle aging is characterized by accumulation of dysfunctional mitochondria and misfolded proteins. However, the connection between these two hallmarks of muscle aging remains elusive. We found that aged skeletal muscles present a similar perturbation of mitochondrial and APP processing pathways when compared to muscles from inclusion body myositis patients (IBM), a disease characterized by intracellular protein deposits containing also Aβ aggregates. In line with this, we identified amyloid-like aggregates in aged muscle closely resembling the ones observed during IBM with concomitant mitochondrial dysfunction. Strategies aiming at restoring mitochondrial homeostasis led to activation of the mitochondrial quality control accompanied by a reduction of amyloid-like aggregates *in vitro* and *in vivo* in mammalian and nematode systems.

In summary, our work demonstrated that amyloidosis characterizes muscle, and possibly brain, aging in a similar fashion to what is observed in muscle and brain tissues from IBM and Alzheimer's patients, respectively. Importantly, restoring mitochondrial homeostasis through activation of mitochondrial quality control is sufficient to alleviate protein aggregation and improve tissue function in aging, IBM and Alzheimer's disease models.

***Keywords*:** Mitochondria, NAD^+, Aging, Mitochondrial quality control, Amyloidosis, Inclusion Body Myositis, Skeletal Muscle, Brain, Proteostasis, Nicotinamide Riboside

Sommario

La perdità di attività mitocondriale e proteostasi caratterizzano il processo di invecchiamento e malattie degenerative associate ad invecchiamento come il morbo di Alzheimer e invecchiamento dei muscoli. Ad oggi, nessuna cura o misura di prevenzione è disponibile per gestire queste condizioni. Alterazioni della proteostasi cellulare, come accumulazione di proteine mal ripiegate o aggragate, possono impattare direttamente sull'omeostasi mitocondriale portando all'attivazione di specifici pathway di stress mitocondriale capaci di mantenere la funzione mitocondriale. Tuttavia, il contributo di questi pathway in malattie associate all'invecchiamento caratterizzate da aggregati proteici tossici è in gran parte sconosciuto. La mia tesi ha lo scopo di caratterizzare la connessione fra proteostasi cellulare e mitocondriale con un'attenzione particolare a pathway di stress mitocondriale coinvolti nella risposta a stress proteotossico. A questo scopo, ho svolto 2 studi di ricerca:

***Riduzione della proteotossicità di beta-amiloide attraverso l'attivazione del controllo qualità mitocondriale*:** Accumulazione di aggregati di peptide beta-amiloide (Aβ), generati dall'errato clivaggio della proteina precorritrice della beta-amiloide (APP), sono spesso associati a disfunzione mitocondriale. Tuttavia, è in gran parte sconosciuto come i mitocondri reagiscono a questi insulti proteotossici. Abbiamo identificato una risposta mitocondriale allo stress conservata fra specie, da nematode a uomo, attivata durante stress proteotossico da Aβ. Questa risposta comprende pathway chiave di controllo qualità mitocondriale fra cui la risposta mitocondriale a proteine malripiegate (UPR^{mt}) e la mitofagia. È importante sottolineare che l'attivazione di queste risposte allo stress attraverso la somministrazione del modulatore mitocondriale Doxycycline e del booster di NAD^+ nicotinamide riboside (NR), è stata sufficiente a ridurre l'accumulazione e la proteotossicità di Aβ in nematodi e linee cellulari umane. Inoltre, il potenziamento del controllo qualità mitocondriale *in vivo* in un modello murino di morbo di Alzheimer usando il composto NR ha portato alla riduzione di placche Aβ cerebrali e alla preservazione della funzione cognitiva.

***L'invecchiamento dei muscoli scheletrici è caratterizzato da aggregati proteici simil-amiloide*:** L'invecchiamento dei muscoli scheletrici è caratterizzato da accumulazione di mitocondri disfunzionali e proteine mal ripiegate. Tuttavia, la connessione fra questi due segni distintivi dell'invecchiamento dei muscoli rimane da approfondire. Abbiamo scoperto che muscoli scheletrici invecchiati presentano una simile perturbazione dei pathway mitocondriali e di processamento di APP quando paragonati a muscoli di pazienti affetti da miosite dell'inclusione (IBM), una malattia caratterizzata da depositi proteici intracellulari composti anche da aggregati di Aβ. In linea con ciò, abbiamo identificato aggregati simil-amiloide in muscoli invecchiati paragonabili a quelli osservati nella IBM con una concomitante disfunzione mitocondriale. Strategie atte a ripristinare l'omeostasi mitocondriale hanno portato all'attivazione del controllo qualità mitocondriale accompagnato da una riduzione di aggregati simil-amiloide *in vitro* e *in vivo* in mammiferi e nematodi.

In sintesi, il nostro lavoro ha dimostrato che l'amiloidosi caratterizza l'invecchiamento dei muscoli, e probabilmente del cervello, in modo simile a quanto osservato in muscoli e tessuto nervono affetti da IBM e morbo di Alzheimer rispettivamente. È importante sottolineare che il ripristino dell'omeostasi mitocondriale attraverso l'attivazione del controllo di qualità mitocondriale è sufficiente ad alleviare l'aggregazione proteica e a migliorare la funzione dei tessuti durante l'invecchiamento, ma anche in modelli di IBM e morbo di Alzheimer.

Chapter 1

Partially adapted from:

Romani M, Hofer DC, Katsyuba E, Auwerx J. *Niacin: an old lipid drug in a new NAD+ dress*. J. Lipid Res. 2019 Apr;60(4):741-746. doi: 10.1194/jlr.S092007

Aging and mitochondria

Mankind has long struggled with the fear of aging and the helplessness in preventing its progression. Legends and stories dealing with ways to maintain youth and pursue eternal life can be found in any culture throughout history, from the holy grail in Christian religion[1], to the fountain of youth[2], obsession of Ponce de León, or the philosopher's stone of Albertus Magnus and Nicholas Flamel[3], and again in Asian culture from the Penglai (mount of the immortals) hidden in the eastern seas of China[4], to the Amrita, the drink of the Indian gods Devas which grants them immortality[5]. Today, thanks to scientific progress, we have stronger basis to study the aging process and to better understand how to slow it down, moving from fantasy and religious basis to a more solid scientific based approach supported by scientific evidence.

The physiological background of human aging has been subject to 300 theories.[6] The majority of them can be classified to three main categories, wear and tear, genetic, and accumulation of cellular waste, yet there is significant overlap even between these categories. The *wear and tear hypothesis*, stating that the body and its cells are damaged by overuse and abuse, is perhaps the oldest aging theory, firstly introduced by Dr. Weissman in 1982, and five years later defined at the cellular level by Warner and colleagues[7]. Like components of a machine, body parts eventually wear out from repeated use. The *genetic theory* of aging proposes that aging follows a precise chronological sequence of events, most likely driven by the same forces that govern development and growth; this process can be accelerated with the introduction of errors in the DNA altering the aging rhythm. Finally, the *cellular waste theory* implies that damaged molecules and their byproducts along with dysfunctional organelles accumulate in cells (especially postmitotic ones) causing cell dysfunction and death in a process also known as "Garb-aging"[8]. This could be caused by both increased production of molecular garbage or decreased clearance activity. In the frame of these hypotheses, **mitochondria** play a crucial role in aging, by being both pivotal during development and youth, and major players in the aging process when they become dysfunctional and virtually involved in all the categories mentioned above[9,10].

Mitochondria are essential components of eukaryotic cells providing them with 90% of the chemical energy (in the form of ATP) they need to survive through oxidative phosphorylation (OXPHOS); moreover, they contribute to cellular metabolism, calcium homeostasis and apoptosis. In turn, mitochondria depend on the proteins encoded by the nuclear DNA of the host cells to be fully functional. However, this symbiotic relationship has not always been present. It is believed that more than 1.45 billion years ago an *alpha-proteobacterium* was engulfed by a primordial eukaryotic cell closely related to *Asgard* archaea[11]. The initial benefit of this symbiosis was probably the production of hydrogen by the endosymbiont as a source of energy and electrons for the archaebacterial host, which is believed to have been hydrogen dependent[12]. Such symbiotic interaction is common in modern microbial communities. This primary endosymbiotic event gradually led to a refined evolutionary process producing the vital cellular organelle, known as the present-day mitochondrion, allowing oxidation to harvest energy in a milieu where oxygen was produced through photosynthesis. Detailed understanding of this billion-year-long symbiotic relationship can provide vital insights to better understand the aging process of eukaryotic organisms, and how to slow it down.

Age-related mitochondrial dysfunction

Abundant literature has described an age-dependent impairment of mitochondrial function across species from yeast to humans, which in return contributes to age-associated cellular quality control decline and tissue dysfunction[13,14]. Aged mitochondria display decreased

transport of metabolites and import of nuclear encoded mitochondrial proteins. This, in return, leads to decreased respiration rates and impaired OXPHOS, the primary source of energy for the cells. This contributes to increased reactive oxygen species (ROS) production with consequent cell toxicity as suggested by the genetic and waste theories of aging. Beside functional decline, aged mitochondria are also characterized by structural changes, such as alterations of cristae structure, important for the OXPHOS process to take place, matrix vacuolization or densification, and a general size enlargement[15]. While impairment in mitochondrial function is a global hallmark of aging, there are tissues in which it is more prominently observed than others. These typically include post mitotic and highly metabolic tissues, such as skeletal muscle and brain, which are therefore more sensitive to dysregulation of mitochondrial-mediated processes.

Indeed, age-dependent mitochondrial dysfunction has been extensively studied in skeletal muscle from human and different model organism. Muscle aging is often accompanied by a reduction in subunits of the protein complexes that compose the OXPHOS machinery (i.e. complex I, II, and IV) and of respiratory enzyme activity (i.e. citrate synthase (CS))[16], followed by accumulation of ROS[17,18], and a drop in the respiration rate (i.e. oxygen consumption)[19,20], oxidative capacity and ATP synthesis[21]. In return, these detrimental features of aged muscle mitochondria contribute to the onset of age-associated muscle diseases, such as sarcopenia or inclusion body myositis (IBM)[22–24].

Similar to muscle, the brain largely consists of postmitotic cells which require a high energy production to sustain their metabolic activity; for this reason mitochondria are present in many copies within neurons and are pivotal for their function[25,26]. Age-associated mitochondrial dysfunction can therefore partially explain the deterioration of this tissue in eldery and the onset of age-related diseases linked with a decline in cognitive performance. In fact, postmortem analysis of different human brain regions revealed an age-associated downregulation of anti-oxidant proteins such as superoxide dismutase (SOD), reduced mitochondrial bioenergetics and OXPHOS complexes[27]; whereas, mitochondria from aged rats brains displayed reduced membrane potential and electron transport, impaired anti-oxidant defenses and increased opening of the mitochondrial transition pore[28,29], a condition associated with cell death in many neurodegenerative diseases.

With our increasing understanding of the neuromuscular aging process, it is now evident that also different environmental factors, such as lifestyle and nutrition, can have an impact and modulate the aging process in order to attenuate age-associated mitochondrial dysfunction. This is in line with the 3 hypotheses of aging, mentioned above, that reducing tissue tearing and waste accumulation could beneficially impact on aging.

Interestingly, while muscular and brain mitochondrial content and activity is strongly reduced in sedentary old people, physically active aged individuals preserve functional mitochondria. In particular, mitochondrial gene expression of cytochrome c oxidase (COX) subunits, CS activity, ATP production, as well as mitochondrial DNA (mtDNA) copy number are maintained in both brain and skeletal muscle of elderly individuals upon physical exercise[30–34]. In fact, a wide range of beneficial effects is known to be induced following physical activity, with a predominant one being an increased mitochondrial biogenesis in many tissues of our body, including in muscles and brain. Generation of new mitochondria relies on the key transcription factor peroxisome proliferator-activated receptor gamma coactivator 1-alpha (PCG1α) which modulates the activity of downstream mediators, such as TFAM and NRF proteins, which mediate mitonuclear communication and nuclear promoters activation[35]. Interestingly, PGC1α overexpression is sufficient to prevent age associated muscle dysfunction contributing to the maintenance of mitochondrial copy number and normalization of mitochondrial dynamics[36,37], suggesting a causal link between

mitochondrial content and function and skeletal muscle pathology. Mitochondrial biogenesis is also crucial for the maintenance of neuronal function, and PGC1α dysregulation has been associated with many age-associated brain diseases including Alzheimer's (AD), Huntington's (HD) and Parkinson's disease (PD)[38].

Progressive age-dependent tissue dysfunction can also be explained by decreased regenerative capacity. In many tissues, this ability relies on tissue-specific stem cells and their ability to activate differentiation, when needed, in response to specific signals[39]. The long-lived nature of these cells makes them susceptible to age-related insults in line with the wear and tear model and the waste accumulation theory of aging, leading to a decrease in their proliferation, differentiation capacity and total number[40]. In fact, dysfunctional mitochondria are considered a hallmark of senescence of muscle stem cells (MuSC) and neural stem cells (NSC)[41,42]. There is evidence that specific metabolic intermediates play an important role in regulating the transcriptional and epigenetic states of stem cells. Importantly, chromatin modifications are largely dependent on the same carbon intermediates (for example methyl, acetyl, etc.) which are generated during normal mitochondrial metabolism[43]. Mitochondrial homeostasis is therefore essential to maintain stem cell function and age-dependent impairment of mitochondrial function is thought to be one of the leading causes of cell death and reduced proliferation in stem cells.

In addition to the examples above describing how mitochondrial play a role in the wear and tear model and the waste accumulation theories, the *genetic theory* of aging suggests that mutations in DNA can affect the aging process; unlike any other cellular organelle, mitochondria have their own genome, being predisposed to mutations. As such, mitochondria are also central players in the genetic theory of aging. Knock-in mice that express a proof-reading-deficient version of PolgA (MtDNA mutator mice), the nucleus-encoded catalytic subunit of mtDNA polymerase[44,45] helped to establish the contribution of mitochondrial genetics to the aging process. MtDNA mutator mice present high levels of point mutations, as well as increased amounts of deleted mtDNA. This increase in somatic mtDNA mutations is associated with reduced lifespan and premature onset of age-related phenotypes. Not surprisingly, mtDNA mutator mice present brain atrophy and decreased muscle strength and mass. Notably, stem cells depletion is a common feature of these tissues in the mutator mice closely resembling the aging phenotype[46]. This model established for the first time a causal link between mtDNA mutations and aging; however, whether mitochondrial heteroplasmy (i.e. the accumulation of mutated mitochondrial sequences) reaches significant levels in tissue upon natural aging is still under debate. Indeed, mtDNA is present in a large number of copies within cells, and the load of mutated mitochondria should exceed 60% of the total mitochondrial population in order to display a significant phenotype.

Age-associated diseases - Neuromuscular amyloid disorders

Age-associated diseases are a group of various complex disorders affecting different tissues of human body, whose major risk factor is aging. These pathologies often share molecular alterations typical of the aging process such as decreased proteasomal[47] and autophagic activity[48,49], increased protein aggregation[50], over-activation of the inflammation process[51], cellular senescence[52], oxidative stress[53] and importantly, mitochondrial dysfunction[54,55].

Amyloidoses are systemic proteotoxic diseases that may be acquired or be inherited. Deposition of amyloid aggregates in a variety of tissues, including brain and skeletal muscle is a hallmark of amyloidiosis, causing progressive dysfunction of the affected organs and

contributing to the pathogenesis of diseases like AD and IBM[56], as described in the chapter above. It is estimated that the best-known age-associated proteotoxic disease in the brain, AD, affects 44 million people globally and costs 604 billion USD per year[57]. AD is characterized by progressive brain atrophy and memory loss which correlates with accumulation of misfolded proteins[58]. IBM, the most common proteotoxic muscle disease, affects 25 per 1 million[59], with a three-fold increased prevalence in the population over 50 years old[60]. However, the reported prevalence is constantly increasing over time thanks to growing awareness of the disease and improvements in diagnosis[59]. Typifying features of this disorder are progressive muscle wasting and weakness associated with pathological intracellular protein aggregates[61]. While the etiology of these disorders is incompletely understood, genetic and environmental factors are involved in the disease pathogenesis and progression[62–66]. Amyloidosis is therefore an example of a process in which the wear and tear, genetic, and waste accumulation theories of aging can coexist and explain age-associated tissue pathology.

The amyloid-β (Aβ) peptide is the main component of amyloid plaques, extracellular deposits that characterize also AD, and inclusion bodies, typical intracellular aggregates in IBM muscles (Figure 1.1). Aβ is derived by the proteolytic cleavage of amyloid precursor protein (APP) (Figure 1.1), a protein mainly expressed in the brain but that can be detected also in skeletal muscle[67], skin[68], adipose tissue[69] and intestine[70]. The amyloidogenic pathway mediates the generation of aggregation prone Aβ peptides, and is catalyzed by two membrane-bound group of enzymes, β-secretase (entailing β-secretase 1 and 2) and γ-secretase, which include presenilin 1 (PS1; encoded by the *PSEN1* gene) and PS2 (encoded by the *PSEN2* gene) (Figure 1.1). In line with the afore mentioned theories of aging, mutations of APP and presenilin genes characterize familial forms of AD and contribute to the generation of amyloidogenic Aβ peptides[71]. However, despite the characterization of an age-dependent decline of Aβ turnover[72], hence increased likelihood to aggregate, the exact nature of how aging impacts the production and clearance of APP and Aβ is yet to be fully understood. APP can also be processed by α-secretase through the non-amyloidogenic pathway which produces non-toxic fragments, and is thought to antagonize Aβ generation (Figure 1.1). APP occupies several subcellular locations, including the plasma membrane, the endoplasmic reticulum (ER), the Golgi, and the mitochondria[73–76]. Accordingly, the proteotoxic effects of Aβ mirror the subcellular distribution of its precursor causing dysfunction in several cellular organelles[77,78].

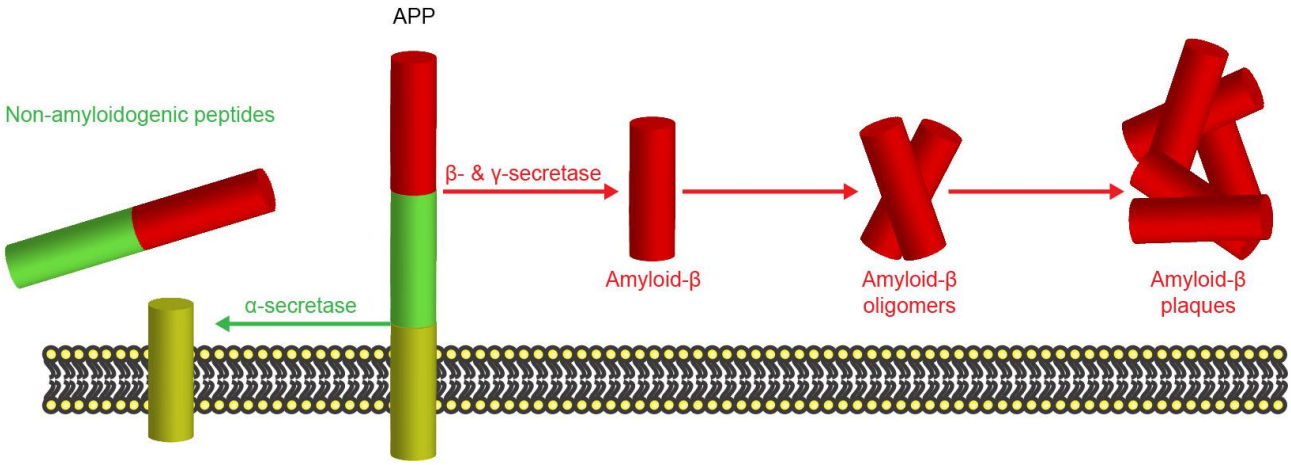

Fig. 1.1 | During the non-amylodoigenic processing (green), APP is cleaved by α-secretase leading to formation of peptides which are not susceptible to aggregation. On the other hand, APP processing through the amyloidogenic pathway (red) is mediated by β- & γ-secretase sequentially, with consequent generation of Aβ peptides. This small aggregation-prone peptide has the ability to diffuse in different cell locations and through the affected tissue generating oligomers which can further migrate. Aβ oligomers can assemble in Aβ plaques which, differently from the monomeric and oligomeric form, are insoluble with consequent deposition and cell/tissue damage.

Amyloidosis and mitochondria

The majority of Aβ peptides is generated within the ER and Golgi compartments and further processed in lysosomal vesicles[79]. Importantly, after their production in these organelles, Aβ accumulates in other cell compartments, such as in mitochondria as observed in brains from AD mouse models and post-mortem human AD brain samples; this occurs even before Aβ plaques form[80–82]. It is therefore not surprising that amyloid-β disorders are generally characterized by a strong mitochondrial impairment, which in return plays a critical role in the pathogenesis of amyloidosis. In fact, the interaction of Aβ peptides and aggregates with mitochondria and their accumulation within these organelles at different levels can trigger mitochondrial conformational and functional changes (Figure 1.2), including enhanced ROS production, reduction of their activity, initiation of the apoptosis cascade, altered mitochondrial dynamics and quality control.

Mitochondria are highly dynamic organelles which continuously fuse and divide during two processes called mitochondrial fusion, mediated by the OPA1 and MFN1/2 proteins[83], and fission, mediated by DRP1[84,85], respectively. Mitochondrial dynamics are pivotal to respond to mitochondrial damage, as they mediate the rescue of non-functional organelles by fusion and elimination of damaged organelles after fission. However, dysregulated fusion and fission have been associated with mitochondrial dysfunction and cell death in many pathologies, including neuromuscular diseases[24,86,87]. Interestingly, levels of DRP1, MFN1/2 and OPA1 are altered in *in vitro* and *in vivo* models of amyloidosis including human neuroblastoma cell lines overexpressing an aggregation-prone form of APP (APP_{Swe}), mouse models of AD and in patients with AD and IBM[24,87–91] (Figure 1.2). Despite not having reached a consensus on whether the balance is tilted towards fusion or fission *in vivo*, mostly because of the heterogeneity of the models used and the stages of the disease analyzed, strong *in vitro* evidence suggest rather an accumulation of small and fragmented mitochondria, typical of ongoing fission in amyloidosis. Mitochondria from either primary hippocampal neurons treated with soluble Aβ oligomers, or APP_{Swe}-expressing neuroblastoma cells, are significantly more fragmented then their control counterparts[92,93]. Importantly, *in vitro* overexpression of OPA1, but not DRP1, partially restores Aβ-induced mitochondrial dysfunction[88]. Of note, impairment of mitochondrial dynamics is also a predominant hallmark of other proteinopathies and neurodegenerative diseases, including Parkinson's disease (PD), autosomal dominant optic atrophy and Charcot-Marie-Tooth neuropathy type 2A[94,95].

Mitochondria depend on the cellular translation machinery for synthesis of the vast majority of their proteome. For this reason, a vital component for mitochondrial function is the mitochondrial protein import system, composed by the translocase of the outer mitochondrial membrane (TOM) and the translocase of the inner mitochondrial membrane (TIM). As for mitochondrial dynamics, the mitochondrial transport system can also be impaired by amyloid proteotoxicity (Figure 1.2). The acidic domain of APP and Aβ can form a stable complex with the TOM and TIM proteins *in vitro*, which prevents its internalization within the mitochondria while promoting accumulation in the mitochondrial import channels[96]. Importantly, the APP-TOM/TIM association has also been observed in human AD brain samples, where it was coupled to reduced mitochondrial activity and reduced protein transport[97]. Reduced mitochondrial protein import due to the interaction of APP or Aβ with mitochondrial translocases could contribute to mitochondrial dysfunction by reducing import of nuclear encoded OXPHOS subunits. It is in fact not surprising that different nuclear-encoded components of the ETC, such as complex I and IV, are downregulated in two different AD mouse models[98,99] and in IBM patients[24], with consequent alteration of respiratory supercomplexes formation[100]. Interestingly, these defects were observed even before accumulation of plaques in the brain, supporting the notion that APP and Aβ can interact

directly with mitochondria and affect their function[99]. Accordingly, free Aβ triggers the appearance of vacuolated muscle fibers, a typical pathological feature of IBM, in patients before the formation of protein aggregates[101].

In line with evidence suggesting an accumulation of Aβ on the outer mitochondrial membrane and its interaction with key mitochondrial proteins during AD, such as TIM and TOM as mentioned above, APP and Aβ are also capable of directly interacting with the voltage-dependent anion channel (VDAC) (Figure 1.2). Being the most abundant protein on the mitochondrial outer membrane, VDAC constitutes the main gatekeeper for passage of metabolites, nucleotides and ions from the cytoplasm to the intermembrane space. In line with reduced mitochondrial transport of metabolites, components of the tricarboxylic acid (TCA) cycle, including pyruvate dehydrogenase (PDH) and α-ketoglutarate dehydrogenase (KGDH), which rely on VDAC, among other transporters, for substrate uptake, display reduced activity in postmortem brain tissues of AD-affected subjects[102] (Figure 1.2).

Beside its role in metabolites transportation, VDAC is involved in the formation of the mitochondrial permeability transition pore (mPTP) together with other important mediators such as Cyclophilin D (CypD) located in the mitochondrial matrix and adenine nucleotide translocase (ANT), which anchors to the mitochondrial inner membrane (MIM)[103]. This protein complex is generated when CypD associates with the inner membrane, leading to the binding of ANT; this complex further connects with VDAC, creating a pore on the mitochondrial surface which leads to the loss of membrane potential, swelling and, ultimately, the rupture of outer mitochondrial membrane leading to release of factors causing apoptosis[104]. Of note, CypD is upregulated in a time-dependent manner in temporal lobes and hippocampi of AD human patients and of transgenic mouse models[105]. Moreover, CypD binding with Aβ strongly promotes its translocation to the MIM, activating the apoptotic cascade (Figure 1.2). Importantly, CypD ablation was sufficient to significantly reduce Aβ proteotoxicity and restore cognitive and synaptic function in a mouse model of Alzheimer's disease[105,106].

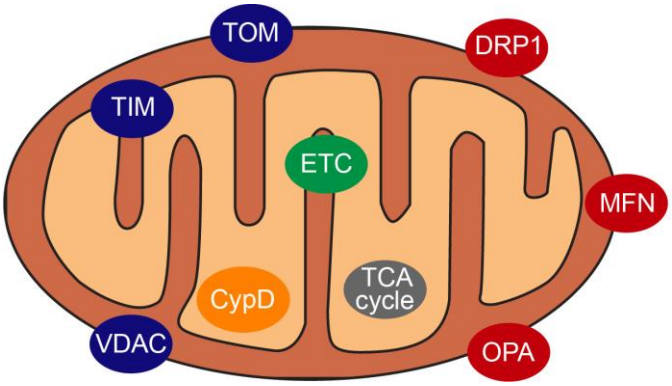

Fig. 1.2 | Aβ can affect mitochondrial homeostasis binding different targets ultimately leading to decreased mitochondrial function. Aβ perturbs important mediators of mitochondrial dynamics (red) such as DRP1, MNF1/2 and OPA1 with consequent altered mitochondrial morphology. Aβ can also interact with mitochondrial transport machinery (blue) such as TOM, TIM and VDAC. As a consequence of this interaction these mitochondrial channels are blocked, jeopardizing transport of pivotal mitochondrial proteins and substrates involved in the electron transport chain (ETC) (green) and mitochondrial metabolism (grey). Finally, Aβ binding to apoptosis mediating protein CypD (orange) promotes mPTP formation with consequent disruption of mitochondrial membrane and apoptosis. TCA, tricarboxylic acid.

NAD^+ and amyloidosis

Mitochondria are a central hub of many transcriptional and metabolic pathways due to their role in energy metabolism. Aβ peptides and aggregates can affect these organelles and consequently cell metabolism not only by directly interacting with them, but also by affecting upstream processes depleting essential metabolites and cofactors needed for correct mitochondrial function and regulation.

NAD^+ synthesis

NAD^+ is a crucial metabolite for mitochondrial metabolism and altered NAD^+ homeostasis typifies different disease states including neuromuscular degenerative disorders. NAD^+ can be produced from different forms of vitamin B3, which include nicotinamide (NAM), nicotinic acid (NA) and nicotinamide riboside (NR)[107] through the "salvage pathway". All these molecules are known as "NAD^+ precursors." Alternatively, NAD^+ can be synthetized via the de novo synthesis (DNS) pathway, from the essential amino acid tryptophan.

NA is converted into NA mononucleotide (NAMN) by nicotinate phosphoribosyltransferase (NAPRT) in the first step of the Preiss-Handler pathway[108] (Figure 1.3). NAM mononucleotide adenylyltransferase (NMNAT) uses NAMN to generate NA adenine dinucleotide (NAAD), which gets converted into NAD^+ by NAD synthetase (NADS) (Figure 1.3). NAD^+ synthesis from NAM and NR comprises their conversion into NAM mononucleotide (NMN) by NAM phosphoribosyltransferase (NAMPT) and NAM riboside kinase (NRK), respectively, and the subsequent conversion of NMN into NAD^+ by NMNAT (Figure 1.3). NMNAT is, therefore, common to all branches of the NAD^+ synthesis pathways fueled by vitamin B3 precursors. Interestingly, NMNAT activity has been associated with amyloid proteins formation (e.g. Aβ, Tau, and α-syn), preventing their aggregation and cytotoxicity[109–111]. It is not surprise therefore that NMNAT plays a protective role for neurons in Wallerian degeneration, a condition considered an early hallmark preceding neuronal death in many disorders of the nervous system, including AD and PD, ischemic brain and spinal cord injuries, diabetic neuropathy, traumatic brain injury (TBI) and ALS[112,113]. In a similar manner, NAMPT, the rate-limiting enzyme in the conversion of NAM to NAD^+, delays the occurrence of axonal degeneration and protects against paclitaxel-induced peripheral neuropathy[114], while its impairment is linked to proteotoxic neurodegeneration[115]. Of note, a neurogenesis-enhancing compound, P7C3[116], which is neuroprotective in a mouse model of PD[117] (Table 1) was later shown to be a NAMPT activator[118]. P7C3 also protects against the onset of ALS[119], TBI[120] and AD[121,122] (Table 1), all conditions tightly associated with Wallerian degeneration.

The NAD^+ DNS pathway consists of 7 steps, all but one of which are catalyzed by an individual enzyme (Figure 1.3). The single non-enzymatic reaction is the spontaneous cyclisation of α-amino-β-carboxymuconate-ε-semialdehyde (ACMS) into quinolinic acid (QA). Interestingly, besides being transformed into QA, ACMS can also be decarboxylated by ACMS decarboxylase (ACMSD) (Figure 1.3). Since the conversion of ACMS into QA occurs spontaneously, the proportion of ACMS leading to NAD^+ is determined by the activity of ACMSD[123,124]. If QA is formed, it is converted into NAMN by quinolinate phosphoribosyltransferase (QPRT), which then feeds into the Preiss-Handler pathway. Dysregulation of the DNS and tryptophan catabolism characterizes different brain areas of patients affected by neurodegenerative diseases mediated by cytotoxic protein aggregation, including AD, PD and HD[125–128]. Moreover, altered activation of the DNS in central nervous system-resident macrophages mediates aberrant immune stimulation hence contributing to the development of age-associated neurodegenerative diseases[129].

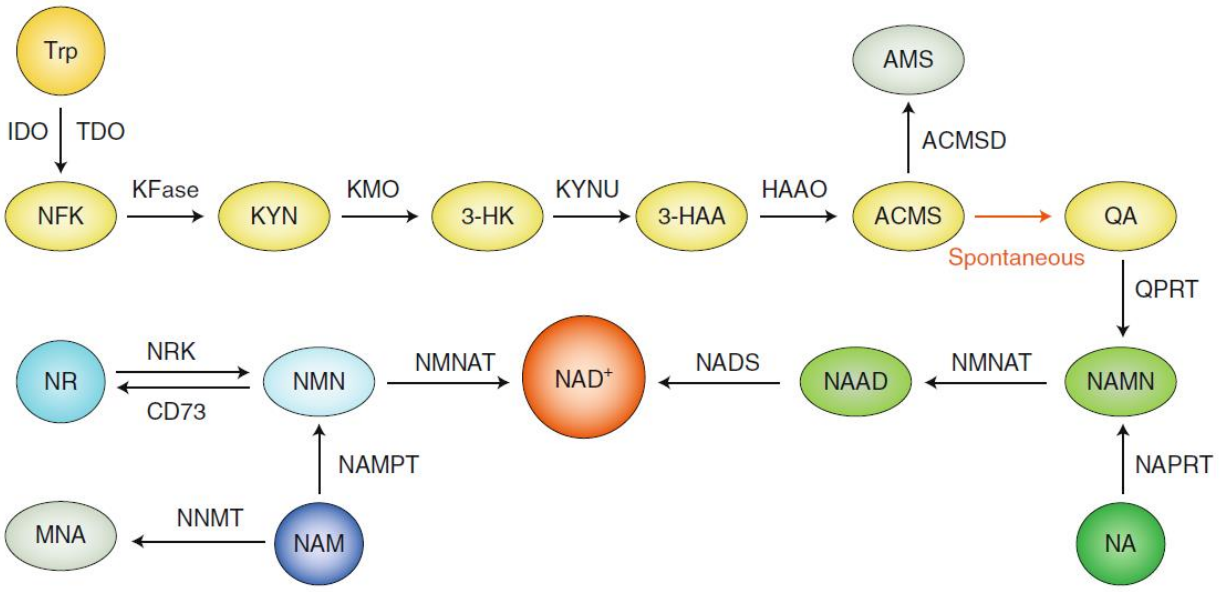

Fig. 1.3 | NAD^+-biosynthesis pathways. NAD^+ biosynthesis can be accomplished through different routes: it can be produced either *de novo* from the essential amino acid tryptophan (Trp) (yellow) or via salvaging, starting from different naturally occurring forms of vitamin B_3—nicotinic acid (NA) (green), nicotinamide riboside (NR) (light blue) and nicotinamide (NAM) (dark blue). The first reaction of de novo NAD^+ biosynthesis opens the indole ring of tryptophan and is catalysed by either indoleamine-2,3-dioxygenase (IDO) or tryptophan-2,3-dioxygenase (TDO). Four consecutive enzymatic steps lead to production of 2-amino-3-carboxymuconate-6-semialdehyde (ACMS), which is then transformed into quinolinic acid (QA) in the unique non-enzymatic reaction of the de novo pathway. ACMS can otherwise be decarboxylated by ACMS decarboxylase (ACMSD), thus limiting the proportion of ACMS transformed into QA. QPRT catalyses the conversion of QA into NA mononucleotide (NAMN), which is also an intermediate in the Preiss–Handler pathway (green). In the Preiss–Handler pathway, NA is converted into NAD^+ via three consecutive enzymatic reactions catalysed by NA phosphoribosyltransferase (NAPRT), NMN/NAMN adenylyltransferase (NMNAT) and NAD synthetase (NADS), respectively. The two remaining salvaging routes, starting either from NR or NAM, share the common intermediate NAM mononucleotide (NMN), which is generated by NR kinase (NRK) or NAM phosphoribosyltransferase (NAMPT), respectively. NAM can otherwise be methylated by NAM *N*-methyltransferase (NNMT). AMS, 2-aminomuconic-6-semialdehyde; CD73, ecto-5′-nucleotidase; 3-HAA, 3-hydroxyanthranilic acid; HAAO, 3-hydroxyanthranilic acid dioxygenase; 3-HK, 3-hydroxykynurenine; KFase, kynurenine formamidase; KMO, kynurenine 3-monooxygenase; KYN, kynurenine; KYNU, kynureninase; NAAD, NA adenine dinucleotide; NFK, *N*-formylkynurenine; MNA, 1-methyl-nicotinamide.

NAD^+ consuming enzymes

NAD^+ is an essential co-factor for a variety of biochemical reactions, acting as an electron acceptor in these reactions. Many reactions that require NAD^+ as a coenzyme are linked to catabolism and harvesting of metabolic energy: NAD^+, serves a cofactor for enzymes involved in **i)** alcohol metabolism (alcohol and aldehyde dehydrogenases), **ii)** glycolysis (glyceraldehyde phosphate dehydrogenase), **iii)** oxidative decarboxylation of pyruvate to acetyl-CoA (pyruvate dehydrogenase), **iv)** fatty acid β-oxidation (3-hydroxyacyl-CoA dehydrogenase) and **v)** TCA cycle enzymes function (α-ketoglutarate, isocitrate- and malate dehydrogenases). NAD^+ also acts as a cofactor for lactate dehydrogenase (LDH) in the liver during the Cori cycle.

NAD^+ also acts as co-substrate for the sirtuin family of deacylases (SIRTs) and thereby effectively coordinates a number of crucial mitochondrial processes including mitophagy, OXPHOS, fatty acid oxidation, mitochondrial biogenesis and quality control. Sirtuins remove an acyl-group from their substrate using NAD^+ as a cosubstrate; thereby generating the deacylated substrate, 2-O-acyl-ADP-ribose (2-OAADPR) and nicotinamide (NAM) as end-products (Figure 1.4).

Dysregulation of components of this protein family has been linked to different disorders such as nonalcoholic fatty liver disease, diabetes, Duchenne muscular dystrophy, IBM, and PD [130–132]. A robust decrease in SIRT1 levels also correlates with the accumulation of proteotoxic aggregates and severity of cognitive decline in parietal cortex of AD patients, monkeys and mice[133–136]. Importantly, *in vitro* and *in vivo* induction of SIRT1, through genetic

overexpression or interventions such as calorie restriction, exercise and resveratrol treatment, ameliorates proteotoxicity in different degenerative diseases[132,137–141], while its repression during amyloidosis worsens Aβ pathology in mice[142]. Of note, activity of SIRT1 is also diminished in muscle during IBM, resulting in exacerbated Aβ accumulation in muscle fibers[131]. This is in line with the protective role of SIRT1 in AD and further implies a shared NAD^+ and sirtuin-dependent mechanism.

Decreased SIRTs activity could be in fact a direct effect of NAD^+ depletion, which characterizes amyloidosis diseases such as AD and IBM[143–145], and NAD^+ depletion is often the result of increased NAD^+ processing. Indeed, besides SIRTs, other important NAD^+ consuming enzymes have been identified, such as the cyclic ADP-ribose (cADPR) synthases and the poly-ADP-ribose polymerase (PARP) protein family, and their implication in neuromuscular disease models investigated

cADPR synthases, whose most prominent member, CD38, is expressed ubiquitously, use NAD^+ to produce cADPR (Figure 1.4), an important cellular regulator of Ca^{2+} homeostasis[146]. Interestingly, CD38-deficient mice have up to 30-fold higher NAD^+ levels in tissues[147], and in line with a protective role of NAD^+ in neurodegeneration, the AD model APP/PS1 mutant transgenic mice lacking CD38 display diminished Aβ accumulation and corrected learning and memory[148]. Recently, an increase in CD38 positive cells has been characterized in IBM patients and proposed as biomarker of this disease[149]

PARPs are responsible for PARylation, a reversible post-transcriptional protein modification, in which a large polymer of ADP-ribose moieties is added to a target protein, accompanied by NAD^+ hydrolysis into NAM (Figure 1.4). PARylation mediates a number of cellular processes including DNA repair[150], chromatin reorganization[151] and apoptosis[152]. The main NAD^+ consumer among the PARPs is PARP1, which alone accounts for 90% of all NAD^+ used by the PARP family[153]. In contrast to sirtuin family proteins, PARPs activity seems not to be affected by fluctuations in NAD^+ levels, as the Km values for NAD^+ are far below the physiological range of NAD^+. Thus, PARPs have an advantage over sirtuins when competing for limiting NAD^+ resources[153]: NAD^+ availability would become rate-limiting for sirtuin activity in situations when PARPs are overactivated, as observed during aging or upon DNA damage[154–157]. Oxidative stress, exacerbated by proteotoxic damage-mediated mitochondrial dysfunction, has been linked to accumulation of DNA damage. It is therefore not a surprise that PARP1 was found to be strongly induced in brain tissues from AD, HD and ALS patients[158–161]. Consistently, genetic induction of protein aggregation or injection of proteotoxic peptides *in vivo* also promoted PARP1 activation, while administration of PARP inhibitors alleviated proteotoxic stress in AD mouse models[162].

Sterile alpha and TIR motif–containing 1 (SARM1) is an important NAD^+ consumer in neurons. The dimerization of its TIR domain consumes NAD^+, generates mostly NAM and ADPR, but also small amounts of cADPR[163,164] (Figure 1.4). NAD^+ depletion caused by SARM1 is tightly associated with axonal destruction or Wallerian degeneration[165]. Unsurprisingly, preserving the NAD^+ pool was sufficient to protect axons from degeneration and alleviate conditions associated with axonal degeneration, including various peripheral neuropathies, ischemic brain or spinal cord injury (Table 1).

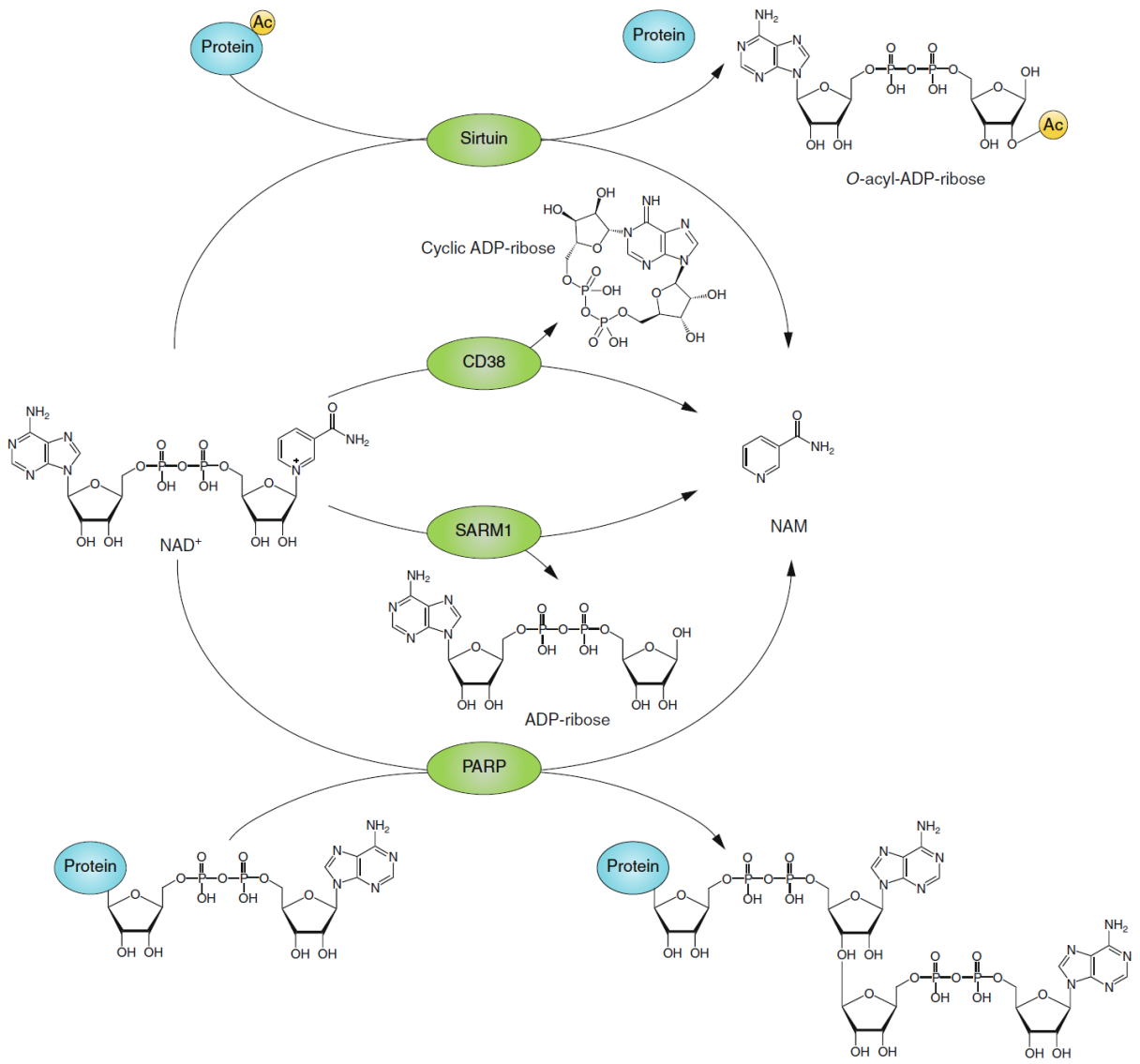

Fig. 1.4 | The main NAD$^+$-consuming enzymes. NAD$^+$ serves as a cosubstrate for a variety of enzymes with crucial roles in metabolism, ageing and cell survival. Arrows indicate reactions mediated by NAD$^+$-consuming proteins (green). Molecular structures are represented for the initial and end products, along with by-products of each reaction. Comprising seven proteins in humans, the sirtuin family of enzymes mediates deacylation of several important proteins. The reactions catalysed by sirtuins involve removal of an acyl group (such as acetyl, malonyl, succinyl, crotonyl or propionyl) from the substrate, thus resulting in the generation of *O*-acyl-ADP-ribose with concomitant consumption of NAD$^+$. NAD$^+$ in turn is hydrolysed into nicotinamide (NAM). PARPs are another important group of NAD$^+$ consumers. During the PARylation reaction catalysed by PARPs, multiple ADP-ribosyl groups are attached to protein substrates, and NAD$^+$ is hydrolysed into NAM. The third group of NAD$^+$-consuming enzymes is represented by cyclic ADP ribose synthases, which regulate calcium homeostasis. CD38 catalyses the generation of cyclic ADP-ribose by using NAD$^+$, which is converted into NAM. The TIR domain of SARM1 drives the cleavage of NAD$^+$ into NAM and ADP-ribose (and cyclic ADP-ribose to a lesser extent), thus qualifying the TIR-domain-containing proteins as a family of NAD$^+$ consumers. Ac, Acyl.

NAD$^+$ boosting strategies

NAD$^+$ depletion is a hallmark of aging and numerous age-related disorders, from neuro-muscular[130,166–168] to cardiometabolic[169,170], liver[171,172] and kidney diseases[173,174]. For this reason, the therapeutic and preventive potential of NAD$^+$ boosting has been scrutinized in a variety of preclinical models and disease settings (Table 1, 2). The promising outcomes of these studies have triggered a series of clinical trials, which are at present testing the efficacy of NAD$^+$ therapeutics also in human diseases.

Strategies to promote an increase in NAD$^+$ levels broadly fall into two categories: stimulation of its synthesis or inhibition of excessive NAD$^+$ consumption[175,176].

Several strategies can be adopted to promote NAD$^+$ synthesis:

i) Supplementation with NAD^+ precursors is efficient *in vitro* and *in vivo*, including in nematodes, flies, rodents[177] and, most importantly, humans (Table 1, 2). Dihydronicotinamide riboside (NRH) has been recently reported as another biochemical precursor for NAD^+, which induced strong NAD^+ increase in different mammalian cell lines and mouse tissues[178].

ii) NAD^+ production can also be enhanced by stimulation of enzymes involved in NAD^+ synthesis (Figure 1.3): both overexpression of NAMPT[179,180] and its activation with pharmacological enhancers, such as P7C3[118] or SBI-797812[181] translate into an increase in NAD^+ content, positively impacting on Wallerian degeneration and associated neurodegenerative diseases [117,119–122]. Similarly, overexpression of another NAD^+ synthetic enzyme, NMNAT, demonstrated comparable proteotoxicity protective effects[112,113,168,182,183].

iii) NAD(P)H-quinone oxidoreductase 1 (NQO1) is an antioxidant that uses NADH as an electron donor hence raising cellular NAD^+ levels. Overexpression of NQO1 mimics different aspects of caloric restriction, including modest lifespan extension[184]. Moreover, chemical activation of NQO1 increases intracellular NAD^+ levels and protects from various diseases, including chemotherapy-induced nephrotoxicity, cardiac dysfunction, acute pancreatitis, intestinal damage, lung fibrosis, hearing loss and PD[185–192].

(iv) The most recent wave of approaches to stimulate NAD^+ production is based on the principle of preventing the escape of intermediates from the NAD^+ biosynthetic pathway. This method can be illustrated by two enzymes: ACMSD and NAM N-methyltransferase (NNMT). As already mentioned earlier, ACMSD catalyses the reaction at the branching point of the de novo NAD^+ synthesis and therefore acts as a gatekeeper controlling the dissipation of a pathway intermediate ACMS into the side branch (Figure 1.3). Accordingly, mice overexpressing human ACMSD and maintained on vitamin B3-free diet have reduced NAD^+ levels and neurological symptoms similar to humans with NAD^+-deficiency[124]. Conversely, downregulation and pharmacological inhibition of ACMSD efficiently increased NAD^+ levels in C. elegans, as well as in mouse livers and kidneys[123,193].
Similar to ACMSD, NNMT catalyses a reaction removing a precursor molecule from the path normally leading to the production of NAD^+. But in case of NNMT it acts on the salvage pathway, i.e. NNMT N-methylates NAM to produce 1-methylnicotinamide (MNA) (Figure 1.3), which cannot be used for NAD^+ synthesis anymore. Knockdown[194] and pharmacological inhibition of NNMT[195,196] both lead to an increase in NAD^+ content.

(v) Due to their low Km for NAD^+, PARP-1 and CD38 have the capacity to strongly deplete cellular NAD^+ stores in situations when they become overactivated, typically aging and proteotoxic diseases (Figure 1.4). Both pharmacological and genetic PARP inhibition raise NAD^+ levels with beneficial effects on metabolic health and longevity[155,197–202]. Similarly, NAD^+ levels are substantially increased by genetic or pharmacological CD38 inhibition[201,203–209]. Another NAD^+ consumer, SARM1, has been extensively studied in the context of Wallerian degeneration (Figure 4). NAD^+ depletion caused by SARM1 activation leads to axonal destruction[165]. SARM1 loss-of-function was hence reported to restore NAD^+ content depleted by nerve transection and protect axons[210].

Supplement	**Pathological condition**	**Health benefits/effects**	**Ref.**
NR (250-400 mg/kg/d) NAM (40-500 mg/kg/d) NMN (500 mg/kg) P7C3 (10-20 mg/kg) Calorie restriction	AD	↓ Amyloid-β aggregates, ↑ synaptic plasticity and neuronal survival, ↑ BDNF levels, ↑ SIRT1 activity, ↓ oxidative stress, ↓ apoptosis, ↓ PARP-1 activity	211–217
P7C3 and P7C3A20 (5-40 mg/kg/d)	PD	Protection of dopaminergic neurons from MPTP-mediated cell death	117

P7C3 (20 mg/kg) NR (400 mg/kg/d)	ALS	Protection of ventral horn spinal cord motor neurons from cell death, ↑ motor function	119,167
NAD^+ (30 mg/kg/d)	Prion disease	↓ Prion protein neurotoxicity	218
NR (400 mg/kg/d)	Spinocerebellar Ataxia Type 7	↓ Motor dysfunction, ↓ Neuronal abnormalities, ↑ Lifespan	219
NR (200 mg/kg/d)	Peripheral neuropathy	↓ Tactile hypersensitivity, ↓ escape-avoidance behaviors	220
NR (300 mg/kg/d)	Diabetic peripheral neuropathy	↑ Motor and sensory neuron conduction velocity and intraepidermal nerve fibers	221
NAD^+ (50-100 mg/kg) NAM (125-500 mg/kg) NU1025 (1-3 mg/kg) 4-ANI (1-3 mg/kg)	Ischemic injury Spinal cord injury	↓ Neuronal death	222–227
P7C3-S243 (3-30 mg/kg/d)	Traumatic brain injury	↓ Axonal degeneration, ↑ synaptic activity, ↑ learning and memory, ↑ motor coordination	228

Table. 1 | Therapeutic potential of NAD^+ boosters in rodent models of proteotoxic disease or related conditions. Abbreviations: AD, Alzheimer's disease; ALS, amyotrophic lateral sclerosis; PD, Parkinson's disease.

Supplement	Dose	Pathological condition	Health benefits/effects	Ref.
Stabilized NADH	12 mg / d / 6m	Probable AD patients	↑ Cognitive function, ↑ MDRS, ↑ verbal fluency, ↑ visual-constructional ability and abstract verbal reasoning	229
NA	250 mg / d / 45d	PD	↑ Motor and cognitive function, ↑ sleep, normalization of GPR109A, ↑ NAD/NADP ratio	230
	1 g / d / 3m	PD	↑ Routine activities and motor function, ↓ rigidity	231
	From 250 mg / d up to 1 g / d	Mitochondrial myopathy	↑ Muscle performance	232
NAM	3 g / d / 6m	Mild/moderate AD	No adverse effects, no effect on cognitive function	233
Acipimox	250 mg / 4x / 1d	Hypopituitary patients	↓ Parasympathetic tone	234
EH301	1200 mg / d / 4m-1y	ALS	↓ ALS progression, ↑ ALSFRS-R score, ↑ Muscle strength, weight and function	235

Table 2 | Therapeutic potential of NAD^+ boosters in diseases of the neuro/muscular system in humans. Abbreviations: AD, Alzheimer's disease; ALS, amyotrophic lateral sclerosis; PD, Parkinson's disease.

Mitochondrial quality control

Enhancing NAD^+ levels has pleiotropic effects on cellular homeostasis as NAD^+ acts as central player in many cellular processes as mentioned. Given the link between NAD^+ levels and SIRTs, NAD^+ boosting strategies' the main outcome of NAD^+ boosting strategies is an improvement of mitochondrial homeostasis. NAD^+ and SIRTs are responsible for generation of new mitochondria, for modulation of their activity and for the maintenance of their function through activation of the mitochondrial quality control pathways activated in response to stress which entails UPR^{mt} and mitophagy[155,236–238].

Mitochondrial unfolded protein response (UPR^{mt})

The mitochondrial proteome is composed of ~1500 proteins, encoded by both mitochondrial and nuclear genomes[239]. Mitochondrial homeostasis is maintained through an equilibrium between proteins made in these two cellular compartments that is fundamental for the correct function of complexes and supercomplexes of the ETC. Thirteen indispensable

proteins of the ETC and part of the machinery necessary for their synthesis are encoded by the mitochondrial DNA[240], but the majority of the mitochondrial proteins are encoded by the nucleus and have to be transported to the mitochondria. Consequently, the correct cross talk between nucleus and mitochondria is vital to coordinate transcription, translation, translocation, and import of mitochondrial proteins, and to ensure mitochondrial proteostasis. When this communication and equilibrium is jeopardized by alterations of OXPHOS, impairment of mitochondrial transport, reduced expression of mitochondrial proteases, or reduction or inhibition of translation by disrupted mitochondrial ribosomal proteins, the cell can experience mitochondrial and cytosolic stress due to accumulation of misfolded mitochondrial proteins within these two cell compartments. One of the mechanisms triggered to restore mitochondria, and consequently cytosolic, homeostasis is the activation of a nuclear transcriptional response that includes the increased expression of mitochondrial proteases and chaperone proteins, the mitochondrial unfolded protein response (UPR^{mt}) (Figure 1.5).

In the last two decades, it became possible to characterize the mechanism of UPR^{mt} activation through genetic and biochemical approaches, mainly in the nematode model *C. elegans*. In this organism, the main transcription factor involved in the activation of the UPR^{mt} is the activating transcriptional factor associated with stress-1 (ATFS-1) (Figure 1.5). This protein, a member of the bZIP transcription factor family, harbors a nuclear localization sequence (NLS) and an amino-terminal mitochondrial targeting sequence (MTS). Under physiological conditions, the latter is dominant, therefore allowing mitochondria to successfully import ATFS-1, leading to its degradation through the matrix-localized protease Lon (Figure 1.5). On the other hand, when mitochondria are perturbed, the NLS becomes dominant due to defective ATFS-1 import into the mitochondria, driving the nuclear localization of the transcription factor. This results in transcriptional activation of the UPR^{mt} genes (Figure 1.5). This arrangement allows cells to evaluate the function of the mitochondrial network using mitochondrial protein import efficiency as a surrogate. The UPR^{mt} response entails mainly genes involved in proteostasis such as chaperones and proteases, which are activated to restore mitochondrial homeostasis. The UPR^{mt} is also accompanied by the activation of genes involved in glycolysis, suggesting an involvement of this stress response in the adaptation of cell metabolism to face mitochondrial stress. Interestingly, ATFS-1 is capable of binding OXPHOS genes promoters modulating directly the production of respiratory components to cope with stressed mitochondrial environment[241]. Finally, different genes involved in mitochondrial import and detoxification, such as *tim-23* and *skn-1*[242,243], are induced by ATFS-1. These genes eventually restore physiologic conditions in the mitochondria and cells by shutting off the stress response.

In worms, UPR^{mt} activation appears to require several additional factors besides ATFS-1, including the mitochondrial protease ClpP, the inner mitochondrial membrane transporter HAF-1, the homeobox transcription factor DVE-1, and the ubiquitin-like protein UBL-5 (Figure 1.5). ClpP is activated upon accumulation of misfolded proteins in the mitochondrial matrix. Speculations about the targets of ClpP protease activity are largely based on the bacterial ClpP which is likely an ancestor of the mitochondrial ClpP. This protease can degrade proteins to small peptides in association with auxiliary chaperones[244]. Although their exact nature is yet to be defined, it is known that the peptides generated by the protease activity of ClpP are transported to the cytosol through the ATP-binding cassette, HAF-1, to initiate the UPR^{mt} signal[245]. Next to this translocation of ClpP cleavage products to the cytosol, nuclear translocation of transcription factor DVE-1 and co-factor UBL-5 are also required to mediate chromatin remodeling which facilitates ATFS-1 binding to its chaperone targets[246]. Interestingly, while RNAi targeting *dve-1* and *ubl-5* only partially impairs the UPR^{mt}, *clpp-1* and *haf-1* RNAis completely blunted UPR^{mt} activation, placing them upstream

of this mitochondrial stress response[246]. Finally, two jumonji domain histone demethylases, JMJD-3.1 and JMJD-1.2, are necessary and sufficient for UPR^{mt} activation, underlining the importance of chromatin remodeling during this stress response[247].

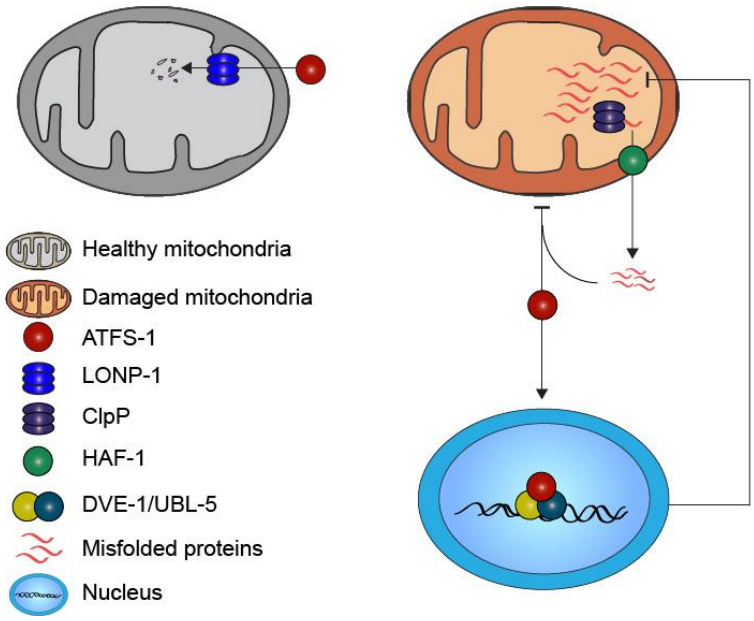

Fig. 1.5 | In basal state ATFS-1 is imported in the mitochondria where it is degraded by the mitochondrial LONP-1. However, upon accumulation of misfolded proteins in the mitochondria ATFS-1 import is jeopardized. These misfolded proteins are processed by the mitochondrial protease ClpP generating peptides which are exported into the cytoplasm through the HAF-1 transporter. Cytosolic presence of these peptides prevents ATFS-1 from entering the mitochondria and therefore promotes its translocation in the nucleus. Here, ATFS-1 interacts with UBL-5 and DVE-1 inducing expression of chaperones and proteases that ultimately restore mitochondrial proteostasis.

The mammalian UPR^{mt}, which was identified thanks to pioneer work using chemical-induced mitochondrial stress[248] or overexpression of aggregation prone mutant ornithine transcarbamylase (ΔOTC), is far more complex than its nematode counterpart, however some of the key mediators modulating this response are evolutionally conserved across species. Indeed, a major role in mammalian UPR^{mt} activation is played by a bZIP transcription factor, ATF-5, which harbors an MTS similar to that of ATFS-1. During mitochondrial stress ATF-5 is required to ensure the activation of a gene signature, that includes chaperones and proteases, and closely resembles the ATFS-1-mediated stress signature[249]. Of note, ATF-5 expression in nematodes lacking functional ATFS-1 restored their ability to activate the UPR^{mt}, suggesting an evolutionary conserved role for this transcription factor[249]. Much like ATFS-1, ATF-5 was required for cardioprotective effects mediated by the UPR^{mt} following administration of mitochondrial stressors such as the ATPase inhibitor, oligomycin, and the mitochondrial translation inhibitor, doxycycline, both known activators of this stress response[250]. ATF-5 activity is mediated by both CHOP and ATF-4[251,252]. The role of CHOP in the UPR^{mt} underlines the importance of this protein in predisposing the cell to face proteotoxic stress, as it is also involved in activation of the integrative stress response (ISR). During mitochondrial proteotoxic stress phosphorylation of the eukaryotic initiation factor alpha (eIF2α), involved in the ISR, enhances synthesis of mRNA containing uORFs in the 5′ UTR. Not surprisingly, ATF-5/4 and CHOP mRNAs molecules accommodate different ORFs making their translation promoted during mitochondrial stress.

Despite extensive characterization, the exact physiological role of the UPR^{mt} in disease is yet to be fully understood. For this reason, deep investigation is currently ongoing to define the involvement of this stress pathway in different disorders; this will also be the focus following chapters of this thesis.

Mitophagy

Autophagy is a physiological process involved in the recycling of the cellular components. During autophagy, organelles, as well as endogenous and xeno proteins, are engulfed into autophagosomes which are then fused and degraded within the lysosomes[253]. This vital process is tightly linked to the ubiquitin-proteasome system (UPS). In fact, while UPS is involved in the degradation of peptides and partially misfolded proteins, autophagy is restricted to the cytoplasm, but is capable of degrading a much wider spectrum of substrates, which, on average, tend to be longer-lived and bulkier. These include functional or misfolded soluble proteins, protein complexes, oligomers and aggregates. Although limited, there appears to be a certain overlap in function between UPS and autophagy, as both seem to be capable of degrading soluble misfolded polypeptide chains[254].

Mitophagy is a peculiar form of autophagy through which cells regulate the number of mitochondria and eliminate the dysfunctional ones. Indeed, while the UPR^{mt} mediates repair of damaged mitochondria, mitophagy coordinates their removal and digestion if damage from proteotoxic stress accumulates to a level that exceeds the capacity of the UPR^{mt} [255]. This process can be performed in an ubiquitin-dependent or independent way (Figure 1.6).

Ubiquitin-dependent mitophagy relies on two key proteins, PINK1 and Parkin. PINK1 is a protein kinase that undergoes proteolytic cleavage in the mitochondria in which it is transported under physiological conditions. If mitochondria suffer for stress or damages, PINK1 is stabilized, due to depolarization, on the outer mitochondrial membrane (Figure 1.6). Here, following the PINK-mediated phosphorylation of the ubiquitin localized on the outer membrane proteins, it recruits the E3 ubiquitin ligase Parkin[256]. The binding between phospho-ubiquitin and Parkin activates its latent E3 ubiquitin ligase activity, ensuring a further ubiquitination of the mitochondrial outer membrane and leading to the formation of the mitophagosome (Figure 1.6). Furthermore, different proteins involved in the autophagy process contribute to the PINK1 and Parkin-mediated mitophagy, such as optineurin and nuclear dot protein 52 and ubiquitin-binding protein p62, which operate as recruiting platforms for autophagy-initiating factors and for anchoring ubiquitinated mitochondria to LC3[257] driving autophagosome assembly around individual damaged mitochondria (Figure 1.6). The main effectors of the *ubiquitin-independent mitophagy* are the receptors BCL2/adenovirus E1B 19-kDa protein interacting protein 3 (BNIP3), NIP3-like protein X (NIX), and FUN14domain–containing 1 (FUNDC1) (Figure 1.6). These proteins are localized on the outer membrane of the mitochondria where they interact directly with LC3 and GABARAP bypassing PINK1 and Parkin to promote mitochondrial degradation.

In addition, mitophagy is linked through different molecular mechanisms to other mitochondrial quality control pathways. In fact, the LON protease and the ATP-dependent Clp protease (CLPP) are essential for protein homeostasis in the mitochondrial matrix, and deficits in their activity are tightly linked to a decline in mitochondrial function and to aging[258]. Interestingly, the LON protease is also known to regulate mitochondrial levels of PINK1[259], as well as being the dominant protease responsible for initially handling of misfolded and aggregated proteins in the mitochondrial matrix[260]. The latter stimulus is the classic activator of the UPR^{mt}. Indeed, the UPR^{mt} and mitophagy form a continuum of pathways where mitophagy takes over when UPR^{mt} activation is insufficient to re-establish mitochondrial homeostasis. Thus, while, for clarity, mitophagy and the UPR^{mt} have been discussed here as distinct regulatory pathways, the aforementioned observation with LON protease, as well as other evidence suggest the existence of substantial cross-regulation between these various mitochondrial quality control pathways, which we grouped together, using the term mitochondrial stress response (MSR).

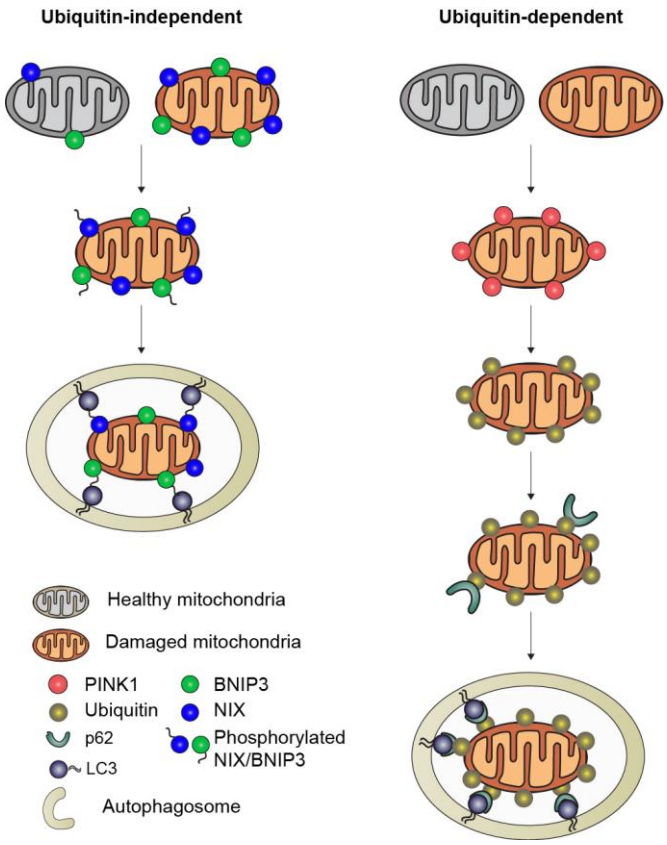

Fig. 1.6 | During the ubiquitin-independent mitophagy BNIP3 and NIX, normally present on the mitochondrial membrane, accumulate on the surface of the damaged mitochondria which is further promoted by their phosphorylation. Both BNIP3 and NIX serve as docking sites for LC3 and the autophagosome leading to destruction of dysfunctional mitochondria. During the ubiquitin-dependent mitophagy PINK1, which is degraded in the mitochondria under basal conditions, is stabilized on the surfaced of damaged and depolarized mitochondria. PINK1 decoration of the mitochondrial membrane ensures the ubiquitination of the mitochondrial surface which, in returns, recruits p62. This ubiquitin-binding protein is used to anchor damaged mitochondria to LC3 mediating their engulfment in the autophagosome and ultimately their degradation.

Mitochondrial quality control and neuromuscular degenerative diseases

Given the acquired mitochondrial defects observed in aging and age-associated diseases, it is not surprise that mitochondrial quality control plays an important role in these conditions by maintaining mitochondrial proteostasis. Strategies aiming at improving these stress pathways, indeed, mediate a number of anti-aging effect. Mitonuclear imbalance, a process capable of triggering the UPR^{mt}, correlates with increased lifespan in the BXD mouse population[261]; while genetic or pharmacological induction of the UPR^{mt} in nematodes mediates an increase of lifespan and fitness in old age[261]. Both ATFS-1 and UBL-5 are required for UPR^{mt} mediated positive effects in nematodes, underlining their crucial role in mediating this stress response[261]. Concordantly, activating mitophagy genetically or through administration of a variety of compounds mediates health- and lifespan extension in worms and mammals[261–265].

Mitochondrial quality control relies on mitochondrial membrane potential and transport for their signaling, two mitochondrial features that are altered under proteotoxic stress. Accordingly, both UPR^{mt} and mitophagy are altered in these disorders. Interestingly, AD and PD patients display increased UPR^{mt} gene expression in brain tissue, while induction of mitophagy is observed in both humans and mouse models of AD[266,267]. On the other hand, mutations of the mitophagy mediators PINK1 and Parkin and defects in the UPRmt mediator, LONP, characterize PD patients along with impaired mitochondrial dynamics necessary for correct mitochondrial quality control[268–270]. Perturbation of mitochondrial dynamics is also a predominant feature of other proteinopathies, such as HD [271,272]. Conversely, the induction of mitochondrial quality control is sufficient to promote neuroprotection in both HD and PD [273–275]. The importance of mitochondrial quality control is not restricted to the nervous system as IBM has been linked to mutations in valosin-containing protein and sequestosome 1, already implicated in mitochondrial proteostasis and mitophagy[276,277] while boosting mitochondrial quality control inhibits muscle impairments in a rat model of IBM[278].

Accordingly, recent evidence suggests an involvement of mitochondrial proteostasis in proteotoxic neuromuscular diseases progression and in cell survival to proteotoxic stress.

Emerging research is focused on understanding how mitochondrial quality control can impact on protein aggregation and therefore aging and a variety of age-associated neuromusclular degenerative disorders. In this frame, my thesis aims to characterize a causal link between cytosolic proteotoxic stress and mitochondrial homeostasis. In particular, we investigate how mitochondrial quality control can impact cytosolic proteostasis in amyloidosis disorders and skeletal muscle aging.

Chapter 2

Enhancing mitochondrial proteostasis reduces amyloid-β proteotoxicity

Vincenzo Sorrentino[1], Mario Romani[1*], Laurent Mouchiroud[1*], John S. Beck[2], Hongbo Zhang[1], Davide D'Amico[1], Norman Moullan[1], Francesca Potenza[1], Adrien W. Schmid[3], Solène Rietsch[1], Scott E. Counts[2], Johan Auwerx[1]

[1]Laboratory for Integrative and Systems Physiology, Institute of Bioengineering, Ecole Polytechnique Fédérale de Lausanne, CH-1015 Lausanne, Switzerland; [2]Department of Translational Science and Molecular Medicine, Department of Family Medicine, Michigan State University, Grand Rapids, MI 49503, USA; [3]Proteomics Core Facility, Ecole Polytechnique Fédérale de Lausanne, CH-1015 Lausanne, Switzerland

Correspondence to Johan Auwerx at admin.auwerx@epfl.ch

*, These authors contributed equally to this work

One-sentence summary Amyloid-β peptide proteopathies perturb mitochondria and repairing mitochondrial proteostasis reduces protein aggregation in animal models of amyloid-β disease.

Alzheimer's disease (AD) is a common and devastating disease characterized by the aggregation of amyloid-β peptide (Aβ), yet we know relatively little about the underlying molecular mechanisms or how to treat AD patients. Here, we provide bioinformatic and experimental evidence of a conserved mitochondrial stress response signature present in Aβ proteotoxic diseases in human, mouse and *C. elegans*, and which involves the UPR^{mt} and mitophagy pathways. Using the worm model of Aβ proteotoxicity, GMC101, we recapitulated mitochondrial features and confirmed the induction of this mitochondrial stress response as key to maintain mitochondrial proteostasis and health. Importantly, boosting mitochondrial proteostasis by pharmacologically and genetically targeting mitochondrial translation and mitophagy increases fitness and lifespan of GMC101 worms and reduces amyloid aggregation in cells, worms, and in AD transgenic mice. Our data support the relevance of enhancing mitochondrial proteostasis to delay Aβ proteotoxic diseases, such as AD.

Aging is often accompanied by the onset of proteotoxic degenerative diseases, characterized by the accumulation of unfolded and aggregated proteins. Amyloid diseases are proteotoxic disorders, which can affect the nervous system, like in the case of Alzheimer's (AD), the most common form of dementia[279], but also other organs, as exemplified by amyloidosis-associated kidney disease[280] and inclusion body myositis (IBM)[281]. To date, no efficient therapy is available for AD[282], a disease with a strong component of amyloid-β (Aβ) aggregation[279]. Clinical trials for AD focused primarily on counteracting Aβ aggregation in the brain, considered the key pathogenic mechanism[283]. However, AD is a complex multifactorial disease[284] and mitochondrial dysfunction emerged as a common pathological hallmark[285]. Mitochondrial abnormalities in AD include decreased mitochondrial respiration and activity and alterations in mitochondrial morphology[285]; however, the relevance of other aspects of mitochondrial homeostasis, such as mitochondrial proteostasis, to the pathogenesis of AD is still largely unknown.

Mitochondrial function pathways are perturbed in AD

We investigated brain expression datasets from AD patients (GN327, GN328 and GN314) archived in GeneNetwork (www.genenetwork.org) to define the mitochondrial signature associated with the disease. Gene Set Enrichment Analysis (GSEA) of datasets from healthy *versus* AD individuals in prefrontal, primary visual cortex and whole brain showed that downregulation of mitochondrial oxidative phosphorylation (Oxphos) and perturbation of mitochondrial import pathways were hallmarks of AD (**Fig. 2.1a, Extended Data Fig. 2.1a,b,c,e,f** and **Supplementary Table 1-4**). As these processes are linked with, and affect mitochondrial proteostasis[286], we used comprehensive gene sets for two major mitochondrial quality control pathways, the mitochondrial unfolded protein response (UPR^{mt}) and mitophagy, to evaluate whether their expression is co-regulated in AD patients (**Supplementary Table 5**). Whereas we observed a tight correlation between genes typifying UPR^{mt} and mitophagy in all brain datasets investigated (**Fig. 2.1b** and **Extended Data Fig. 2.1d,g**), other stress pathways, such as the ER stress (UPR^{er}) and heat shock response (HSR) were co-regulated to a lower degree (**Fig. 2.1b** and **Extended Data Fig. 2.1d,g**).

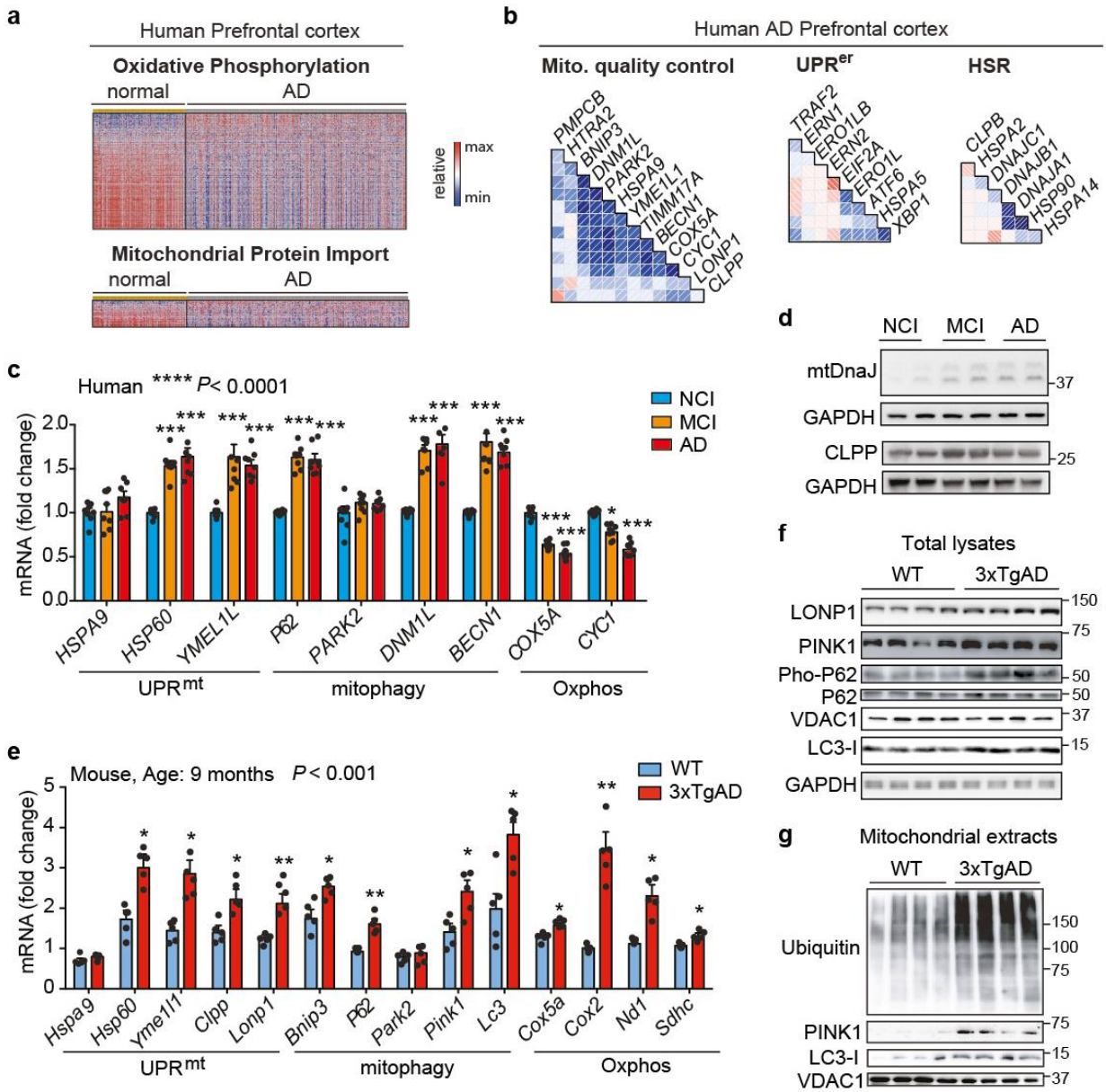

Fig. 2.1 | Mitochondrial dysfunction in AD is typified by a conserved Mitochondrial Stress Response. a Heatmap of the expression levels of Oxphos and mitochondrial import genes in human AD prefrontal cortex (GN328; normal, *n*=195; AD, *n*=388 individuals). **b,** Correlation plots of mitochondrial stress genes, UPR^{er} and HSR levels in prefrontal cortex from AD patients (GN328; *n* as in **a**). See **Extended Data Fig. 1** and **Supplementary Table 1-5**. **c-d**, Transcript analysis of the Mitochondrial Stress Response signature (**c**; MSR, *n*=8 per group) and Western blot (**d**, WB, *n*=2 individuals) of mtDNaJ and CLPP in brains of humans with no cognitive impairment (NCI), mild-cognitive impairment (MCI) and mild/moderate AD. **e-f,** Transcript (**e**) and immunoblot (**f**) analysis of MSR genes in cortex of 9-months old wild type (WT) and 3xTgAD mice (WT, *n*=5; 3xTgAD, *n*=5 for RNA; WT, *n*=4; 3xTgAD, *n*=4 for WB, representative of 6 animals). **g,** Immunoblot (WT, *n*=4; 3xTgAD, *n*=4, WB representative of 5 animals) of mitophagy and autophagy proteins in mitochondrial extracts from cortex tissues of the animals in **e-f**. Values in the figure are mean ± s.e.m. **P*<0.05; ***P*≤0.01; ****P*≤0.001. Throughout the figure, overall differences between conditions were assessed by two-way ANOVA. Differences for individual genes/proteins were assessed using two-tailed *t* tests (95% confidence interval). All experiments were performed independently twice. Mito., mitochondrial. See also **Extended Data Fig. 2**. For uncropped gel source data, see **Supplementary Fig. 1**. For all the individual *p* values, see the **Fig.1 Spreadsheet** file.

Evidence for a mitochondrial stress signature in AD

We then measured UPR^{mt}, mitophagy and Oxphos transcripts in human cortex. Previously, we reported that several UPR^{mt} genes were up-regulated during frank familial or sporadic AD[287]. Here, we extended that analysis and observed that, compared to subjects with no cognitive impairment (NCI), several UPR^{mt} and mitophagy transcripts were also up-regulated in patients with mild cognitive impairment (MCI), a putative prodromal AD stage[288],

and in mild/moderate AD (**Fig. 2.1c** and **Supplementary Table 6**), whereas Oxphos genes were down-regulated, consistent with our GSEA. The induction of this mitochondrial stress response was also observed at the protein level in MCI and AD subjects (**Fig. 2.1d**). The occurrence of this perturbation already in MCI suggests that mitochondrial dysfunction contributes to neuron and synapse loss, and that mitochondrial stress pathways may be activated as a protective response during disease progression[288]. We also analyzed cortex samples of wild-type (WT) and 3xTgAD mice[289] (**Extended Data Fig. 2.2a**) at 6 and 9 months of age. Both mitochondrial quality control and Oxphos genes were induced in AD mice (**Fig. 2.1e** and **Extended Data Fig. 2.2b**), although to a different extent over time. In fact, pairing WT and AD animals at these two times indicated a marked attenuation of this stress signature during disease progression (**Extended Data Fig. 2.2d-f**). Immunoblotting of total lysates from the cortex of WT and 3xTgAD mice showed the induction of PINK1, LONP1 and LC3 at both time points (**Fig. 2.1f** and **Extended Data Fig. 2.2c**). Additional analysis of the 9-month old animals also indicated a reduction in VDAC, a marked increase in P62 phosphorylation (**Fig. 2.1g**), and reduced citrate synthase (CS) activity (**Extended Data Fig. 2.2g**) in AD mice, indicative of autophagy and mitophagy. PINK1 and LC3-I were also increased in mitochondrial extracts from cortex samples of the AD mice (**Fig. 2.1g**), confirming that these proteins are recruited to the mitochondria to promote mitophagy, as supported by the augmented ubiquitylation of mitochondrial proteins (**Fig. 2.1g**). For simplicity, we abbreviate the comprehensive mitochondrial stress footprint analyzed herein as Mitochondrial Stress Response (MSR).

Identification of a cross-species MSR signature

The functional impact of changes in mitochondrial homeostasis during disease and aging in mammals can be rather faithfully translated in the nematode *Caenorhabditis elegans*[290]. Worm models of Aβ aggregation have been extensively used to study the basic consequences of proteotoxic stress on conserved biological pathways between worms and mammals[291,292]. We took advantage of the GMC101 worm model of Aβ proteotoxicity. GMC101 worms constantly express the human Aβ isoform 1–42 in muscle cells, but adults only develop age-progressive paralysis and amyloid deposition in the body wall muscle after a temperature shift from 20 to 25°C[293], while the control strain CL2122 does not express the Aβ peptide (**Extended Data Fig. 2.3a**).

Transcripts of the worm orthologs of the MSR were induced in adult GMC101 worms compared to CL2122 following the temperature shift (**Fig. 2.2a**), while only partially perturbed at 20°C (**Extended Data Fig. 2.3b**). Basal and maximal respiratory capacity were decreased in GMC101 (**Fig. 2.2b** and **Extended Data Fig. 2.3c**), in contrast with the increased Oxphos transcript levels (**Fig. 2.2a**), suggesting a compensatory induction to ensure respiration. Mitochondrial content was lower in GMC101, as shown by decreased Oxphos proteins, mt/nDNA ratio and CS activity (**Fig. 2.2c** and **Extended Data Fig. 2.3d-e**). Importantly, GMC101 fitness, measured as spontaneous movement[294], was robustly reduced relative to CL2122 in line with the muscle disorganization and alteration of the mitochondrial network in the body wall muscle (**Extended Data Fig. 2.3f,g**). These data highlight the cross-species conservation of the MSR, and make GMC101 an excellent proxy to characterize the mitochondrial dysfunction and phenotypic impact observed in Aβ diseases in mammals.

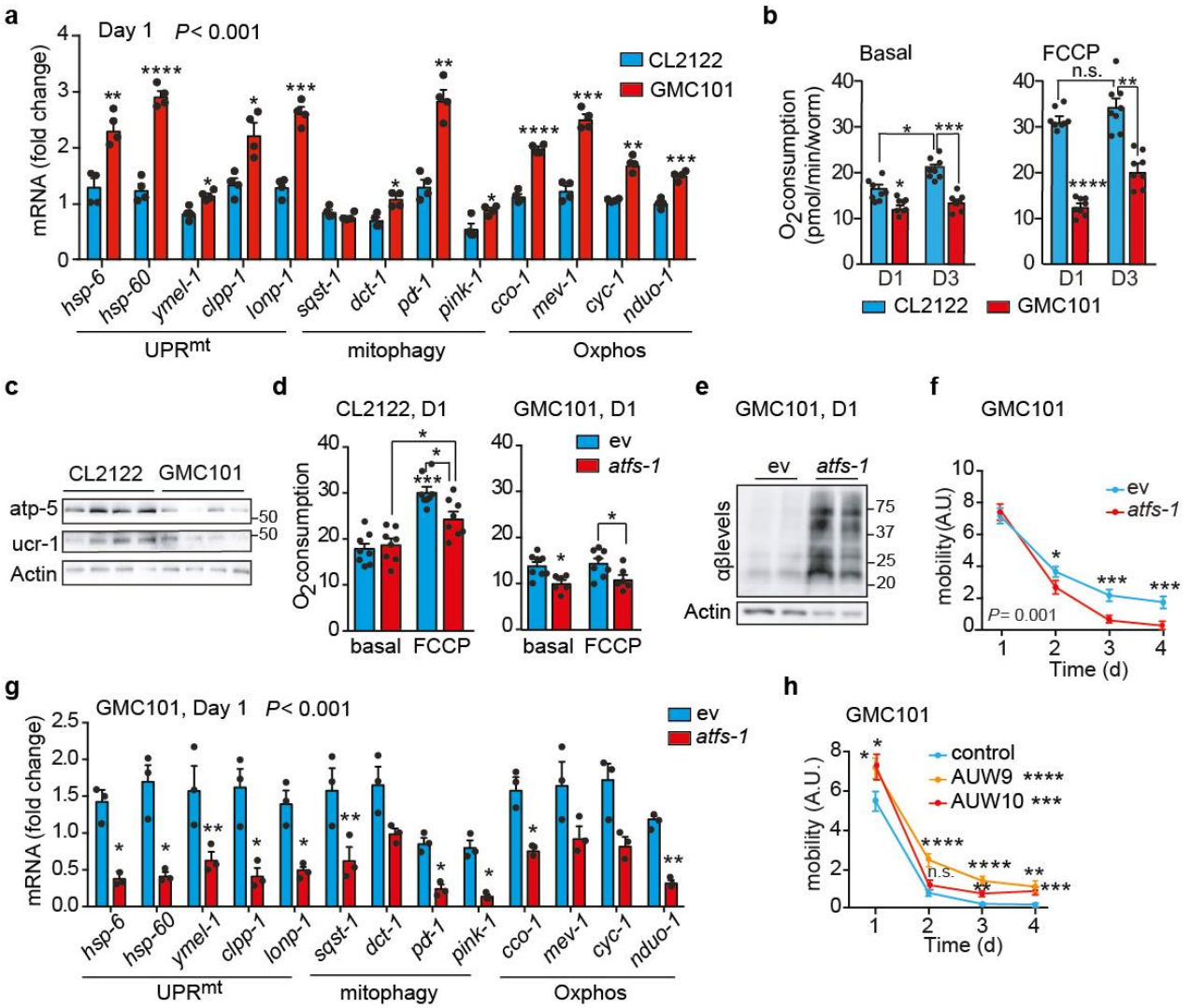

Fig. 2.2 | Mitochondrial dysfunction and reliance on *atfs-1* of GMC101 worms upon proteotoxic stress. a, MSR transcript analysis in CL2122 and GMC101 (*n*=3 biologically independent samples). **b,** Basal respiration and after FCCP (45 min, 10µM) of day 1 (D1) and 3 (D3) adult worms (CL2122, *n*=8; GMC101, *n*=8 biologically independent samples). **c,** Immunoblot (CL2122, *n*=4; GMC101, *n*=4, WB representative of 5 biological replicates) of Oxphos proteins in control and GMC101 at D1. **d,** Respiration assay as in **b** in CL2122 (ev, *n*=8; *atfs-1*, n=8 biologically independent samples) and GMC101 (ev, *n*=8; *atfs-1*, *n*=6 biologically independent samples) fed with *atfs-1* RNAi. **e,** Amyloid aggregation in GMC101 upon *atfs-1* RNAi shown by WB of 2 biological repeats. **f,** Mobility of GMC101 fed with 50% *atfs-1* RNAi (ev, *n*=59; *atfs-1*$^{1/2}$, *n*=50 worms). **g,** MSR transcript analysis of GMC101 upon *atfs-1* RNAi (*n*=3 biologically independent samples). **h,** Mobility of control and *atfs-1* overexpressing GMC101 strains (GMC101, *n*=61; AUW9, *n*=48; AUW10, *n*=41 worms). Values in the figure are mean ± s.e.m. **P*<0.05; ***P*≤0.01; ****P*≤0.001; *****P*≤0.0001; n.s., non-significant. Throughout the figure, overall differences between conditions were assessed by two-way ANOVA. Differences for individual genes/proteins were assessed using two-tailed *t* tests (95% confidence interval). All experiments were performed at least independently twice. Mito., mitochondrial; ev, scrambled RNAi; A.U., arbitrary units. See also **Extended Data Fig. 3-4**. For uncropped gel source data, see **Supplementary Fig. 1**. For all the individual *p* values, see the **Fig. 2 Spreadsheet** file.

Mitochondrial homeostasis counters Aβ proteotoxicity

The control of mitochondrial function and UPR^{mt} during stress in the worm is largely attributable to the activating transcription factor associated with stress, *atfs-1*[241,243]. Depletion of *atfs-1* by RNAi feeding of the GMC101 worms, but not CL2122, caused a severe developmental delay even in absence of the "disease-inducing" temperature shift (**Extended Data Fig. 2.3h**), phenocopying mitochondrial respiration mutants that rely on *atfs-1* for survival and adaption[243]. Comparative analysis of transcripts involved in cytosolic and nuclear adaptation pathways, such as UPR^{er}, HSR, and *daf-16,* showed also a mild induction of the UPR^{er} and a striking upregulation of the HSR in GMC101 (**Extended Data Fig. 2.3i**), in line with the role of HSR as a primary defense against proteotoxic stress in

worm[295]. We therefore evaluated the effect of RNAis targeting key regulators of these pathways, *hsf-1* and *xbp-1*, on the development of GMC101. Only *atfs-1* RNAi again led to extreme developmental delays, while no alterations were observed with all these RNAis in CL2122 (**Extended Data Fig. 2.3j)**.

Importantly, basal and maximal respiration in adult GMC101 was significantly impaired upon *atfs-1* silencing, while only maximal respiration was partially affected in CL2122 (**Fig. 2.2d**). In addition, *atfs-1* RNAi exacerbated aggregation (**Fig. 2.2e** and **Extended Data Fig. 2.3k**) and paralysis (**Fig. 2.2f**) in GMC101, while CL2122's mobility was unaffected (**Extended Data Fig. 2.3l**). Furthermore, *atfs-1* knockdown in GMC101 prominently repressed the MSR signature, including mitophagy effectors (**Fig. 2.2g**), whereas in CL2122, *pdr-1*, *dct-1* and Oxphos transcripts were even induced, in spite of *atfs-1* silencing in both strains (**Extended Data Fig. 2.3m,n**).

Given the induction of the HSR in the GMC101, we tested whether *hsf-1* repression would impact on fitness. Interestingly, while *atfs-1* knockdown only paralyzed GMC101, silencing of *hsf-1* reduced mobility in both CL2122 and wild-type N2 strains when incubated at 25˚C (**Extended Data Fig. 2.3o**), reflecting a general effect of *hsf-1* on homeostasis independent of the strain. Worm mobility was similarly impaired in GMC101, but not in CL2122, following silencing of *atfs-1* with an alternative RNAi we generated (*atfs-1 #2*) (**Extended Data Fig. 2.3p,q** and **Supplementary Table 13**), confirming a specific role of *atfs-1* in ensuring organismal homeostasis in GMC101. Furthermore, silencing of *ubl-5*, another positive regulator of the UPR^{mt} [296], also delayed development and decreased health- and lifespan specifically in GMC101 (**Extended Data Fig. 2.4a-c**). Intriguingly, *atfs-1* silencing led to further upregulation of the HSR in GMC101 and to its induction in CL2122 (**Extended Data Fig. 2.4d,e**), while repressing the MSR specifically in GMC101 (**Fig. 2.2g** and **Extended Data Fig 2.3n**).

Conversely, to enhance *atfs-1* function, we generated two GMC101-derived strains, AUW9 and AUW10, and one CL2122 line (AUW11), overexpressing *atfs-1* (**Supplementary Table 12,13**). This resulted in the induction of the UPR^{mt} (**Extended Data Fig. 2.4f**), a significant increase in fitness, and a discrete decrease in paralysis and death scores in the GMC101-derived strains AUW9 and AUW10 (**Fig. 2.2h** and **Extended Data Fig. 2.4g,h)**, while no changes were observed in AUW11 (**Extended Data Fig. 2.4g**). As an alternative approach to increase mitochondrial stress response, we crossed GMC101 with two long-lived mitochondrial mutants, *i.e. clk-1*[297] and *nuo-6*[298] (**Supplementary Table 12,13**). Consistently, GMC101 with a mutation in these mitochondrial genes (AUW12 and AUW13) manifested intermediate phenotypes between GMC101 and their mitochondrial mutant counterpart, with enhanced healthspan and lifespan (**Extended Data Fig. 2.4i-l**).

Altogether, this indicates that *atfs-1* and the MSR induction ensure proteostasis and survival in this worm model of Aβ aggregation, and that mitochondria play an active, rather than passive, role during Aβ proteotoxic stress. This prompted us to investigate the potential of boosting mitochondrial proteostasis to curb the progression of this deleterious phenotype.

Reducing mitochondrial translation lowers Aβ proteotoxicity

Given the tight link between the UPR^{mt} and AD observed above, we investigated the effects of two established strategies to induce the UPR^{mt} in *C. elegans*; genetically, by silencing the expression of the mitochondrial ribosomal protein *mrps-5*[261], and pharmacologically, by using the mitochondrial translation inhibitor doxycycline (dox)[261,299]. Both interventions, which favor worm health and lifespan[261], markedly induced transcripts of UPR^{mt}, mitophagy and respiration genes in GMC101 (**Fig. 2.3a,b**), without causing major development and

growth delays (**Extended Data Fig. 2.5a**). Dox similarly induced these pathways in CL2122 (**Extended Data Fig. 2.5b**). No perturbations of UPR^{er} and HSR in GMC101 treated with dox or *mrps-5* RNAi were observed (**Extended Data Fig. 2.5c,d)**, while one *daf-16* target, mitochondrial superoxide dismutase *sod-3,* was induced (**Extended Data Fig. 2.5c,d)**. The transcriptional induction of the MSR impacted beneficially on fitness and lifespan of GMC101 (**Fig. 2.3c-e**). Furthermore, Aβ aggregation was reduced by *mrps-5* RNAi and dox (**Fig. 2.3f** and **Extended Data Fig. 2.5e**). Of essence, the improvement in motility and Aβ clearance in GMC101 required *atfs-1* (**Fig. 2.3g,h**), proving the vital contribution of the UPR^{mt} to the phenotypic improvements. Respirometry on GMC101 worms fed with *mrps-5* RNAi at D3 and D6 of adulthood (**Extended Data Fig. 2.5f**), showed that *mrps-5* knockdown prevented the decrease in respiration upon aging, suggesting a stabilization of mitochondrial function following the MSR-dependent improvement of proteostasis.

We then extended our investigation to a mammalian SY5Y neuroblastoma cell line expressing the APP Swedish K670N/M671L mutation (APP_{Swe})[300]. Dox markedly reduced intracellular Aβ deposits, as shown with an Aβ1-42-specific antibody (**Fig. 2.3k** and **Extended Data Fig. 2.5g**). This improvement was linked to a mito-nuclear protein imbalance and the induction of components of the MSR (**Extended Data Fig. 2.5h,i)**. These results add to observations of *in vitro*[301] and *in vivo* studies in AD flies[302] and patients[303], which suggested that dox treatment may ameliorate AD and Aβ aggregation. Recently, the regulation of the mitochondrial stress responses in mammals, including dox-dependent mitochondrial stress, was shown to rely on the activation of the integrated stress response (ISR) and on the transcription factor ATF4[304–306]. Pretreating cells with ISRIB, a global ISR inhibitor[307], prevented amyloid clearance by dox and hampered the dox-mediated induction of canonical ATF4 target genes, such as *CHOP* and *CHAC1*[304] (**Fig. 2.3k** and **Extended Data Fig. 2.5g,j**). This suggests the involvement of the ISR in resolving Aβ proteotoxic stress in mammalian cells.

Given the induction of mitophagy in 3xTgAD mice, human AD patients and in GMC101 worms, and its further increase upon *mrps-5* RNAi and dox treatments, we also tested the contribution of mitophagy to the homeostasis of GMC101. To achieve this, we silenced by RNAi *dct-1*, an evolutionarily conserved regulator of mitophagy[262]. *dct-1* RNAi reduced GMC101's health- and life-span already in basal conditions (**Extended Data Fig. 2.5k-m**). Furthermore, it blunted the positive effects of *mrps-5* RNAi and dox on health- and lifespan (**Fig. 2.3i** and **Extended Data Fig. 2.5l,m**) and proteostasis (**Fig. 2.3j**). Conversely, *dct-1* knockdown in CL2122 affected their movement only during aging (**Extended Data Fig. 2.5n,o**), stressing the relevance of mitophagy in aging. Altogether, these data show that mitophagy, in addition to UPR^{mt}, is also induced and required for the survival of GMC101 worms and for the beneficial effects of the described interventions.

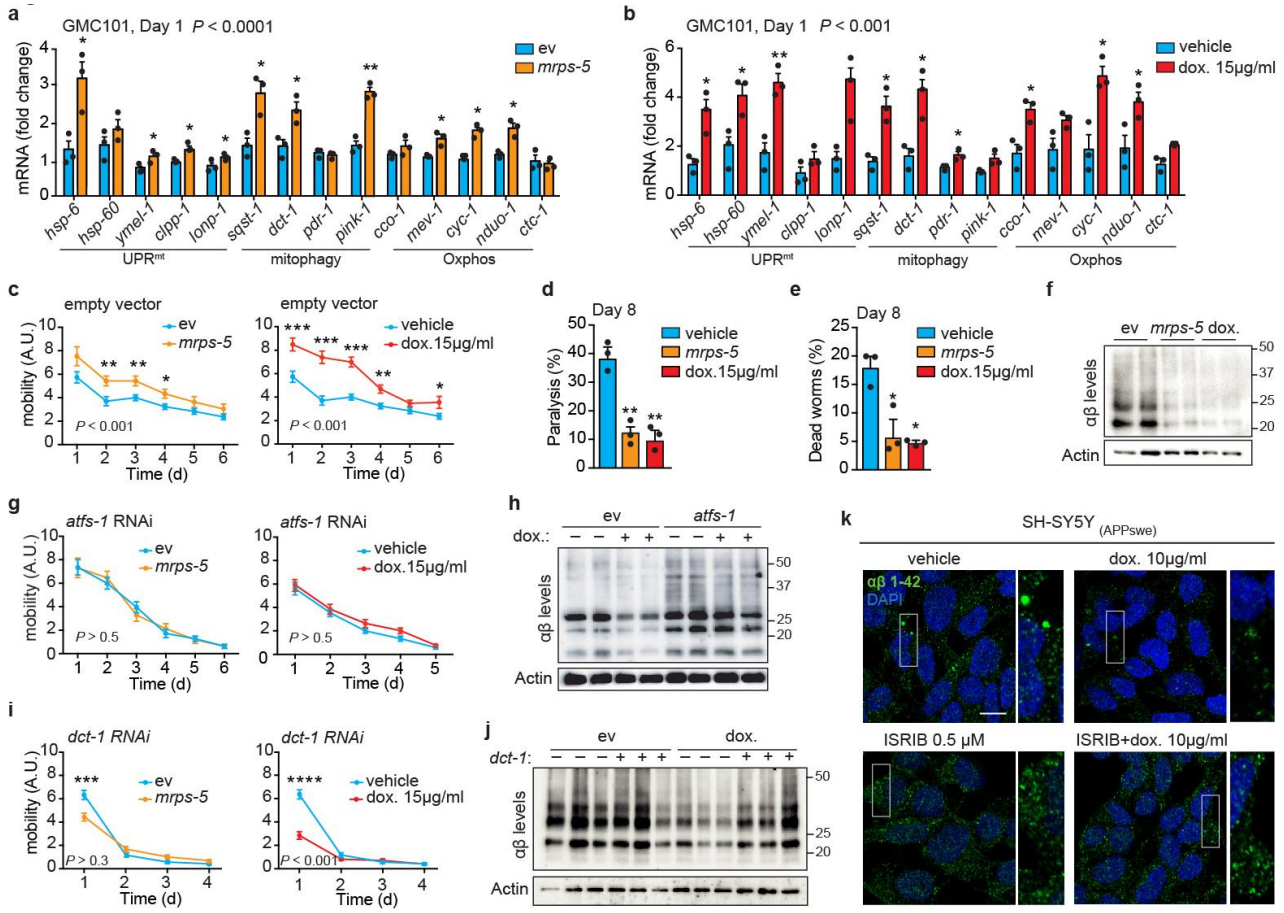

Fig. 2.3 | Inhibiting mitochondrial translation reduces Aβ proteotoxicity and aggregation in GMC101 worms and in cells. a-b, MSR transcript levels in GMC101 fed *mrps-5* RNAi or treated with dox (**a** and **b**, *n*=3 biologically independent samples). **c,** Mobility of GMC101 upon *mrps-5* RNAi (*n*=35 worms) or dox treatment (*n*=54 worms). **d-e,** Percentage of paralyzed (**d**) and dead (**e**) D8 adult GMC101 worms after *mrps-5* RNAi or dox treatment (*n*=3 independent experiments). **f,** Western-blot of amyloid aggregation in GMC101 upon *mrps-5* RNAi or dox treatment (*n*=2 biologically independent samples). **g**, Mobility of GMC101 upon *atfs-1* RNAi feeding (ev, *n*=54; *mrps-5*, n=49; dox, n=49 worms). **h,** Amyloid aggregation in dox-treated GMC101 upon *atfs-1* RNAi (*n*=2 biological replicates). **i**, Mobility of GMC101 upon *dct-1* RNAi (ev, n=44; dox, *n*=59; *mrps-5, n*=66 worms). ***$P \leq 0.001$ (P=0.0004); ****$P \leq 0.0001$. **j,** Amyloid aggregation in dox-treated GMC101 upon *dct-1* RNAi (*n*=3 biologically independent samples). **k**, Confocal images of the SH-SY5Y neuroblastoma cell line stained with the anti-β-Amyloid 1-42, after dox and, where indicated, ISRIB treatments for 24 h. Scale bar, 10μm. See **Methods** for further details. Values in the figure are mean ± s.e.m. *$P<0.05$; **$P \leq 0.01$; ***$P \leq 0.001$; ****$P \leq 0.0001$. Throughout the figure, overall differences between conditions were assessed by two-way ANOVA. Differences for individual genes or two groups were assessed using two-tailed *t* tests (95% confidence interval). All experiments were performed independently at least twice. ev, scrambled RNAi; dox., doxycycline; A.U., arbitrary units; ISRIB, integrated stress response inhibitor. See also **Extended Data Fig. 5**. For uncropped gel source data, see **Supplementary Fig. 1**. For all the individual *p* values, see the **Fig. 3 Spreadsheet** file.

NAD$^+$ boosters attenuate Aβ proteotoxicity

The UPR^{mt} and mitophagy pathways are also potently induced in worms and in various mammalian tissues by NAD$^+$-boosting compounds, such as nicotinamide riboside (NR), and Olaparib (AZD2281 or AZD)[41,155,172,308]. Similarly to dox and *mrps-5* RNAi, treatment of GMC101 with NR and AZD induced the MSR (**Fig. 2.4a,b**), and improved health- and lifespan (**Fig. 2.4c-d** and **Extended Data Fig. 2.6a**). The NR- and AZD-mediated induction of the MSR was also observed in CL2122 (**Extended Data Fig. 2.6b,c)**, but, these treatments only improved CL2122 fitness during aging (**Extended Data Fig. 2.6d,e**), similarly to what previously was shown in N2 worms[155]. In addition, treatment of GMC101 with NR and AZD reduced proteotoxic stress (**Fig. 2.4e**). Importantly, the NR-mediated phenotypic and proteostasis benefits required *atfs-1* (**Fig. 2.4f-h**, **Extended Data Fig. 2.6f**) and *dct-1* (**Fig. 2.4i-k**, **Extended Data Fig. 2.6g**). NR has been shown to increase sirtuin activity, and activate the FOXO/*daf-16* signaling in mammals and *C. elegans*[155]. Therefore,

we evaluated the effect of *daf-16* and *sir-2.1* silencing on development, healthspan and NR-dependent benefits of GMC101. While *sir-2.1* knockdown did not delay growth of GMC101 or its control (**Extended Data Fig. 2.6h**), it increased paralysis and death in the GMC101 similarly to *dct-1* and *atfs-1* RNAis (**Extended Data Fig. 2.6i,k**). However, NR still significantly rescued health- and life-span of GMC101 fed with *sir-2.1*, showing that the effects of NR rely mostly on *atfs-1* and *dct-1* (**Extended Data Fig. 2.6i,k**). Instead, feeding GMC101 with *daf-16* RNAi did not result in major phenotypic changes (**Extended Data Fig. 2.6h,j,k**). Furthermore, NR did not affect the expression of *daf-16* and its targets (**Extended Data Fig. 2.6l**). NR and AZD had only a minimal impact on UPR^{er} and HSR in GMC101, with the induction of *hsp-16.41* and *hsp-16.48/49* (**Extended Data Fig. 2.6l,m**). These results indicate that in the GMC101 model, the main mode of action of NAD$^+$ boosting involves the induction of the MSR.

We also assessed the effect of NR in the Aβ-expressing neuronal cells and consistent with the data in *C. elegans*, we observed a remarkable reduction of the intracellular Aβ deposits with NR (**Fig. 2.4l** and **Extended Data Fig. 2.6n**), accompanied by increased Oxphos protein (**Extended Data Fig. 2.5h**) and MSR transcript levels (**Extended Data Fig. 2.6o**).

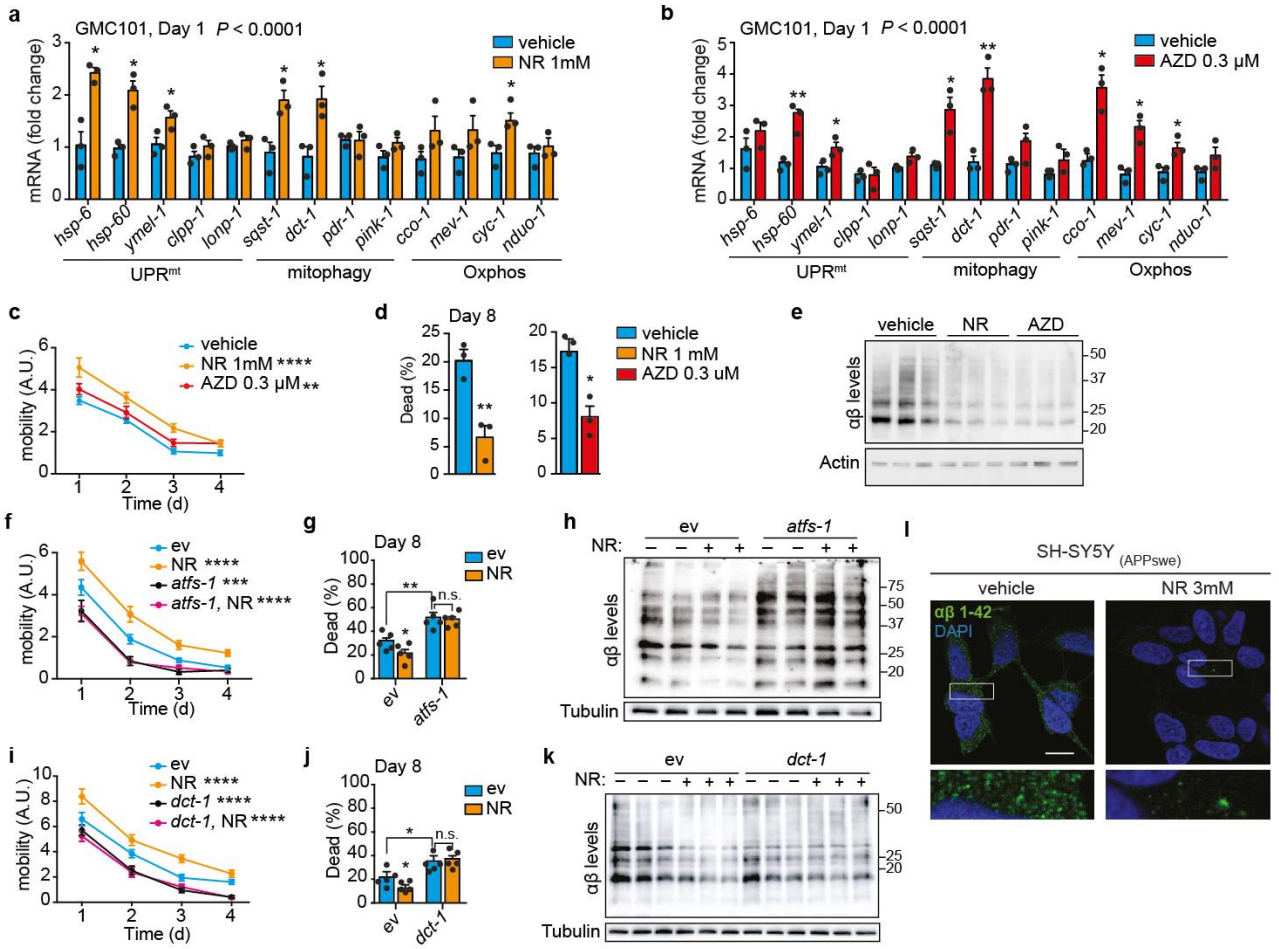

Fig. 2.4 | NAD$^+$ boosters reduce Aβ proteotoxicity and aggregation in GMC101 worms and cells. a-b, MSR transcripts in GMC101 worms treated with nicotinamide riboside (**a**, NR) or Olaparib (**b**, AZD). **a-b**, *n*=3 biologically independent samples. **c,** Mobility of GMC101 treated with NR (*n*=50 worms) or AZD (*n*=39 worms). ***P*≤0.001 (AZD,0.006); *****P*≤0.0001 (NR). **d,** Percentage of dead D8 adult GMC101 after NR or AZD (*n*=3 independent experiments). **e,** Western-blot of amyloid aggregation in GMC101 after NR or AZD (*n*=3 biologically independent samples for all groups). **f**, Mobility of GMC101 treated with NR upon *atfs-1* RNAi feeding (ev, *n*=52; *atfs-1*, *n*=38; NR, *n*=40; NR, *atfs-1*, *n*=41 worms). ****P*≤0.001 (*atfs-1*,0.0006). **g,** Percentage of dead D8 adult GMC101 treated with NR upon *atfs-1* RNAi (*n*=5 biologically independent samples). **h,** Amyloid aggregation in NR-treated GMC101 upon *atfs-1* RNAi feeding (WB representative of 2 biological replicates). **i**, Mobility of NR-treated GMC101 upon *dct-1* RNAi (ev, *n*=41; *dct-1*, *n*=40; NR, *n*=39; NR, *dct-1*, *n*=50 worms). **j,** Percentage of dead D8 adult GMC101 treated with NR upon *dct-1* RNAi (*n*=5 biologically independent samples). **k,** Amyloid aggregation immunoblot in NR-treated GMC101 upon *dct-1* RNAi (*n*=3 biologically independent samples). **l**, Confocal images of APP$_{Swe}$ SH-SY5Y

cells stained with anti-β-Amyloid 1-42, after 24 h NR treatment. Scale bar, 10μm. Values in the figure are mean ± s.e.m. *P<0.05; **P≤0.01; ***P ≤ 0.001; ****P≤0.0001; n.s., non-significant. Throughout the figure, overall differences between conditions were assessed by two-way ANOVA. Differences for individual genes or two groups were assessed using two-tailed t tests (95% confidence interval). All experiments were performed independently at least twice. ev, scrambled RNAi; A.U., arbitrary units. See also **Extended Data Fig. 6**. For uncropped gel source data, see **Supplementary Fig. 1**. For all the individual p values, see the **Fig. 4 Spreadsheet** file.

NR reduces Aβ levels in AD transgenic mice

We have previously shown that NR exerts beneficial effects on health- and lifespan[41,155], but whether it also improves mitochondrial function and proteostasis *in vivo* in a mouse model of Aβ proteotoxicity is so far unknown. We hence treated *APP/PSEN1* AD mice with NR and assessed the levels of Aβ plaques in brain with Thioflavin S, as well as mitochondrial Oxphos and MSR transcript and protein expression. In agreement with the effects observed in cells and worms, NR robustly reduced Aβ deposits in cortex tissues of the AD mice (**Fig. 2.5a**), and induced the MSR mRNA signature (**Fig. 2.5b**) and Oxphos protein levels (**Fig. 2.5c**). NR also enhanced context-dependent memory in the *APP/PSEN1* AD mice, which was impaired compared to WT animals, as assessed by contextual fear conditioning[309] (**Fig. 2.5d**), suggesting a potential positive impact on cognitive function. We hence propose that restoring or boosting mitochondrial function and proteostasis induces a conserved repair mechanism, from worm to mouse that leads to decreased Aβ proteotoxicity and improves health- and lifespan.

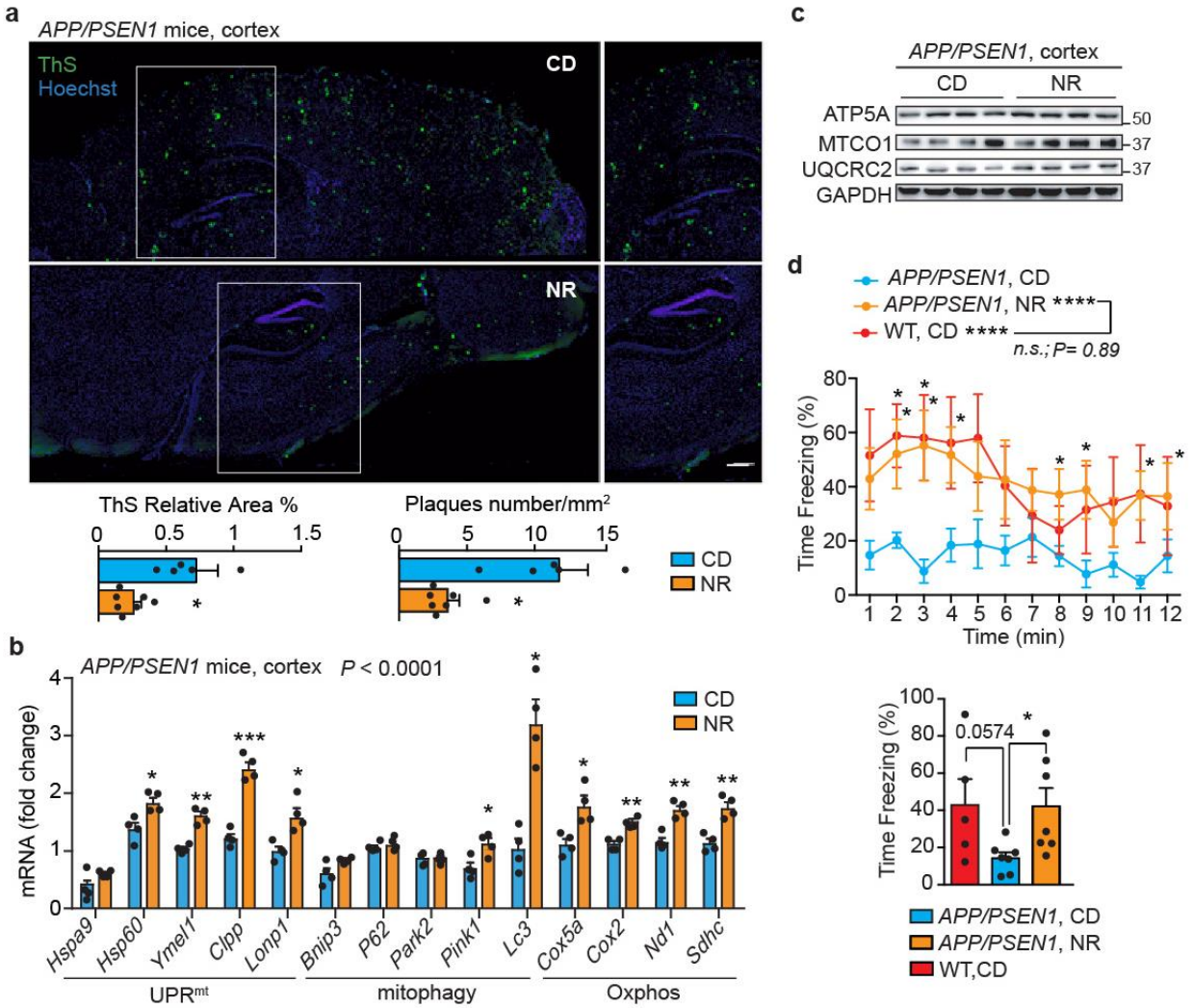

Fig. 2.5 | NR reduces Aβ deposits, induces the MSR and improves contextual memory in transgenic AD mice. a, Representative images and corresponding quantification of plaques in cortex samples of *APP/PSEN1* AD mice following NR treatment, stained using Thioflavin S (ThS) (CD, *n*=5 animals; NR, n=7 animals; NR 400mg/kg/day for 10 weeks). Scale bar, 200μm. **P*<0.05 (relative % area,0.041; number,0.014). **b-c,** MSR transcript (**b**) and immunoblot (**c**) analyses of cortex samples of *APP/PSEN1* mice following NR treatment (**b**, *n*=5 animals per group; **c**, *n*=4 animals per group). Data in **b**,**c** are representative of two independent experiments. **d**, Contextual fear conditioning in WT (*n*=5 animals) and *APP/PSEN1* mice with or without NR treatment (*n*=7 animals), plotted in function of the time intervals (left) or as average of the total obtained values (right). **P*<0.05 (*P*=0.03); *****P*≤0.0001. One-tail *t* test performed between WT and *APP/PSEN1* averaged values (*P*=0.0574, 95% confidence interval). Values in the figure are mean ± s.e.m. **P*<0.05; ***P*≤0.01; ****P*≤0.001; *****P*≤0.0001; n.s., non-significant. Throughout the figure, overall differences between conditions were assessed by two-way ANOVA. Differences for individual genes or two groups were assessed using two-tailed *t* tests (95% confidence interval). See **Methods** for further details. CD,chow diet. For uncropped gel source data, see **Supplementary Fig. 1**. For all the individual *p* values, see the **Fig. 5 Spreadsheet** file.

Discussion

Proteotoxic stress in Aβ diseases, such as AD, is associated with mitochondrial dysfunction, and reduced Oxphos activity has been considered one of the major hallmarks of these diseases. Here, we identify a cross-species mitochondrial stress response signature that implicates mitochondrial proteostasis as a key mechanism in the response to Aβ proteotoxic stress. Most importantly, we show that Aβ accumulation induces both the UPR^{mt} and mitophagy in a strikingly conserved manner from *C. elegans* to humans. Currently, the molecular mechanism driving this induction is still unclear. Based on our results, we speculate that it must involve the alteration of a basic, conserved functional process, such as for instance mitochondrial import, which is linked to the activation of the UPR^{mt} [243], is perturbed during Aβ proteotoxic stress[310] and is downregulated in AD patients in our analyses. Our work also provides solid evidence that mitochondria play an active role in the pathogenesis of Aβ diseases, as reducing mitochondrial homeostasis via *atfs-1* depletion in GMC101 worms aggravates the hallmarks of the disease (model in **Extended Data Fig. 2.7**); conversely, boosting mitochondrial proteostasis by increasing the UPR^{mt} and mitophagy decreases protein aggregation, restores worm fitness and delays disease progression, ultimately translating in increased lifespan. Similarly, in mammals we show that dox and NR decrease Aβ accumulation in a neuronal cell model and that NR treatment reduces amyloid plaque formation in brain and improves contextual memory in *APP/PSEN1* AD mice. These findings indicate that boosting mitochondrial function and proteostasis may decrease the formation of detrimental protein aggregates in the context of proteotoxic disease, typified by reduced mitochondrial activity and loss of proteostasis. Together with initial evidence suggesting potential benefits of targeting dysfunctional mitochondria in AD[162,213,301–303] and in view of recent findings linking mitochondrial stress to the induction of cytosolic proteostasis mechanisms[311–314], our data support the concept that enhancing mitochondrial proteostasis may hold promise to manage pervasive Aβ proteopathies, such as AD.

Methods

Animal experiments

3xTg AD mice, bearing human mutant APPswe, PS1M146V, and TauP301L transgenes[11], and wild-type, hybrid 129/C57BL6 mouse littermates were transcardially perfused with saline at 6 and 9 months of age (n = 6/group) and brains from each group were hemisected. One hemisphere was immersion-fixed in 4% paraformaldehyde/0.1% glutaraldehyde for 24 hours and stored in cryoprotectant. From the other hemisphere, hippocampus, frontoparietal cortex, and cerebellum were rapidly dissected and snap-frozen.

APP/PSEN1 mice (Tg(APPswe,PSEN1dE9)85Dbo/Mmjax) were purchased from JAX. *APP/PSEN1* mice were fed NR pellets (400 mg/kg/day) for 10 weeks, starting at the age of

4 months. The pellets were prepared by mixing powdered chow diet (2016S, Harlan Laboratories) with water or with NR dissolved in water. Pellets were dried under a laminar flow hood for 48 hours. Mice were housed by groups of 2 to 4 animals per cage and randomized to 7-8 animals per experimental group according to their body weight. No blinding was used during the experiment procedures.

Fear Conditioning

Fear conditioning was conducted as described previously[38], using chambers placed in sound-attenuating boxes (635x420x445mm) (Med Associates, USA). Each chamber is equipped with light (infra-red and visible), speakers, and the floor of the chamber consists of a stainless-steel grid connected to a shock generator. A computer running MED PC-IV (Med Associates, USA) controls the presentation of the stimuli (tone and shock). A video camera connected to the MED-VFC-NIR-M automated video-tracking system is used to detect and record movements and freezing behaviour. On the first day (conditioning session), mice were habituated to the testing chamber for 2min followed by the presentation of an auditory cue for 30sec [5kHz tone; 80dB, conditioned stimulus (CS)], co-terminating with a foot shock during the last 2 seconds [0.7mA; unconditioned stimulus (US)]. Mice received four CS-US pairings with an inter-trial interval of 2min. The last CS-US pairing was followed by a 2min-resting phase before mice were returned to their home cage. The entire conditioning session lasted 12min. On the second day, the mouse is re-exposed to the same context with no tone and the freezing response is monitored. Fear was assessed by measuring the percentage of time spent freezing, characterized by a crouching posture and an absence of any visible movement except breathing.

Ethical approval

All experiments were performed in compliance with all relevant ethical regulations. The experiments with postmortem human samples were authorized by the Michigan State University (MSU) Human Research Protection Program. Informed consent for brain autopsies of Rush Religious Orders Study participants was authorized by the Rush University Medical Center Institutional Review Board. The experiments with the 3xTg mice were authorized by the MSU Institutional Review Board and Institutional Animal Care and Use Committee. The experiments with *APP/PSEN1* mice were authorized by the local animal experimentation committee of the Canton de Vaud under license 3207. The committee that approved the license is the Commission cantonale pour l'expérimentation animale.

Human brain samples

Superior temporal cortex (Brodmann area 22) samples were obtained postmortem from participants in the Religious Orders Study who died with an antemortem clinical diagnosis of no cognitive impairment (NCI), mild cognitive impairment (MCI), or AD (n = 8/group) (**Supplementary Table 6**). Neuropsychological and clinical examinations, as well as postmortem diagnostic evaluations, have been described elsewhere[46]. Demographic, antemortem cognitive testing, and postmortem diagnostic variables were compared among the groups using the nonparametric Kruskal-Wallis Test with Bonferroni correction for multiple comparisons. Gender and apoE ε4 allele distribution were compared using Fisher's Exact Test with Bonferroni correction.

Bioinformatics analysis

For the *in silico* analysis of human brain expression datasets, we have used two sets of publicly available RNA-seq data: (1) from the Harvard Brain Tissue Resource Center (HBTRC), for human primary visual cortex (GN Accession: GN327) and human prefrontal cortex (GN Accession: GN328), and (2) from the Translational Genomics Research Institute, for the whole brain (GN Accession: GN314)[47]. These two datasets are publicly available on GeneNetwork (www.genenetwork.org). For correlation analysis, Pearson's r genetic correlation of the UPR^{mt}, mitophagy, ER stress and HSR gene sets was performed to establish the correlation between these pathways and genes that are associated or are causal to the development of AD. Analyses were performed using the hallmarks and canonical pathways gene sets databases. Additional information about the data sets employed are provided in **Supplementary information**.

Gene expression analyses

***C. elegans*:** A total of ≈3000 worms per condition, divided in 3 biological replicates, was recovered in M9 buffer from NGM plates and lysed in the TriPure RNA reagent. Each experiment was repeated twice. Total RNA was transcribed to cDNA using QuantiTect Reverse Transcription Kit (Qiagen). Expression of selected genes was analyzed using the LightCycler480 system (Roche) and LightCycler® 480 SYBR Green I Master reagent (Roche). For *C. elegans*, 2 housekeeping genes were used to normalize the expression data, namely actin (*act-1*) and peroxisomal membrane protein 3 (*pmp-3*). See **Supplementary Table 7** for the primer list.

Mouse: Total RNA was extracted from tissues using TriPure RNA isolation reagent (Roche) according to the product manual. Expression of selected genes was analyzed using the LightCycler480 system (Roche) and LightCycler® 480 SYBR Green I Master reagent (Roche). The beta-2-Microglobulin *B2m* gene was used as housekeeping reference. See **Supplementary Table 8** for the primer list.

Human: Total RNA was extracted using guanidine-isothiocyanate lysis (PureLink, Ambion, Waltham, MA) from cortex samples, and RNA integrity and concentration was verified using Bioanalysis (Agilent, Santa Clara, CA). Samples were randomized based on diagnostic group and assayed in triplicate on a real-time PCR cycler (ABI 7500, Applied Biosystems, Foster City) in 96-well optical plates. qPCR was performed using Taqman hydrolysis probe primer sets (Applied Biosystems) specific for the following human transcripts (**Supplementary Table 10**): *HSPA9*, *HSPD1*, *YME1L1*, *DNM1L*, *BECN1*, *SQSTM1*, *PARK2*, *COX5A*, *CYC1*. A primer set specific for human *GAPDH* was used as a control housekeeping transcript. For the APP_{Swe}-expressing SH-SY5Y cell line, total RNA was extracted from tissues using TriPure RNA isolation reagent, and expression of selected transcripts was analyzed using the LightCycler480 system (Roche) and LightCycler® 480 SYBR Green I Master reagent (Roche). The *GAPDH* gene was used as housekeeping reference. See **Supplementary Table 9** for the primer list. The ddCT method was employed to determine relative levels of each amplicon. Variance component analyses revealed relatively low levels of within-case variability, and the average value of the triplicate qPCR products from each case was used in subsequent analyses.

C. elegans strains and plasmids generation, and RNAi experiments

C. elegans strains (**Supplementary Table 12**) were cultured at 20°C on nematode growth media (NGM) agar plates seeded with *E. coli* strain OP50 unless stated otherwise. Strains used in this study were the wild-type Bristol N2, GMC101 [unc-54p::A-beta-1-42::unc-54 3'-UTR + mtl-2p::GFP][15], CL2122 [(pPD30.38) unc-54(vector) + (pCL26) mtl-2::GFP][48], CB4876 (*clk-1(e2519)*) and MQ1333 (*nuo-6(qm200)*). Strains were provided by the Caenorhabditis Genetics Center (University of Minnesota). The strain CL2122 was outcrossed 3 times in the N2 background, and subsequently used in the control experisments reported herein. AUW9 and AUW10: [GMC101+epfEx6[*atfs-1p::atfs-1]],* and AUW11: *[CL2122+epfEx7[atfs-1p::atfs-1]]* overexpression strains, and AUW12: [*GMC101+clk-1(e2519*) III], AUW13: [*GMC101+nuo-6(qm200)* I] were generated within this study.

Cloning and sequencing primers used in *C. elegans* are listed **Supplementary Table 13***. atfs-1p::atfs-1* expression vector was created by amplifying 1488 bp sequence upstream from the transcription start site of *atfs-1* coding region by using worm genomic DNA for the promoter region. The PCR product was digested with PciI and AgeI and ligated into the *pPD30.38* expression vector containing *gfp* coding sequence cloned between inserted AgeI and NotI restriction sites. The *atfs-1* coding sequence (CDS) was instead amplified using using *C. elegans* cDNA, and the PCR product was inserted into *pPD30.38* downstream of the promoter region, between AgeI and NheI restriction sites. The correctness of the *atfs-1p::atfs-1* construct was assessed by sequencing with the indicated *pPD30.38* and *atfs-1 seq*. primers. Two independent GMC101 lines (AUW9 and AUW10), and one CL2122 strain (AUW11) carrying *atfs-1p::atfs-1* transgene as extrachromosomal array were analyzed in the study. Injection marker *myo-2p::gfp* was cloned by amplifying 1179 bp sequence upstream from the transcription start site of *myo-2* coding region by using *C. elegans* genomic DNA. The PCR product was digested with PciI and AgeI and ligated into the *pPD30.38* expression vector containing *atfs-1::gfp* to replace *atfs-1* promoter sequence between PciI and AgeI restriction sites. All transgenic strains were created by using microinjection. For the generation of the GMC101 lines AUW12 and AUW13, GMC101 males were generated after exposure of L4 worms to 30°C for 3h, and let mate with L4 from *clk-1* or *nuo-6* mutant strains. The derived progeny was selected for homozygosis of the GMC101 intestinal GFP marker for few generations, and the homozygosis of the *clk-1* or *nuo-6* mutant alleles verified by amplifying and sequencing a 500 bp region of the worms genomic DNA encompassing the desired mutation (**Supplementary Table 13**). Bacterial feeding RNAi experiments were carried out as described[49]. Clones used were *atfs-1* (ZC376.7), *ubl-5* (F46F11.4), *mrps-5* (E02A10.1), *dct-1* (C14F5.1), *daf-16* (R13H8.1), *sir-2.1* (R11A8.4), *xbp-1* (R74.3) and *hsf-1* (Y53C10A.12). Clones were purchased from GeneService and verified by sequencing. The novel *atfs-1* RNAi construct (*atfs-1* #2) used in this study was generated by amplifying 1400 bp of the *atfs-1* genomic DNA sequence, starting from the last exon of *atfs-1*. Gateway cloning (Thermo Scientfic) was used to insert the PCR product into the gateway vector pL4440gtwy (Addgene #11344), and verified by sequencing. *atfs-1* knockdown was verified by qPCR for all the *atfs-1* RNAi constructs used herein. For phenotypic studies (see below), worms at the L4 larval stage were allowed to reach adulthood and lay eggs on the treatment plates. The deriving F1 worms were shifted from 20°C to 25°C at the L4 stage to induce amyloid accumulation and paralysis, and phenotypes assessed over time as indicated. For double RNAi experiments, we used a combination of *atfs-1* with *mrps-5* RNAi constructs as indicated in the text, with 80% amount of *atfs-1* and 20% *mrps-5* RNAi. For mRNA analysis, synchronized L1 worms were exposed to the treatment plates, and shifted from 20°C to 25°C when reaching the L4 stage. After 24 hours incubation at 25°C, corresponding to day 1 of adulthood, they were harvested in M9 for analysis.

Pharmacological treatment of C. elegans

Doxycycline was obtained from Sigma-Aldrich and dissolved in water[23]. For experiments, a final concentration of 15 µg/mL was used. Olaparib (AZD2281) was dissolved in DMSO to experimental concentrations of 300 nM[34]. Nicotinamide Riboside triflate (NR) was custom synthesized by Novalix (http://www.novalix-pharma.com/) and dissolved in water, and used at a final concentration of 1mM[34]. Compounds were added just before pouring the plates. For phenotyping experiments, parental F0 L4 worms were allowed to reach adulthood and lay eggs on the treatment plates. The deriving F1 worms were therefore exposed to compounds during the full life from eggs until death. For RNA analysis experiments, synchronized L1 worms were exposed to the compounds until harvest. To ensure a permanent exposure to the compound, plates were changed twice a week.

Worm phenotypic assays

Mobility: *C. elegans* movement analysis was performed as described[16], starting from day 1 of adulthood, using the Movement Tracker software. The experiments were repeated at least twice.

Development: 50 adult worms per condition were transferred on NGM agar plates (10 worms per plate) and allowed to lay eggs for 3 h. Then they were removed and the number of eggs per plate was counted. 72 h later, the number of L1–L3 larvae, L4 and adult worms was counted. The experiment was done twice with five individual plates.

Paralysis and death score: 5 L4 worms per condition were allowed to reach adulthood and lay eggs on the treatment plates. 45 to 60 deriving F1 worms per condition were manually scored for paralysis after poking, as already described[15]. Worms that were unable to respond to any, repeated stimulation, were scored as dead. Results are representative of the data obtained in at least three independent experiments.

Oxygen-consumption assays: Oxygen consumption was measured using the Seahorse XF96 equipment (Seahorse Bioscience)[34,50]. Respiration rates were normalized to the number of worms in each individual well and calculated as averaged values of 5 to 6 repeated measurements. Each experiment was repeated at least twice.

MitoTracker® Orange CMTMRos staining: A population of 20 worms at L4 stage were transferred on plates containing MitoTracker® Orange CMTMRos (Thermo Scientific) at a final concentration of 2ug/uL. The plates were incubated at 25°C and the worms were collected and washed in 200uL of M9 in order to remove the residual bacteria after 24h of treatment. The worms were then incubated for 30 minutes on regular NGM plates at 25°C and mounted on an agar pad in M9 buffer for visualization. Mitochondria were observed by using confocal laser microscopy.

Phalloidin and DAPI staining: A population of 100 L4 worms was incubated for 24h at 25°C. The worms were then washed in M9 and frozen in liquid nitrogen, immediately after they were lyophilized using a centrifugal evaporator. Worms were permeabilized using acetone. 2 U of phalloidin (Thermo Scientific) were resuspended in 20uL of a buffer containing: Na-phosphate pH 7.5 (final concentration 0.2mM), MgCl (final concentration 1mM), SDS (final concentration 0,004%) and dH_2O to volume. The worms were incubated for 1h in the dark and then washed 2 times in PBS and incubated in 20uL of 2ug/mL DAPI in PBS for 5 minutes. Following the immobilization, worms were observed by using confocal laser microscopy.

Quantitative real-time PCR for mtDNA/nuDNA ratio

Absolute quantification of the mtDNA copy number in worms was performed by real-time PCR. Relative values for *nd-1* and *act-3* were compared within each sample to generate a ratio representing the relative level of mtDNA per nuclear genome. The results obtained were confirmed with a second mitochondrial gene *MTCE.26*. The average of at least three technical repeats was used for each biological data point. Each experiment was performed at least on five independent biological samples.

Cell culture and treatments

The SH-SY5Y neuroblastoma cell line expressing the APP Swedish K670N/M671L double mutation (APP_{Swe})[25] was a kind gift of Prof. Cedazo-Minguez (Karolinska Institute, Sweden). Cells were grown in DMEM/F-12, supplemented with 10% fetal bovine serum (FBS, Gibco), GlutaMAX (100X, Gibco) and penicillin/streptomycin (1x, Gibco). Cells were selected in 4 µg/mL Geneticin® Selective Antibiotic (G418 Sulfate, Sigma) and grown for three generations before experiments with cells plated and passaged at 4x10^3 cells/ml and 60% confluence, respectively. Cells were cultured at 37 °C under a 5% CO_2 atmosphere and tested for mycoplasma using Mycoprobe (#CUL001B, R&D systems) following the manufacturer's instructions. Cells were treated with 10µg/mL dox, NR 1 or 3mM, ISRIB 0.5µM (Sigma), as indicated for 24 hours before cell harvesting or fixation. For the immunostaining, cells were fixed with 1x Formal-Fixx (Thermo Scientific) for 15min. After 15min permeabilization with 0.1% Triton X-100, cells were blocked in PBS supplemented with 5% fetal bovine serum for 1 hour and immunostained overnight, at 4ºC, with the anti-β-Amyloid 1-42 (1:100, Millipore AB5078P). The secondary antibody was coupled to the Alexa-488 fluorochrome (Thermo Scientific), and nuclei were stained with DAPI (Invitrogen, D1306). After washing in PBS, cell slides were mounted with Dako mounting medium (Dako, S3023) and examined with a Zeiss LSM 700 confocal microscope (Carl Zeiss MicroImaging) equipped with a Plan-Apochromat 40×/1.3 NA oil immersion objective lens using a 488 nm laser. Laser power was set at the lowest intensity allowing clear visualization of the signal. Imaging settings were maintained with the same parameters for comparison between different experimental conditions.

Western blot analysis

***C. elegans*:** Worms were lysed by sonication with RIPA buffer containing protease and phosphatase inhibitors (Roche), and analyzed by SDS–PAGE and western blot. The concentration of extracted protein was determined by using the Bio-Rad Protein Assay. Proteins were detected using the following antibodies: anti-β-actin (Sigma), anti-tubulin (Santa Cruz), atp-5, ucr-1 (Oxphos cocktail, Abcam), anti-β-Amyloid, 1-16 (6E10) (BioLegend). In addition to the housekeeping proteins, loading was monitored by Ponceau Red to ensure a homogeneous loading. Pixel intensity was quantified by using ImageJ software. Each immunoblot experiment was repeated at least twice using 3 biological replicates each containing ≈1000 worms.

Mouse: Frozen cortex tissue samples were lysed by mechanical homogenization with RIPA buffer containing protease and phosphatase inhibitors, and analyzed by SDS–PAGE and western blot. Subsequently, the concentration of extracted protein was determined by using the Bio-Rad Protein Assay. Proteins were detected using the following antibodies: HSP60 (Enzo Life Science), CLPP (Sigma), anti-GAPDH (14C10) (Cell Signaling), LONP1 (Sigma),

PINK1 (Novus Biologicals), LC3 A/B (Cell Signaling), SDHB (Oxphos cocktail, Abcam), MTCO1 (Abcam), Ubiquitin (Enzo), P62 (BD Transduction Laboratories), Phopsho P62 (Cell Signaling), VDAC (Abcam). In addition to the housekeeping proteins, loading was monitored by Ponceau Red to ensure a homogeneous loading. Antibody detection reactions for all the immunoblot experiments were developed by enhanced chemiluminescence (Advansta) and imaged using the c300 imaging system (Azure Biosystems). Pixel intensity was quantified by using ImageJ software.

Human: Frozen cortex tissue samples were prepared as previously described[51]. Samples were randomized based on diagnostic group and assayed in triplicate. For CLPP, blots were incubated overnight at 4°C with a mouse monoclonal antibody to CLPP (1:1000; clone 2E1D9, ProteinTech) and then incubated for one hour with near-infrared-labeled goat anti-mouse IgG secondary antiserum (IRDye 800LT, 1:10,000; Licor) and analyzed on an Odyssey imaging system (Licor). Following imaging, the membranes were stripped and re-probed with a mouse monoclonal GAPDH antibody (1:10'000; clone 2D9, Origene) overnight followed by 1-hour incubation with near-infrared-labeled goat anti-mouse IgG secondary antiserum and Odyssey imaging. For mtDnaJ/Tid1, blots were incubated overnight at 4°C with both a mouse monoclonal antibody to mtDnaJ/Tid1 (1:500; clone RS13, Cell Signaling) and the GAPDH antibody, followed by goat anti-mouse IgG incubation and Odyssey imaging. Signals for CLPP and mtDnaJ were normalized to GAPDH for quantitative analysis. Details about all the antibodies used are listed in **Supplementary Table 11**.

Citrate synthase activity assay

Citrate synthase (CS) enzymatic activity was determined in mouse cortex samples and *C. elegans* using the CS assay kit (Sigma). Absorbance at 412 nm was recorded on a Victor X4 (PerkinElmer) with 10 readings over the 1.5 min timespan. These readings were in the linear range of enzymatic activity. The difference between baseline and oxaloacetate-treated samples was obtained and used to calculate total citrate synthase activity according to the formula provided in the manual. The obtained values were normalized by the amount of protein used for each sample.

Extraction of the mitochondrial fraction

Cortexes were placed in a homogenizer glass-Teflon potter tubes with 5ml of a buffer prepared adding 10 ml of 0.1MTris–MOPS and 1 ml of EGTA/Tris to 20 ml of 1M sucrose and bringing the volume to 100ml with distilled water. Homogenization was performed at 1600rpm for 5 minutes. The samples were then centrifuged for 10min at 600g and the supernatants were collected. A second centrifugation at the speed of 7000g for 10 min was performed on the supernatants in order to precipitate the mitochondrial fraction. All the steps were performed on ice or at 4°C.

Histology

Brains hemispheres were harvested from anaesthetized mice and immediately frozen in isopentane. 8-µm cryosections were collected and fixed with 4% paraformaldehyde. For immunostainings, sections were stained with 0,01% Thioflavin S (Sigma) for 15min at room temperature, and after washes in ethanol and PBS, stained with Hoechst (Life Technology). After washing in PBS, tissue sections were mounted with Dako mounting medium. Images were acquired using Leica DM 5500 (Leica Microsystems) CMOS camera 2900 Color at the

same exposure time. Quantitative analysis of the immunofluorescence data was carried out by histogram analysis of the fluorescence intensity at each pixel across the images using Image J (Fiji; National Institutes of Health). Appropriate thresholding was employed to all the images of each single experiment to eliminate background signal in the images before histogram analysis. Fluorescence intensity and signal positive areas were calculated using the integrated "analyse particles" tool of the Fiji software, and statistical analysis were performed using Prism 6 (GraphPad Software).

Statistical analyses

Differences between two groups were assessed using two-tailed *t* tests. Differences between more than two groups were assessed by using two-way ANOVA..GraphPad Prism 6 (GraphPad Software, Inc.) was used for all statistical analyses. Variability in all plots and graphs is represented as the s.e.m. All P values < 0.05 were considered to be significant. *$P < 0.05$; **$P \leq 0.01$; ***$P \leq 0.001$; ****$P \leq 0.0001$ instead stated otherwise. All mouse experiments were performed once. Animals that showed signs of severity, predefined by the animal authorizations were euthanized. These animals, together with those who died spontaneously during the experiments, were excluded from the calculations. These criteria were established before starting the experiments. For motility, fitness and death scoring experiments in *C. elegans*, sample size was estimated based on the known variability of the assay. All experiments were done non-blinded and repeated at least twice.

Data availability

All data generated or analysed during this study are included in this published article (and its supplementary information files). Source data for uncropped gels and for all the individual *p* values presented herein are provided with the paper. The expression datasets that support the findings of this study are available in GeneNetwork (www.genenetwork.org) with the identifiers GN327, GN328, GN314[47], and on the Geo Dabatabase (https://www.ncbi.nlm.nih.gov/geo/) with the identifiers (GSE3112, GSE39454)[52,53]. The worm strains generated in this study are available upon request.

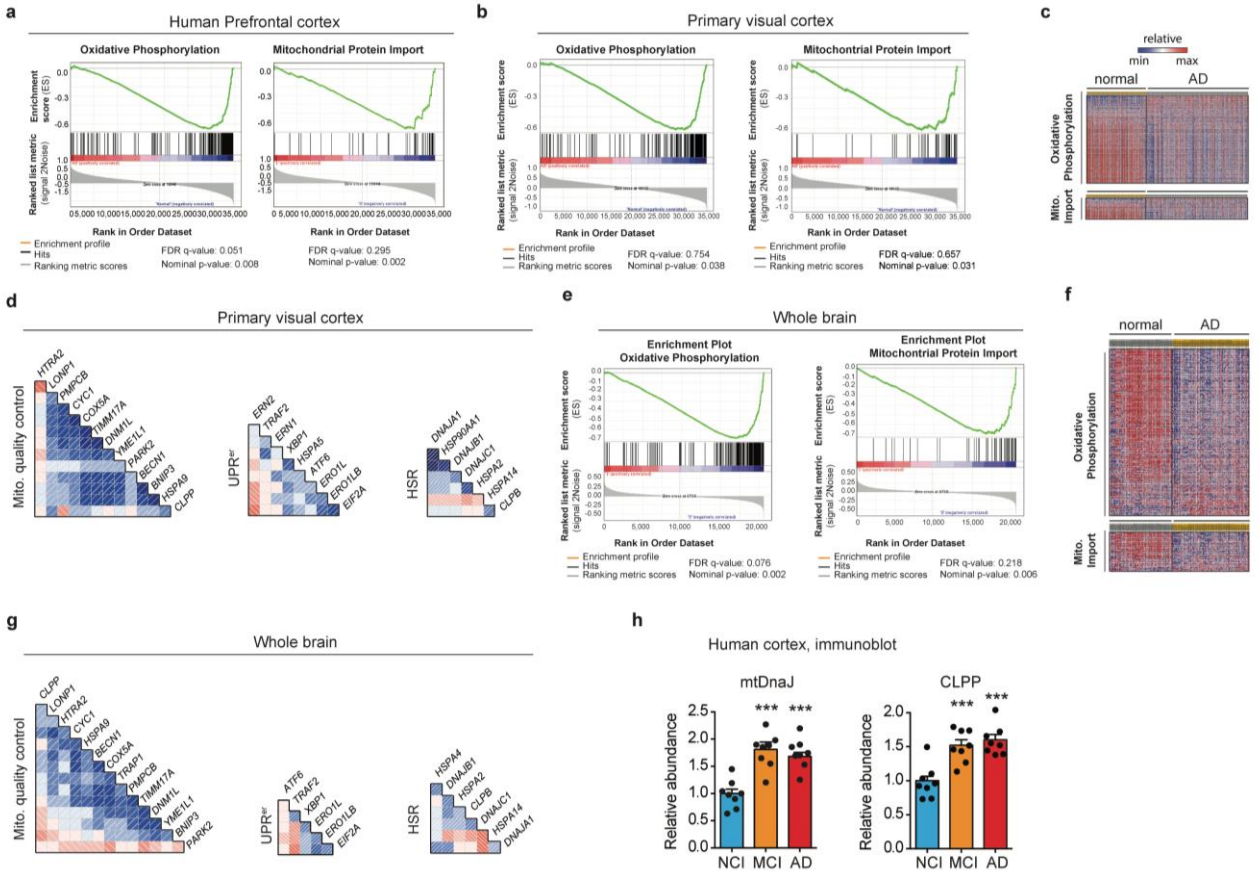

Extended Data Fig. 2.1 | Mitochondrial function pathways are perturbed in AD. a, GSEA of Oxphos (FDR:0.051, nominal-*P*=0.008) and mitochondrial import (FDR:0.295, nominal-*P*=0.002) genes in human AD prefrontal cortex (GN328; normal, *n*=195; AD, *n*=388 individuals). **b-g,** GSEA of Oxphos (FDR:0.754, *P*=0.038) and mitochondrial import (FDR:0.657, *P*=0.031) genes in human Alzheimer visual cortex (GN327, *n*=195 normal and *n*=388 AD individuals) (**b**) and whole brain (GN314, *n*=16 normal and 33 AD individuals) (FDR:0.076, *P*=0.002 for Oxphos, FDR:0.218, *P*=0.006 for mitochondrial import) (**e**). Heatmaps of genes from visual cortex (**c**) and whole brain (**f**) datasets. Correlation plots of mitochondrial stress genes, UPR^{er} and HSR levels in human visual cortex (**d**) and whole brain (**g**) from AD patients. For further information, see **Supplementary Table 5**. **h,** Quantification of immunoblots for mtDNaJ and CLPP (*n*=8 per group) from brains of humans with no cognitive impairment (NCI), mild-cognitive impairment (MCI) and mild/moderate AD. This experiment was performed independently twice. Values in the figure are mean ± s.e.m. ***$P \leq 0.001$. Differences were assessed using two-tailed *t* tests (95% confidence interval). Mito., mitochondrial. For all the individual *p* values, see the **Extended Data Fig. 1 Spreadsheet** file.

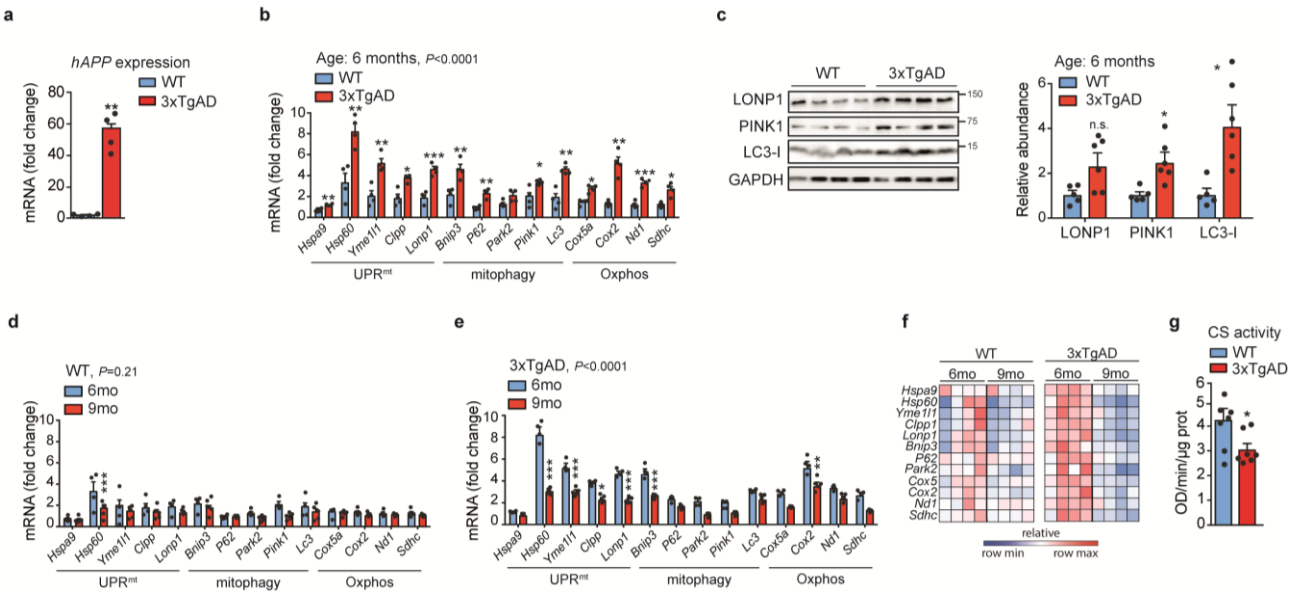

Extended Data Fig. 2.2 | MSR analysis and mitochondrial function in 3xTgAD mice. **a,** Human *APP* expression in cortex tissues of WT and 3xTgAD mice (*n*=4 animals per group). **$P \leq 0.01$ (*P*=0.002). **b,** MSR transcript analysis from cortex tissues of WT (*n*=4 animals) and 3xTgAD mice (*n*=4 animals) at 6 months of age. **c,** Immunoblot analysis (WT, *n*=5; 3xTgAD, *n*=6, WB of 4 representative mice) and

quantification of the same samples as in **b**. **P*<0.05. (*P*=0.035,0.029). **d-f**, MSR transcript analysis from cortex tissues of WT (**d**, 6mo, *n*=4 animals; 9mo, *n*=5 animals) and 3xTgAD mice (**e**, 6mo, *n*=4 animals; 9mo, *n*=5 animals) at 6 and 9 months of age, and corresponding heatmaps (**f**) representing relative variation in gene expression between groups. **g,** CS activity assay in cortex tissues from WT and 3xTgAD mice (WT, *n*=8 animals; 3xTgAD, *n*=7 animals). **P*<0.05 (*P*=0.039). Values in the figure are mean ± s.e.m. **P*<0.05; ***P*≤0.01; ****P*≤0.001; n.s., non-significant. Throughout the figure, overall differences between conditions were assessed by two-way ANOVA. Differences for individual genes, proteins or two groups were assessed using two-tailed *t* tests (95% confidence interval). All experiments were performed independently twice. For uncropped gel source data, see **Supplementary Fig. 1**. For all the individual *p* values, see the **Extended Data Fig. 2 Spreadsheet** file.

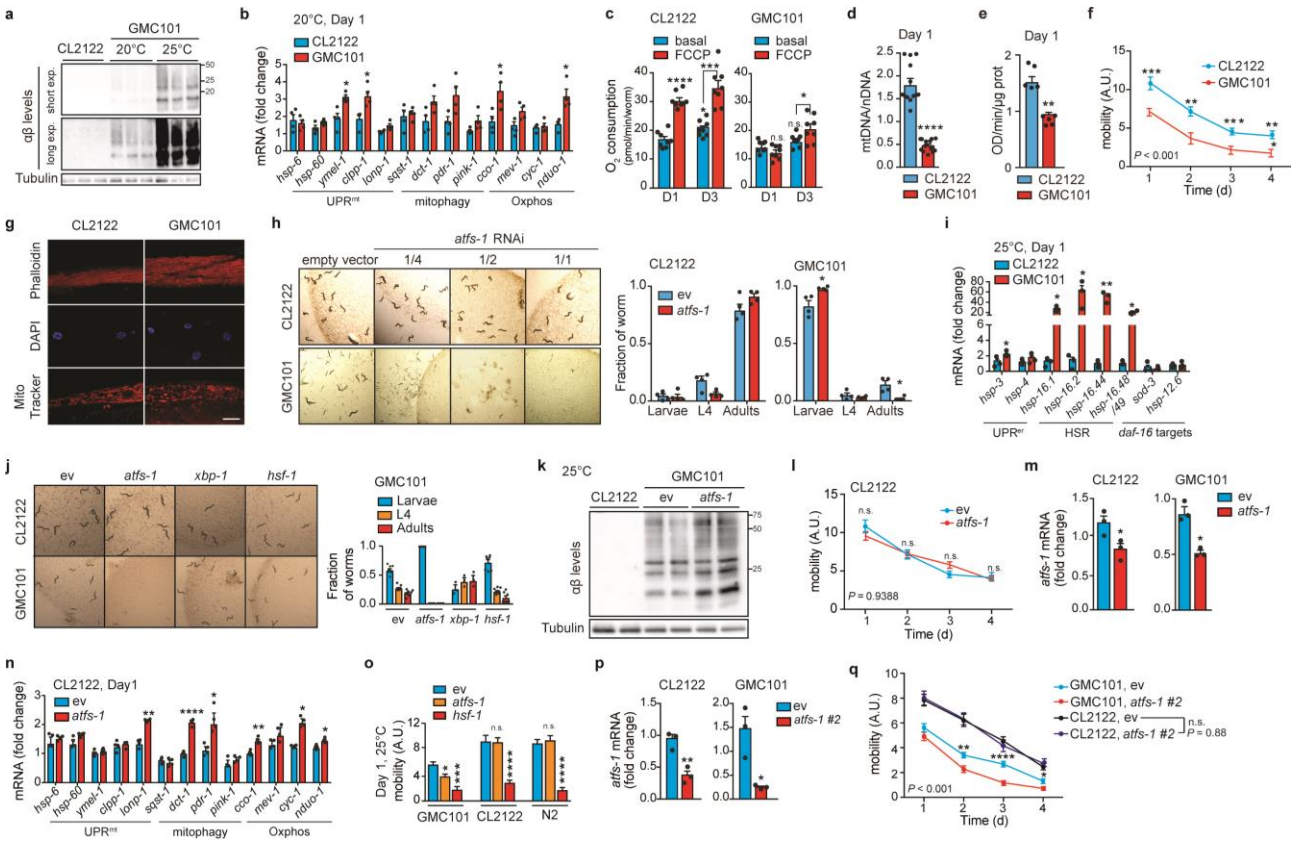

Extended Data Fig. 2.3 | Characterization of Aβ proteotoxicity and stress response pathways in GMC101 worms. a, Amyloid aggregation in CL2122 and GMC101 worms (*n*=3 biologically independent samples) at 20˚C or 25˚C. **b,** MSR transcript analysis in worms at 20˚C (*n*=3 biologically independent samples). **c,** Respiration assay in CL2122 and GMC101 (CL2122, *n*=8; GMC101, *n*=8 biologically independent samples). **d,** mtDNA/nDNA ratio in CL2122 and GMC101 (*n*=13 animals per group). **e,** CS activity in CL2122 and GMC101 on D1 (*n*=5 biologically independent samples). ***P*≤0.01 (*P*=0.004). **f,** CL2122 and GMC101 mobility (CL2122, *n*=48; GMC101, *n*=59 worms). **g,** Confocal images of D1 adult worms showing muscle cell integrity, nuclear morphology and mitochondrial networks. Scale bar, 10µm. See also **Methods**. **h**, Representative images and fraction of worms upon *atfs-1* RNAi (*n*=4 independent experiments). **P*<0.05 (Larvae,0.048; Adults,0.035). **i,** Transcript analysis of UPR^{er}, HSR and *daf-16* target genes (*n*=3 biologically independent samples). **j,** Representative images and fraction of worms fed with *atfs-1, xbp-1* and *hsf-1* RNAis at 20°C (*n*=8 per group; *xbp-1*, *n*=3 biologically independent samples). **k**, Amyloid aggregation upon *atfs-1* RNAi (*n*= 2 biological replicates). **l,** Mobility of CL2122 fed with 50% dilution of *atfs-1* RNAi (ev, *n*=48; *atfs-1*$^{1/2}$, *n*=47 worms). **m,** Validation of the *atfs-1* RNAi in CL2122 and GMC101 (*n*=3 biologically independent samples). **n,** MSR transcript analysis of CL2122 upon *atfs-1* RNAi (*n*=3 biologically independent samples). **o,** Mobility of D1 adult worms fed with *atfs-1* or *hsf-1* RNAi at 25°C (CL2122, *n*=22,27,28; GMC101, *n*=27,21,18; N2, *n*=31,38,27 worms). **p**, Validation of the newly generated *atfs-1#2* RNAi (*n*=3 biologically independent samples). For further information, see **Methods**. **q,** Worm mobility upon *atfs-1#2* RNAi (CL2122, ev, *n*=47; *atfs-1#2*, *n*=42; GMC101, ev, *n*=55; *atfs-1#2*, *n*=46 worms). ev, scrambled RNAi; A.U., arbitrary units. Values in the figure are mean ± s.e.m. **P*<0.05; ***P*≤0.01; ****P*≤0.001; *****P*≤0.0001; n.s., non-significant. Throughout the figure, overall differences between conditions were assessed by two-way ANOVA. Differences for individual genes or two groups were assessed using two-tailed *t* tests (95% confidence interval). All experiments were performed independently at least twice. For uncropped gel source data, see **Supplementary Fig. 1**. For all the individual *p* values, see the **Extended Data Fig. 3 Spreadsheet** file.

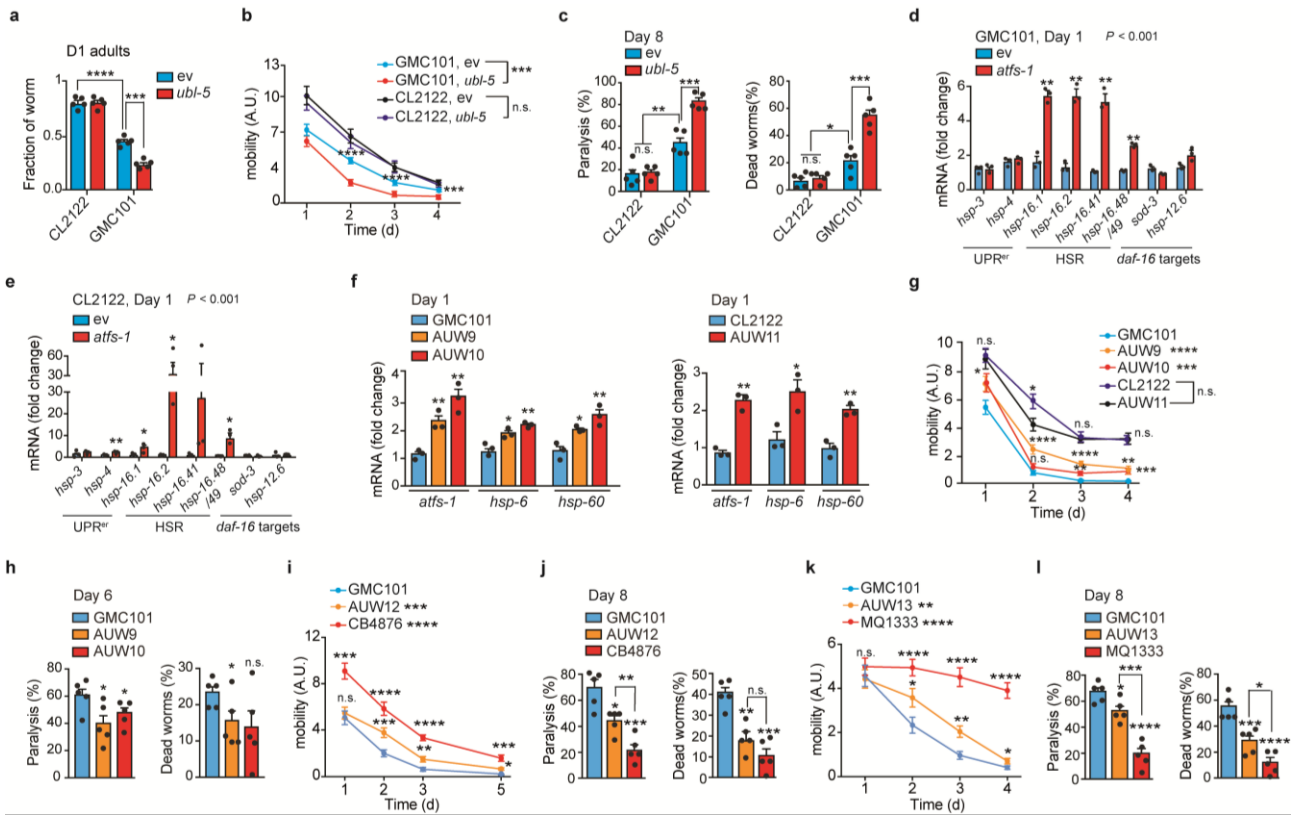

Extended Data Fig. 2.4 | Reliance on *ubl-5* and on increased mitochondrial stress response of GMC101 worms. **a**, Fraction of D1 adult worms fed with *ubl-5* RNAi (*n*=5 biologically independent samples). **b-c,** Mobility of worms (**b**) and percentage of paralyzed and dead D8 adult worms (**c**) upon *ubl-5* RNAi (**b**, CL2122, ev, *n*=39; *ubl-5*, *n*=43; GMC101, ev, *n*=40; *ubl-5*, *n*=41 worms; *n* for **c,** 5 biologically independent samples). **d-e,** Transcript analysis of UPR^{er}, HSR and *daf-16* target genes in GMC101 (**d**) and CL2122 (**e**) upon *atfs-1* RNAi (*n*=3 biologically independent samples) **f,** Validation of the *atfs-1* overexpressing strains AUW9, AUW10 and AUW11 (*n*=3 biologically independent samples). See also **Methods**. **g,** Worm mobility in *atfs-1* overexpressing CL2122- and GMC101-derived lines (CL2122, *n*=40; GMC101, *n*=57; AUW9, *n*=40; AUW10, *n*=38; AUW11, *n*=42 worms). **h,** Percentage of paralyzed and dead D6 adult worms (*n*=5biologically independent samples). **P*<0.05 (*P*=0.019,0.046,0.041). **i-j,** Mobility (**i**) and percentage of paralyzed and dead D8 adult (**j**) GMC101, *clk-1* mutants (CB4876), and AUW12 (**i,** GMC101, *n*= 35; CB4876 *n*=42; AUW12, *n*=38 worms; *n* for **j,** 5 biologically independent samples). **k-l,** Mobility (**k**) and percentage of paralyzed and dead D8 adult (**l**) of GMC101, *nuo-6* mutant (MQ1333), and AUW13 (**k**, GMC101, *n*=46; MQ1333 *n*=50; AUW13, *n*=47 worms; *n* for **l**, *n*=5 biologically independent samples). For further information on all these strains, see **Methods** section. ev, scrambled RNAi; A.U., arbitrary units. Values in the figure are mean ± s.e.m. **P*<0.05; ***P*≤0.01; ****P*≤0.001; *****P*≤0.0001; n.s., non-significant. Throughout the figure, overall differences between conditions were assessed by two-way ANOVA. Differences for individual genes or two groups were assessed using two-tailed *t* tests (95% confidence interval). All experiments were performed independently at least twice. For uncropped gel source data, see **Supplementary Fig. 1**. For all the individual *p* values, see the **Extended Data Fig. 4 Spreadsheet** file.

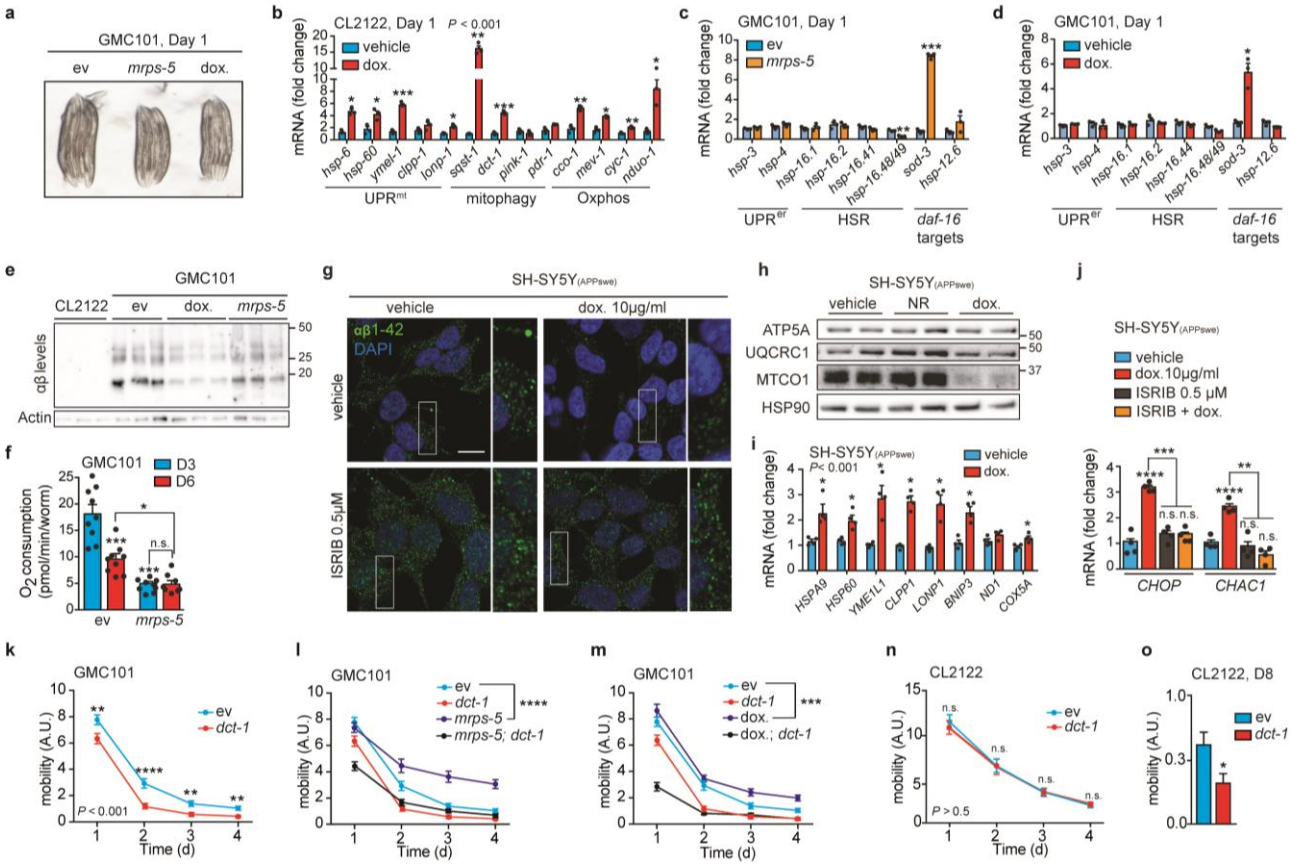

Extended Data Fig. 2.5 | Effects of the inhibition of mitochondrial translation and mitophagy in worms, and of compound treatments in mammalian cells. a, Representative images of GMC101 worms upon *mrps-5* RNAi or dox treatment (15μg/mL) from eggs to D1 (*n*=2 independent experiments). **b,** MSR transcript analysis of dox-treated CL2122 (*n*=4 biologically independent samples). **c-d,** Transcript analysis of UPR^{er}, HSR and *daf-16* target genes in GMC101 fed with *mrps-5* RNAi (**c**), or treated with dox (15μg/mL) (**d**) (**c-d**, *n*=3 biologically independent samples). **e,** Amyloid aggregation in worms upon *mrps-5* RNAi or dox treatment (*n*=3 biologically independent samples). **f**, Respiration on D3 and 6 in GMC101 fed with *mrps-5* RNAi (*n*=9; *mrps-5* D6, *n*=8 biologically independent samples). **g,** Additional confocal images of the SH-SY5Y$_{(APPSwe)}$ cells stained with the anti-β-Amyloid 1-42 antibody, after dox and ISRIB treatment. Scale bar, 10μm. **h**, Oxphos immunoblot of SH-SY5Y$_{(APPSwe)}$ cells showing the effects of NR (1mM) and dox (10μg/mL) (*n*=2 biologically independent samples). **i-j**, Transcript levels of MSR (**i**) and ATF4 target genes (**j**) in APP$_{Swe}$-expressing cell line after 24h of dox (10μg/mL; *n*=4 biologically independent samples). **k,** Mobility of GMC101 upon *dct-1* RNAi (ev, *n*=54; *dct-1*, *n*=44 worms). **l,** Mobility of GMC101 fed with *dct-1*, *mrsp-5,* or both RNAis (ev, *n*=54; *dct-1*, *n*=44; *mrps-5*, *n*=35; *mrps-5*,*dct-1*, *n*=45 worms). **m,** Mobility of GMC101 treated with dox or fed *dct-1* RNAi (ev, *n* =54; *dct-1*, *n*=44; dox, *n*=52; dox,*dct-1*, *n*=54 worms). **n-o**, Mobility of CL2122 fed with *dct-1* RNAi (**n**) from D1 to 4 (ev, *n*=44; *dct-1*, *n*=40 worms), or (**o**) at D8 (*n*=38 worms, **P*<0.05 (0.018)). ev, scrambled RNAi; dox., doxycycline; NR, nicotinamide riboside; ISRIB, integrated stress response inhibitor; A.U. Values in the figure are mean ± s.e.m. **P*<0.05; ***P*≤0.01; ****P*≤0.001; *****P*≤0.0001; n.s., non-significant. Throughout the figure, overall differences between conditions were assessed by two-way ANOVA. Differences for individual genes or two groups were assessed using two-tailed *t* tests (95% confidence interval). All experiments were performed independently at least twice. For uncropped gel source data, see **Supplementary Fig. 1**. For all the individual *p* values, see the **Extended Data Fig. 5 Spreadsheet** file.

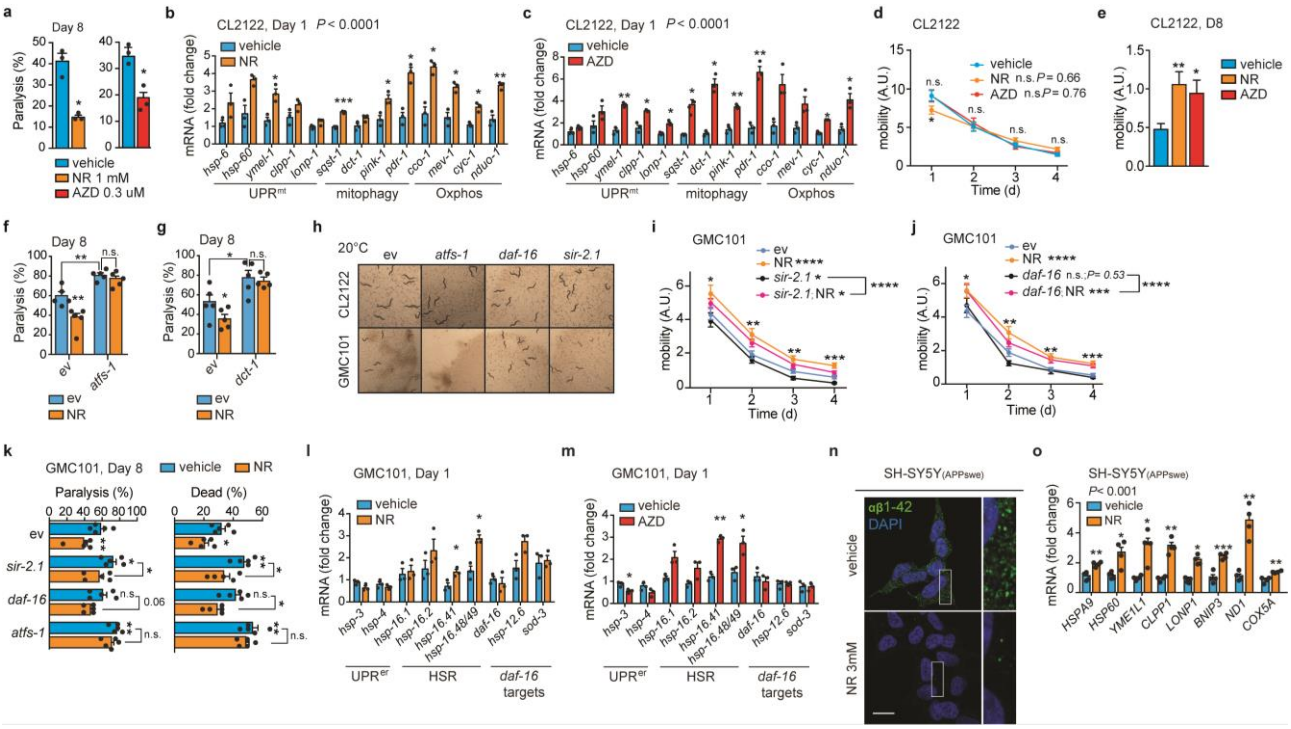

Extended Data Fig. 2.6 | Effect of NAD$^+$-boosting compounds and sirtuin depletion in worms, and NR treatment in mammalian cells. a, Percentage of paralyzed D8 adult GMC101 after NR or AZD (*n*=3 independent experiments). **b-c,** MSR transcript analysis of CL2122 treated with NR (**b**,1mM) or AZD (**c**, 0.3µM) (**b-c**, *n*=3 biologically independent samples). **d-e**, Mobility of CL2122 treated with NR (1mM) or AZD (0.3µM) from (**d**) D1 to 4 (vehicle, *n*=44; NR, *n*=48 ; AZD, *n*=43 worms, or (**e**) at D8 (vehicle, *n*=38; NR, *n*=36; AZD, *n*=33 worms, **P*<0.05 (*P*=0.017); ***P*≤0.01 (*P*=0.004)). **f-g**, Percentage of paralyzed D8 adult GMC101 treated with NR upon *atfs-1* RNAi (**f**) or *dct-1* RNAi (**g**) (*n*=5 biologically independent samples). **h,** Representative images of worms fed with *atfs-1*, *sir-2.1*, and *daf-16* RNAis (*n*=2 independent experiments). **i,** Mobility of NR-treated GMC101 (1mM) fed with *sir-2.1* RNAi (ev, *n*=52; *sir-2.1, n*=37; NR, *n*=40; *sir-2.1,*NR, *n*=51 worms). **j,** Mobility of NR-treated GMC101 (1mM) fed *daf-16* RNAi (ev, *n*=52; *daf-16, n*=43; NR, *n*=40; *daf-16,*NR, *n*=48 worms **k**, Percentage of paralyzed and dead D8 adult GMC101 treated with NR or fed *sir-2.1, daf-16* or *atfs-1* RNAis (*n*=5 biologically independent samples). **l-m,**, Transcript analysis of UPR^{er}, HSR and *daf-16* target genes in GMC101 treated with NR (**l**, 1mM, **P*<0.05 (*P*=0.03,0.008)), or AZD (**m**, 0.3µM, **P*<0.05 (*P*=0.033); ***P*≤0.01 (*P*=0.0004) (*n*=3 biologically independent samples). **n**, Additional confocal images of the intracellular amyloid deposits in the SH-SY5Y$_{(APPSwe)}$ cells after 24 h NR treatment . **o**, Transcript levels of MSR genes in APP$_{Swe}$-expressing cells after NR (1mM) (*n*=4 biologically independent samples). NR, nicotinamide riboside; ISRIB, integrated stress response inhibitor; AZD, Olaparib; ev, scrambled RNAi; A.U., arbitrary units. Values in the figure are mean ± s.e.m. **P*<0.05; ***P*≤0.01; ****P*≤0.001; *****P*≤0.0001; n.s., non-significant. Throughout the figure, overall differences between conditions were assessed by two-way ANOVA. Differences for individual genes or two groups were assessed using two-tailed *t* tests (95% confidence interval). All experiments were performed independently twice. For all the individual *p* values, see the **Extended Data Fig. 6 Spreadsheet** file.

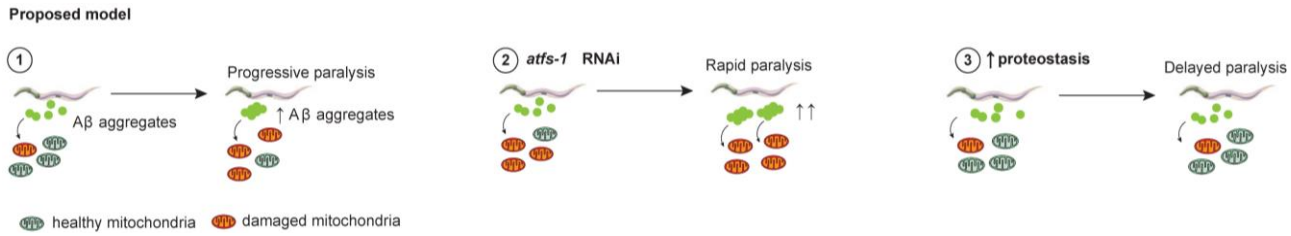

Extended Data Fig. 2.7 | Proposed model. Scheme illustrating the role of mitochondrial proteostasis in Aβ proteopathies based on our studies in the GMC101 model. (1) Accumulation of amyloid aggregates triggers mitochondrial dysfunction, which induces the MSR. (2) *atfs-1* depletion results in loss of mitochondrial homeostasis, more pronounced amyloid aggregation and decreased healthspan. (3) Enhancing mitochondrial proteostasis with dox, *mrps-5* RNAi, and NAD$^+$ boosters (NR and Olaparib), increases organismal fitness, delaying the development of Aβ proteotoxicity.

Acknowledgements We thank P. Gönczy and M. Pierron (EPFL) for sharing reagents, the *Caenorhabditis* Genetics Center, which is funded by NIH Office of Research Infrastructure Programs (P40 OD010440), for providing worm strains. V.S. is supported by the 'EPFL Fellows' program co-funded by Marie Skłodowska-Curie, Horizon 2020 Grant agreement (665667). D.D. is supported by a fellowship funded by Associazione Italiana per la Ricerca sul Cancro (AIRC) and Marie Curie Actions. S.E.C. is supported by NIH grants (P01AG014449, R21AG053581 and P30 AG053760). This research is supported by the EPFL, NIH (R01AG043930), Systems X (SySX.ch 2013/153), Velux Stiftung (1019), and the Swiss National Science Foundation (31003A-140780).

Author contributions V.S. and J.A. conceived and designed the project. V.S., L.M., M.R., J.S.B., H.Z., D.D., F.P., N.M., A.S., S.R., and S.E.C. performed the experiments. V.S., M.R., and L.M. independently replicated worm experiments on figures 2-4. V.S., L.M. and J.A. wrote the manuscript.

Author information Reprints and permissions information is available at www.nature.com/reprints. The authors declare no competing financial interests. Correspondence and requests for materials should be addressed to J.A. (admin.auwerx@epfl.ch).

Chapter 3

NAD^+ boosting reduces age-associated amyloidosis and restores mitochondrial homeostasis in muscle

Mario Romani[1,5], Vincenzo Sorrentino[1,5], Chang-Myung Oh[1,2,3,5], Hao Li[1], Tanes Imamura de Lima[1], Hongbo Zhang[1], Minho Shong[4], Johan Auwerx[1*]

[1]Laboratory of Integrative Systems Physiology, Ecole Polytechnique Fédérale de Lausanne, CH-1015 Lausanne, Switzerland; [2]Department of Endocrinology and Metabolism, CHA Bundang Medical Center, School of Medicine CHA University, Seongnam 13497, South Korea; [3]Department of Biomedical Science and Engineering, Gwangju Institute of Science and Technology, Gwangju 61005, South Korea; [4]Research Center for Endocrine and Metabolic Diseases, Chungnam National University School of Medicine, Daejeon 35015, South Korea

[5]These authors contributed equally to this work

Summary

Aging is characterized by the collapse of cellular proteostasis and mitochondrial homeostasis. Here, we provide mouse and human bioinformatic evidence of dysregulation of mitochondrial and proteostasis pathways in muscle aging and diseases. Moreover, we show accumulation of amyloid-like deposits and mitochondrial dysfunction during natural aging in the body wall muscle of *C. elegans*, in human primary myotubes and in mouse skeletal muscle, which phenocopies some features of inclusion body myositis (IBM), a debilitating age-associated muscle disease. We show here that NAD^+ homeostasis is critical to control amyloid levels in *C. elegans* and mammalian muscle. Treatment of either aged N2 worms, a nematode model of amyloid-beta muscle proteotoxicity, human aged myotubes or old mice with the NAD^+ boosters nicotinamide riboside (NR) and olaparib (AZD), increases mitochondrial function and muscle homeostasis, while attenuating the accumulation of amyloid deposits. Conversely, amyloid binding-based reduction of the aggregation process, by using Thioflavin T (ThT), improves mitochondrial homeostasis in aged worms. Hence, our data reveal that age-related amyloidosis is a contributing factor to mitochondrial dysfunction and that both are features of aging muscle that contribute to frailty. Enhancing NAD^+ metabolism even at the onset of aging normalizes mitochondrial alterations and delays age-associated amyloid formation in muscle, warranting further clinical studies.

Graphical abstract

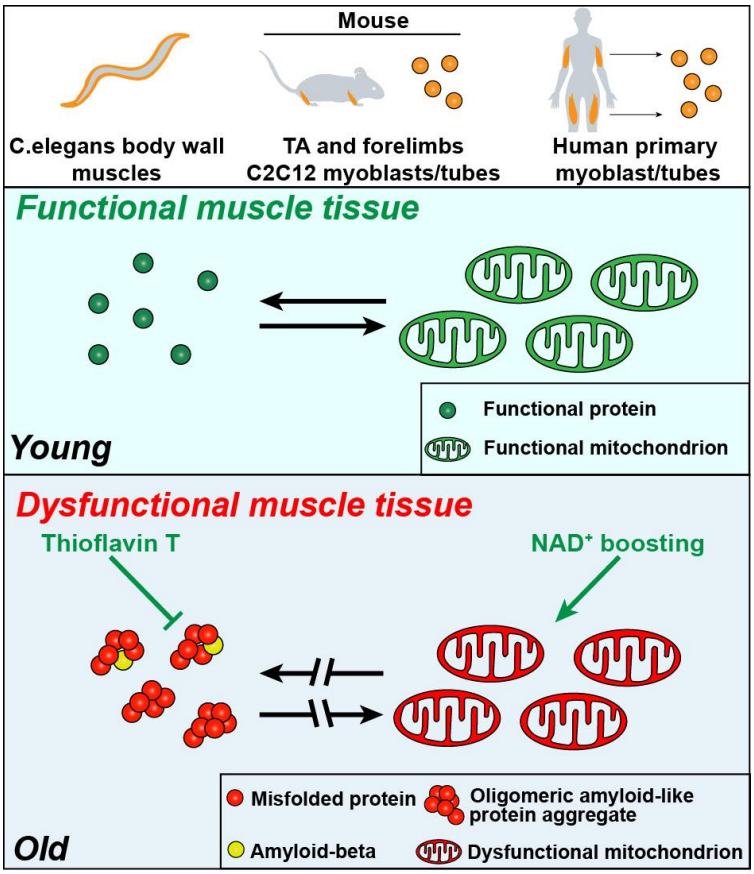

Keywords

Aging, Amyloidosis, Inclusion Body Myositis, NAD^+, Mitochondria, Skeletal Muscle, Proteostasis, Amyloid Beta, Nicotinamide Riboside, Olaparib

Introduction

Aging is a complex, multifactorial, biological process typified by a decline of many cellular functions, including mitochondrial dysfunction and collapse of proteostasis, which ultimately impact on organismal homeostasis [315,316]. Proteostasis includes all cellular processes required to maintain homeostasis of the cellular proteome. These involve regulation of protein synthesis, folding and assembly, and degradation of proteins or aggregates [317].

Due to the fact that mitochondrial function and proteostasis are essential to ensure cellular homeostasis, are functionally interconnected, and decline in aging [315], it is not surprising that mitochondrial dysfunction and abnormal proteostasis are involved in chronic age-associated neuromuscular proteinopathies, such as Alzheimer's disease (AD) [318], and inclusion body myositis (IBM), a debilitating age-associated muscle disease [319,320]. Although affecting different organs, AD and IBM are both protein aggregation diseases characterized by the accumulation of amyloid protein deposits [321]. IBM is the most common muscle proteinopathy affecting the elderly; however, it is generally considered a rare disorder, with its overall prevalence still under debate [322]. Skeletal muscle decay instead is one of the most prominent features of aging, characterized by loss of muscle mass and function [323] and by a decline in mitochondrial function [324]. In addition, muscle aging is also typified by dysfunctional proteostasis pathways, including altered Ubiquitin-Proteasome system (UPS) activity [325] and defective autophagy [326]. Currently, the mechanism underlying the collapse of proteostasis in the aging muscle is not fully elucidated and it is furthermore unclear whether amyloid deposition, a hallmark of IBM, is also at play in the aging muscle.

Here, we report that during natural aging, muscle tissues accumulate amyloid-like deposits, a process which is evolutionary conserved in *C. elegans*, in mouse and human muscle cells and tissues, with molecular features recapitulating some aspects of IBM. Moreover, we also discovered the reversible nature of these deposits, which can be reduced by interventions aimed at restoring mitochondrial homeostasis, such as by enhancing NAD^+ metabolism, even at the onset of aging. Importantly, we show that reduction of the accumulation of amyloid-like deposits in aging is sufficient to improve muscle mitochondrial homeostasis.

Results

Gene signatures of proteostasis and mitochondrial function are altered in muscle aging and diseases

To analyze whether transcriptional signatures associated with protein homeostasis and aggregation and with mitochondria are altered in muscle during aging or diseases, we analyzed transcriptome data from a collection of human muscle datasets of aging, genetic muscle diseases, such as muscle dystrophies, and muscle proteinopathies, such as IBM, polymyositis and amyotrophic lateral sclerosis (ALS) (**Supplementary Table 1**). Gene sets related to mitochondrial respiration and TCA cycle were markedly down-regulated in the majority of the aging and disease conditions (**Fig. 3.1a** and **Supplementary Table 1**), in line with the consensus in the field [319,324,327]. Conversely, gene sets related to protein degradation, such as the UPS, and chaperone-mediated protein folding, were overall up-regulated across the different muscle diseases and in aging (**Fig. 3.1a**). Interestingly, amyloidosis and protein misfolding-related gene sets were among the most consistently induced in all the muscle aging and disease conditions analyzed (**Fig. 3.1a**). This indicates a high similarity between aging- and disease-associated alterations of proteostasis pathways, as highlighted in the volcano plots of selected IBM and aging datasets (**Fig. 3.1b,c** and **Supplementary Table 2**).

We then used the human GTEx muscle datasets (**Fig. 3.1d**, and **Supplementary Table 3**) to confirm our results generated in disease and age-related muscle expression datasets. We separated the GTEx data based on gender and then the age of the subjects was correlated against the expression of genes. We then determined the gene sets correlating with age by using gene set enrichment analysis (GSEA) on the resulting correlation coefficients for all genes [328]. Mitochondrial and proteostasis signatures were also altered in an opposite fashion in GTEx. In agreement with the human data, we observed repression of mitochondrial pathways, mirrored by the induction of protein folding and degradation, but also of aggregation and amyloid formation and regulation, in muscle expression data of mouse models of aging, proteinopathies and dystrophy (**Fig. 3.1e** and **Supplementary Table 4**). Finally, module-module association analysis performed on 12 human muscle datasets using the genetic toolkit GeneBridge [329] indicated that the amyloid-beta formation module has strong negative associations with respiratory electron transport and mitochondrial translation modules (**Fig. 3.1f** top), further pointing at an opposite link between mitochondrial function and amyloid pathways. Module-module association in the mouse, using 11 mouse muscle datasets, also showed similar negative associations (**Fig. 3.1f** bottom).

These analyses hence suggest that there is an overall decline of mitochondrial function paired with perturbed cellular proteostasis in skeletal muscle in established proteinopathies, such as IBM, in aging, as well as in other chronic muscle conditions, including muscular dystrophies. These shared alterations, suggestive of increased protein misfolding and amyloidosis, hence may represent a major common hallmark of muscle aging and disease.

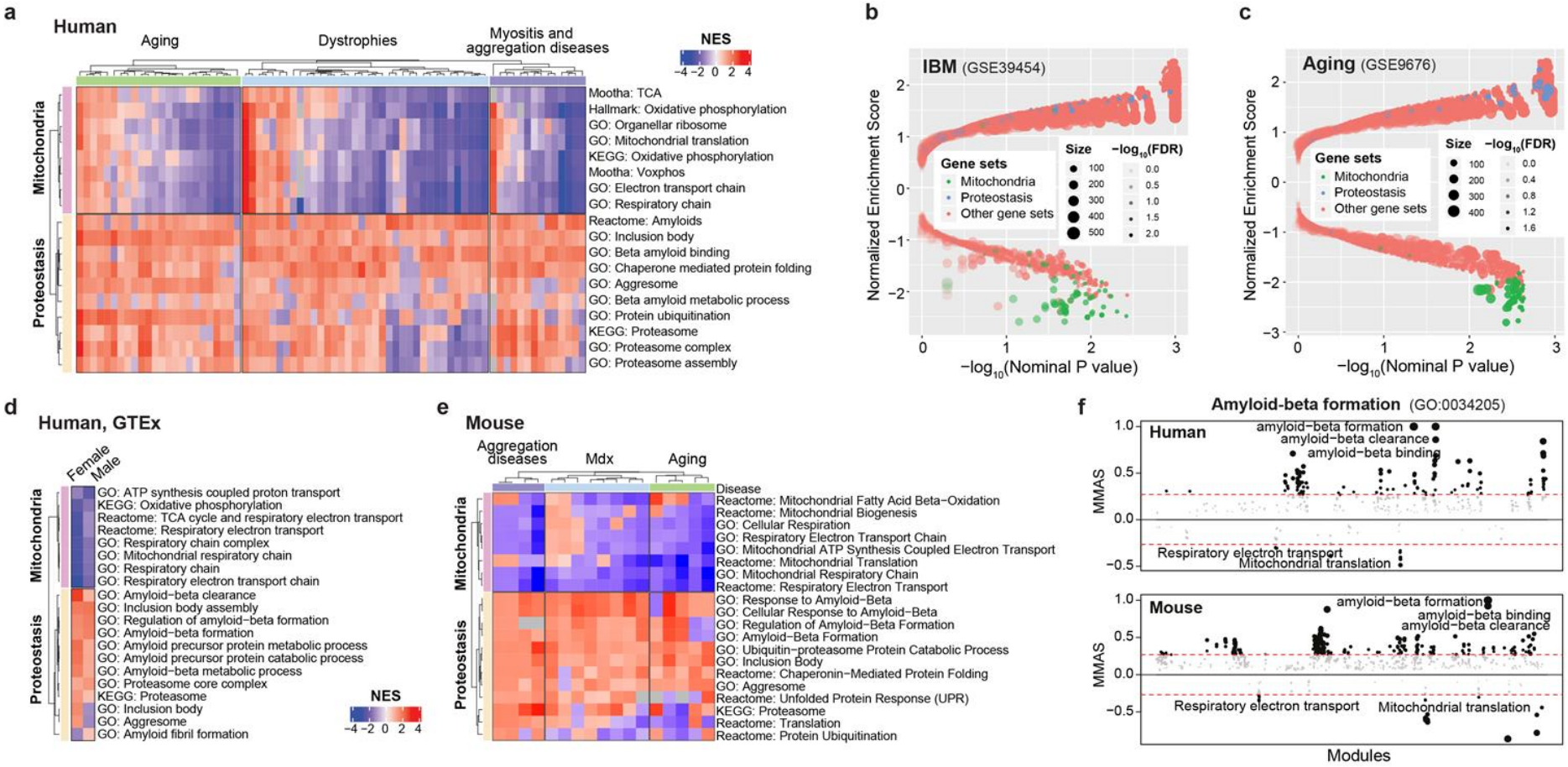
a
Human
Aging
Dystrophies
Myositis and aggregation diseases
NES
−4 −2 0 2 4
Mitochondria
Proteostasis
Mootha: TCA
Hallmark: Oxidative phosphorylation
GO: Organellar ribosome
GO: Mitochondrial translation
KEGG: Oxidative phosphorylation
Mootha: Voxphos
GO: Electron transport chain
GO: Respiratory chain
Reactome: Amyloids
GO: Inclusion body
GO: Beta amyloid binding
GO: Chaperone mediated protein folding
GO: Aggresome
GO: Beta amyloid metabolic process
GO: Protein ubiquitination
KEGG: Proteasome
GO: Proteasome complex
GO: Proteasome assembly
b
IBM (GSE39454)
Normalized Enrichment Score
−log10(Nominal P value)
Gene sets
Mitochondria
Proteostasis
Other gene sets
Size
−log10(FDR)
c
Aging (GSE9676)
Normalized Enrichment Score
−log10(Nominal P value)
Gene sets
Mitochondria
Proteostasis
Other gene sets
Size
−log10(FDR)
d
Human, GTEx
Female
Male
Mitochondria
Proteostasis
GO: ATP synthesis coupled proton transport
KEGG: Oxidative phosphorylation
Reactome: TCA cycle and respiratory electron transport
Reactome: Respiratory electron transport
GO: Respiratory chain complex
GO: Mitochondrial respiratory chain
GO: Respiratory chain
GO: Respiratory electron transport chain
GO: Amyloid−beta clearance
GO: Inclusion body assembly
GO: Regulation of amyloid−beta formation
GO: Amyloid−beta formation
GO: Amyloid precursor protein metabolic process
GO: Amyloid precursor protein catabolic process
GO: Amyloid−beta metabolic process
GO: Proteasome core complex
KEGG: Proteasome
GO: Inclusion body
GO: Aggresome
GO: Amyloid fibril formation
NES
−4 −2 0 2 4
e
Mouse
Aggregation diseases
Mdx
Aging
Disease
Mitochondria
Proteostasis
Reactome: Mitochondrial Fatty Acid Beta−Oxidation
Reactome: Mitochondrial Biogenesis
GO: Cellular Respiration
GO: Respiratory Electron Transport Chain
GO: Mitochondrial ATP Synthesis Coupled Electron Transport
Reactome: Mitochondrial Translation
GO: Mitochondrial Respiratory Chain
Reactome: Respiratory Electron Transport
GO: Response to Amyloid−Beta
GO: Cellular Response to Amyloid−Beta
GO: Regulation of Amyloid−Beta Formation
GO: Amyloid−Beta Formation
GO: Ubiquitin−proteasome Protein Catabolic Process
GO: Inclusion Body
Reactome: Chaperonin−Mediated Protein Folding
GO: Aggresome
Reactome: Unfolded Protein Response (UPR)
KEGG: Proteasome
Reactome: Translation
Reactome: Protein Ubiquitination
f
Amyloid-beta formation (GO:0034205)
Human
amyloid−beta formation
amyloid−beta clearance
amyloid−beta binding
Respiratory electron transport
Mitochondrial translation
MMAS
Mouse
amyloid−beta formation
amyloid−beta binding
amyloid−beta clearance
Respiratory electron transport
Mitochondrial translation
MMAS
Modules

Fig. 3.1 | Mitochondrial and proteostasis transcript signatures are perturbed in aging and muscle disease. a, Heatmap analysis of expression datasets from human muscles during aging and a panel of different muscle diseases. The mitochondrial category of genesets includes sets related to mitochondrial respiration and processes, while proteostasis includes genesets related to the UPS, amyloid-related processes and aggregation. See **Supplementary Table 1**. **b-c,** Volcano plot representations of an IBM (**b**, GSE39454, control, *n*=5; IBM, *n*=10) and a human muscle aging (**c,** GSE9676, young, *n*=14; old, *n*=16) dataset, with the mitochondrial and proteostasis genesets highlighted in green and blue, respectively. See **Supplementary Table 2**. **d,** Heatmap of correlations of mitochondrial and proteostasis genesets with age in the GTEx skeletal muscle expression datasets (male, *n*=316; female, *n*=175). The datasets used for this analysis are listed in **Supplementary Table 3. e,** Heatmap analysis of selected gene expression datasets from mouse muscles during aging and selected muscle diseases. The datasets used for this analysis are listed in **Supplementary Table 4. f,** Module-module association analysis of amyloid beta formation module (GO:0034205) in human and mouse, using 12 and 11 muscle datasets respectively[13]. The threshold of significant module-module connection is indicated by the red dashed line. MMAS, module-module association score.

Muscle aging is characterized by accumulation of amyloid-like deposits across species

Similarly to what is observed in brain tissues affected by AD, IBM is characterized by the accumulation of well-known aggregation-prone proteins, such as amyloid-beta (Aβ) peptides [330]. One common feature of aggregation-prone proteins or peptides is their propensity to form oligomeric aggregates which share a similar conformational status typical of amyloid aggregates [331,332]. However, whether amyloid-based protein deposits might occur in muscle also during physiological aging across different species, is yet to be defined.

Based on these premises and our bioinformatic analysis pointing to the induction of amyloid-related pathways in aging and disease (**Fig. 3.1a-e**), we hence explored whether aging indeed correlated with the accumulation of amyloid-like aggregates in the muscle. First, we analyzed primary myoblasts obtained from 2 healthy young (18 and 25 years old) and 2 aged donors (73 and 82 years old), and from 2 IBM patients (61 years, heterozygote for a *VCP* mutation found in another IBM patient [333], and 73 years, sporadic case), for the presence of these aggregates, using Proteostat-based stainings [334] (**Fig. 3.2a** and **Extended Fig. 3.1a**). The Proteostat dye is reactive towards intracellular aggresomes and related inclusion bodies as well as amyloid-like aggregates [335,336]. Cells from aged donors showed a marked enrichment for the Proteostat signal compared to young donors (**Fig. 3.2a** and **Extended Fig. 3.1a**). These results were corroborated by the increased Proteostat signal in primary cells from IBM patients (**Fig. 3.2a** and **Extended Fig. 3.1a**). This observation is in line with our bioinformatics analysis indicating also the induction of inclusion-bodies-related genesets (**Fig. 3.1a,d,e**). Accordingly, protein aggregates were also detected in the murine muscle cell line C2C12, when over-expressing the amyloidogenic human APP_{Swe} mutant [337,338] (**Fig. 3.2b**, **Extended Fig. 3.1b-d**), along with an altered mitochondrial homeostasis typified by reduced mitochondrial membrane potential (**Fig. 3.2c**) and increased presence of circular mitochondria, suggestive of altered mitochondrial dynamics [339], and by impaired mitochondrial respiration (**Extended Fig. 3.1e,f**). We further validated our observations using the A11 anti-oligomer antibody, which is reactive towards protein aggregates of amyloidogenic nature (conformational epitope), and can be easily implemented in dot blotting assays [340,341]. APP_{Swe}-expressing C2C12 accumulated amyloid deposits (2.06 relative signal compared with empty vector cells), in spite of an equal total protein amount (**Extended Fig. 3.2a,b** and **Supplementary Table 5**), while negative control dot blots, performed in the presence only of the secondary antibody, did not detect aspecific signals (**Extended Fig. 3.2c**), confirming the presence of amyloid-like deposits in the APP_{Swe}-expressing myotubes. To validate our hypothesis also *in vivo*, we tested muscle tissues from young (3 months) and old (2 years) C57BL/6J mice for presence of amyloid-like aggregates, via A11-immunostaining of tibialis anterioris (TA) (**Fig. 3.2d** and **Extended Fig. 3.1g**). Aged muscle displayed a marked accumulation of amyloid oligomers and, importantly, A11 positive aggregates were not detected in interstitial space (**Extended Fig. 3.1g**), in line with intracellular presence of oligomeric aggregates seen also in IBM patients [320]. Additionally, we also investigated protein lysates from forelimb muscles

(**Extended Fig. 3.2d-f** and **Supplementary Table 5**) and TA muscle of young (11 weeks), adult (30 weeks) and old (2 years or 104 weeks) mice (**Extended Fig. 3.2g,h** and **Supplementary Table 5)**. Both muscle groups revealed a specific, strong enrichment for the A11 signal in the old animals (104 old animals compared with 11 weeks old mice had 1,39 increase in A11 signal in TA muscle and 6,08 increase in forelimbs). Altogether, these findings provide evidence for the occurrence of amyloid-like deposits in the aging mammalian muscle.

Recently, the A11 antibody was reported to detect aging-associated aggregates also in *C. elegans* muscles [342]. We therefore performed A11 dot blot analyses on whole-worm protein lysates from adult (day 1) and old (day 11) wild-type N2 worms (as summarized in **Extended Fig. 3.2i**). Lysates from aged N2 showed a marked A11 enrichment compared to young worms (**Fig. 3.2e**) (6,08 relative signal compared with young worms), and this signal was specifically dependent on the presence of the A11 antibody (**Extended Fig. 3.2j,k** and **Supplementary Table 5**). In addition, we performed A11 dot blotting assay on the inducible muscle Aβ proteotoxicity model, GMC101 [343] (day 1), whose proteostasis is hampered by the impairment of mitochondrial homeostasis induced by the RNAi depletion of the UPR^{mt} master regulator *atfs-1* [337] (**Fig. 3.2e**). The amyloid signal, already detectable in GMC101 worms in basal conditions (**Fig. 3.2e: *ev***), was further enhanced by *atfs-1* silencing. Aging in N2 worms also resulted in reduced mitochondrial membrane potential (**Fig. 3.2f**), decreased levels of mitochondrial proteins including the UPR^{mt} effector, HSP-6, and certain OXPHOS components (**Extended Fig. 3.2l**), alteration of mitochondrial networks, with the accumulation of large and circular mitochondria (**Fig. 3.2g**) [344] and in the decay of muscle structural integrity (**Fig. 3.2h**).

Aging is also known to be linked to a decline in NAD^+ levels in muscle tissue in lower organisms and mammals [345,346]. In line with this premise and to investigate whether NAD^+ homeostasis is required to maintain proteostasis, we fed *C. elegans* with bacteria expressing an RNAi targeting *pnc-1,* a key enzyme in NAD^+ salvage in the nematode muscle [347,348]. Genetic attenuation of *pnc-1* function and NAD^+ salvage exacerbated the accumulation of amyloid-like aggregates (1,98 relative signal compared with ev worms) (**Fig. 3.2i** and **Extended Fig. 3.2m**). Moreover, addition of paraquat, an approach which was shown to deplete NAD^+ levels and to reduce lifespan in *C. elegans* [346], also accelerated the loss of proteostasis in day 4 adult worms (**Extended Fig. 3.2n,o**). Similarly, pharmacological blocking NAD^+ salvage using the NAMPT inhibitor, FK866, in APP_{Swe}-expressing C2C12 myoblast [349,350] also robustly induced protein aggregation in these amyloid-producing cells (**Extended Fig. 3.2p**), in line with what observed in nematodes. Collectively, these data confirm that the processes of amyloidosis and aging-associated loss of proteostasis are evolutionary conserved and directly linked to NAD^+ homeostasis. These data furthermore suggest that these processes could be beneficially influenced by mitochondrial or NAD^+-modulating interventions (**Fig. 3.2e-l** and **Extended Fig. 3.2m-p**).

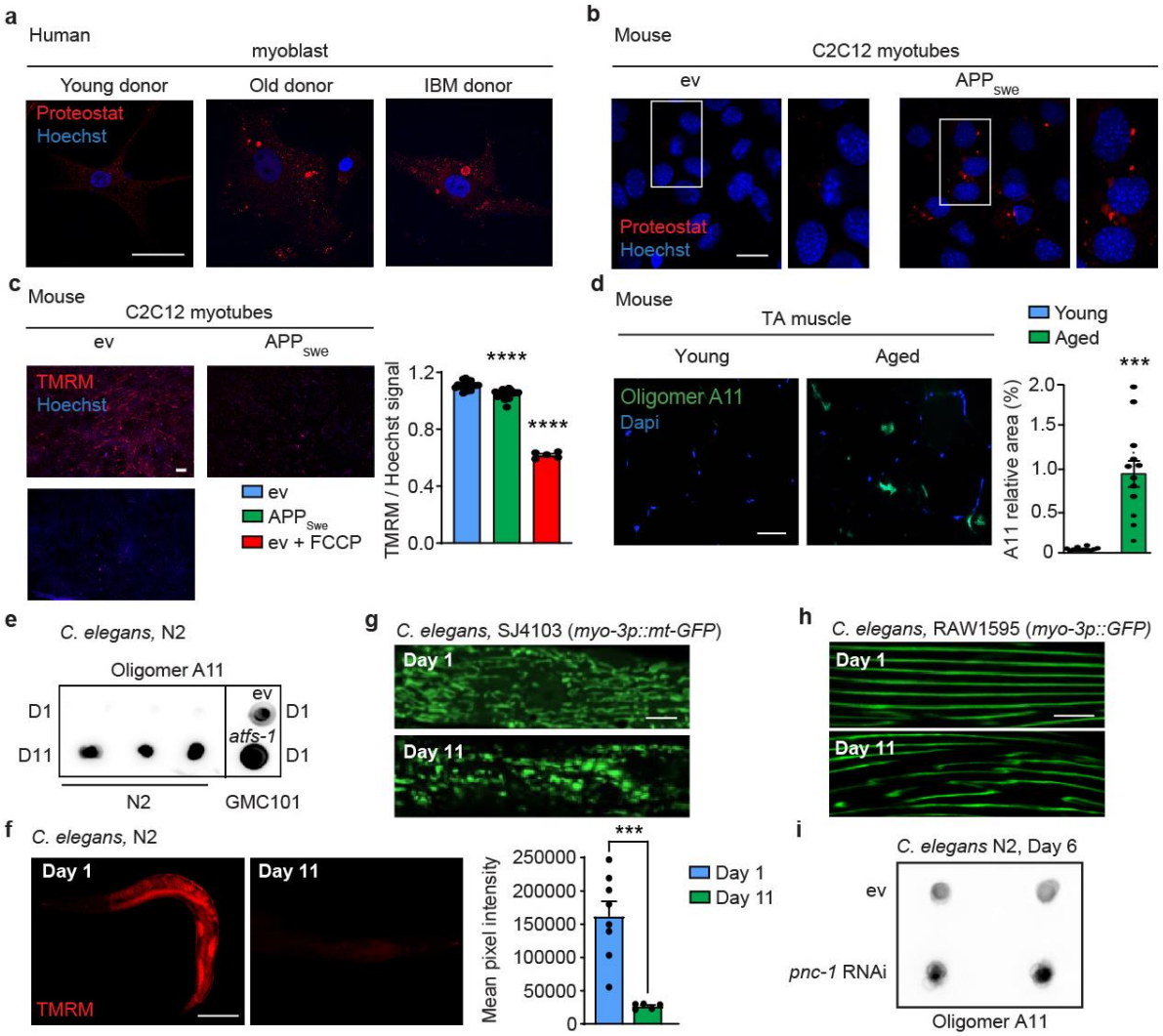

Fig. 3.2 | Accumulation of amyloid-like deposits in aging muscle across species. a-b, Representative confocal images of primary human muscle cells from young, aged and IBM donors (scale bar, 50µm) (**a,** representative images of *n*=2 individuals per group), or of control and APP_{Swe}-expressing C2C12 myotubes (scale bar, 10µm) stained with the Proteostat fluorescent dye (**b,** *n*=3 biological replicates per group). **c**, Microscopy images of TMRM staining of C2C12 ev, C2C12 ev treated with FCCP (10uM, internal control for membrane depolarization) and C2C12 APPSwe (C2C12 ev + Veh, n=17; C2C12 ev + FCCP, n=5; C2C12 APPSwe + Veh, n=20 biological replicates) and relative quantification. Scale bar, 200µm. ****P<0.0001. **d**, Representative images and corresponding quantification of immunostainings of A11 positive deposits in Tibialis anterior (TA) muscles of young (3 months) or aged (24 months) male C57BL/6J mice (*n*=12 animals). Scale bar, 50µm. ***P<0.001 (relative % area). **e**, Dot blot of protein lysates from young (day 1) and aged N2 worms (day 11) (*n*=3 biological replicates per group) and from GMC101 worms, fed with bacteria containing either an empty vector (e.v.) or the *atfs-1* RNAi. Dot blots were stained for the presence of oligomers using the A11 antibody. Relative quantification of the blot intensities is reported in **Supplementary Table 5**. **f**, Confocal images of TMRM staining of young (day 1) and aged (day 11) N2 worms (Day 1, n=8; Day 11, n=5 worms) and relative quantification. Scale bar, 100µm. ***P<0.001. **g**,**h,** Loss of healthy mitochondrial morphology in SJ4103 worms (**h**) and muscle fiber structural decay in the RAW1596 (*myo-3p::GFP*) *C. elegans* strain (**i**) between day 1 and day 11 of aging. **i**, A11 dot blotting of N2 (day 6) worms treated with *pnc-1* RNAi (n=2 biological replicates per group). Relative quantification of the blot intensities is reported in **Supplementary Table 5**. See also **Extended Data Fig. 3.1** and **Extended Data Fig. 3.2.** For all the individual p values, see the **Excel data source Fig. 2.**

Late life treatment with NAD⁺ boosters attenuates amyloid formation and aging phenotypes in *C. elegans*

Given the reversal of mitochondrial dysfunction by life-extending metabolic interventions during aging [346,351] and proteotoxic damage [337,352], the reduced Aβ aggregation and functional improvement in the context of AD following NAD^+ replenishment [337,353], and the increased amyloid-like deposition following NAD^+ depletion (**Fig. 3.2i**) we then tested the impact of the well-known NAD^+ boosters nicotinamide riboside (NR) and the PARP inhibitor

olaparib (AZD), on aging-associated amyloid formation in *C. elegans*. Rather than starting treatment from the embryonic stage, as commonly performed [327,346,354], we only provided the compounds in late adulthood, allowing to bypass all the early effects due to the impact of NAD^+ boosting on development and to only investigate aging-related events (**Extended Fig. 3.3a**). Treating N2 worms with NR (1mM) starting at day 4 of adulthood (**Extended Fig. 3.3a**) induced the expression of the Mitochondrial Stress Response (MSR) signature genes [337] in day 11 old worms (**Fig. 3.3a**), similar to what we previously observed in N2 or in the Aβ aggregation strain GMC101 treated from the egg stage [337]. Additionally, late-life treatment with either NR (1mM) or Olaparib (AZD, 300nM) had a profound effect on proteostasis in aged worms, with amyloid-like deposits levels being reduced by both compounds (0.33 and 0.08 relative signal respectively compared with untreated worms) (**Fig. 3.3b, Extended Fig. 3.3b,c** and **Supplementary Table 5**). Importantly, the NR-mediated reduction of A11 positive aggregates deposition required both *atfs-1* [241,243] and *dct-1* [262] (**Fig. 3.3b**). This confirmed the key contribution of both the UPR^{mt} and mitophagy pathways of the MSR, to cellular proteostasis in line with our previous work on Aβ proteotoxicity [337]. Late-life NAD^+ boosting interventions also restored mitochondrial membrane potential and muscle mitochondrial morphology in aged animals (**Fig. 3.3c,d** and **Extended Fig. 3.3d,e**) and increased mitochondrial DNA content (**Extended Fig. 3.3f**), indicative of increased mitochondrial biogenesis. This furthermore improved fitness, measured as spontaneous movement [355] (**Fig. 3.3e** and **Extended Fig. 3.3g**), muscle integrity (**Fig. 3.3f** and **Extended Fig. 3.3h**) and percentage of paralysis and death at day 18 (**Extended Fig. 3.3i**).

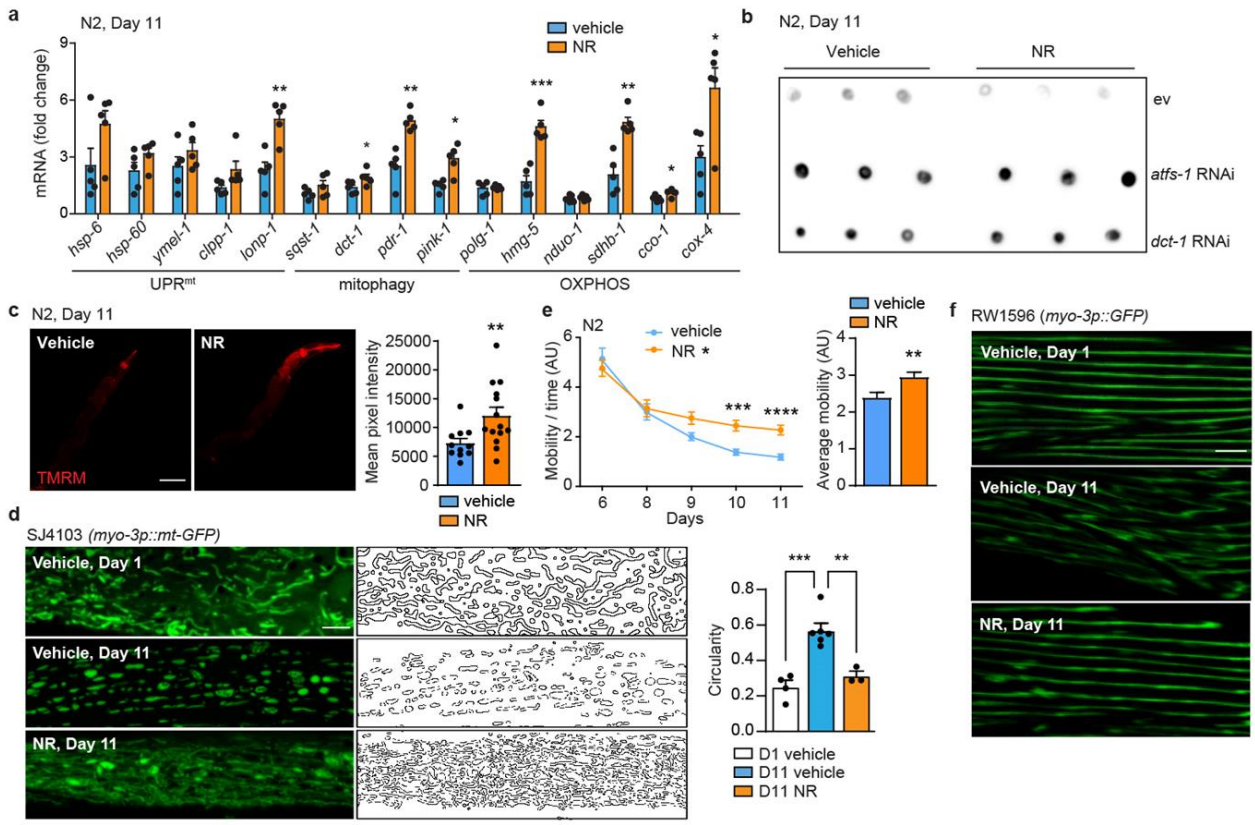

Fig. 3.3 | Boosting NAD^+ levels late in life reduces amyloid-like deposits and improves mitochondrial function and fitness in aged *C. elegans*. a, Transcript analysis of the Mitochondrial Stress Response (MSR) signature (*n*=5 biological replicates) in aged N2 worms treated with nicotinamide riboside (NR; 1mM) from day 4 until day 11 of adulthood. **b**, A11 dot blotting of aged (day 11) N2 worms treated as indicated in **Extended Fig 3a**, with NR (1mM) and fed with either *ev*, *atfs-1* or *dct-1* RNAi (*n*=3 biological replicates per group). Relative quantification of the blot intensities is reported in **Supplementary Table 5**. **c**, Confocal images of TMRM staining of aged (day 11) N2 worms treated as indicated in **Extended Fig 3a**, with NR (1mM) (Vehicle, n=11; NR, n=14 worms) and relative quantification. Scale

bar, 100µm. **d**, Representative confocal images of mitochondrial networks and corresponding morphology analyses including mitochondria outline and circularity assessment (in which 1 represents a perfect circle and 0 a line) in young (day 1) and aged (day 11) SJ4103 (*myo-3p::mt-GFP*) worms treated with NR (1mM) as in **a** (*n*=20 per group). Scale bar, 10µm. **e**, Spontaneous mobility and average mobility of N2 worms treated with vehicle or NR (1mM) as in **a** (vehicle, *n*=55; NR, *n*=49 worms). Overall differences between conditions were assessed by two-way ANOVA (Interaction and Average mobility); differences between conditions at individual time points were assessed using post-hoc Sidak's multiple comparison test. **f**, Confocal images of GFP-labeled muscle fibers in young (day 1) and aged (day 11) RAW1596 (*myo-3p::GFP*) worms treated with NR (1mM) as in **a** (*n*=20 per group). Scale bar, 10µm. See **Methods** for further details. Values in the figure are mean ± s.e.m. **P*<0.05; ***P*≤0.01; ****P*≤0.001; *****P*≤0.0001. Differences for two groups were assessed using two-tailed *t* tests (95% confidence interval) in panel **a**, **c**, and **d.** All experiments were performed independently at least twice. AU, arbitrary units. See also **Extended Data Fig. 2g-i** and **Extended Data Fig. 3.** For all the individual p values, see the **Excel data source Fig. 3.**

Given the beneficial effects on proteostasis observed following boosting of mitochondrial stress responses and function, we decided to test also whether prevention of amyloid-like oligomer accumulation could have a favorable impact on muscle and mitochondrial homeostasis. To test this, we took advantage of the amyloid-binding compound Thioflavin T (ThT); this dye, used to detect protein aggregates, was previously shown to reduce proteotoxicity in *C. elegans* during aging and in models of human proteotoxic disease [342]. The reduction in protein aggregates after ThT was concomitant with a preservation of fitness in nematodes, which is also in line with our results using NAD^+ boosters, showing a simultaneous reduction of amyloid formation and increased fitness in old treated worms (**Fig. 3.3b-f** and **Extended Fig. 3.3b-h).** N2 worms treated with ThT displayed a marked reduction of A11 positive protein aggregates (**Fig. 3.4a**) in agreement with what previously shown [342]. Importantly, we also observed that ThT treatment robustly promoted mitochondrial homeostasis in aging, as shown by higher mitochondrial membrane potential (**Fig. 3.4b**), increased mitochondrial content (**Fig. 3.4c**), and normalized muscle mitochondrial dynamics (**Fig. 3.4d**), to a similar extent to what was observed following administration of NAD^+ boosters (**Fig. 3.3c,d** and **Extended Fig. 3.3d-f**). Collectively, these data indicate that age-associated amyloid-like deposits likely contribute to the mitochondrial dysfunction observed in aged nematodes muscle tissue, and that reducing amyloid formation can be advantageous for mitochondrial homeostasis too (**Fig. 3.4**).

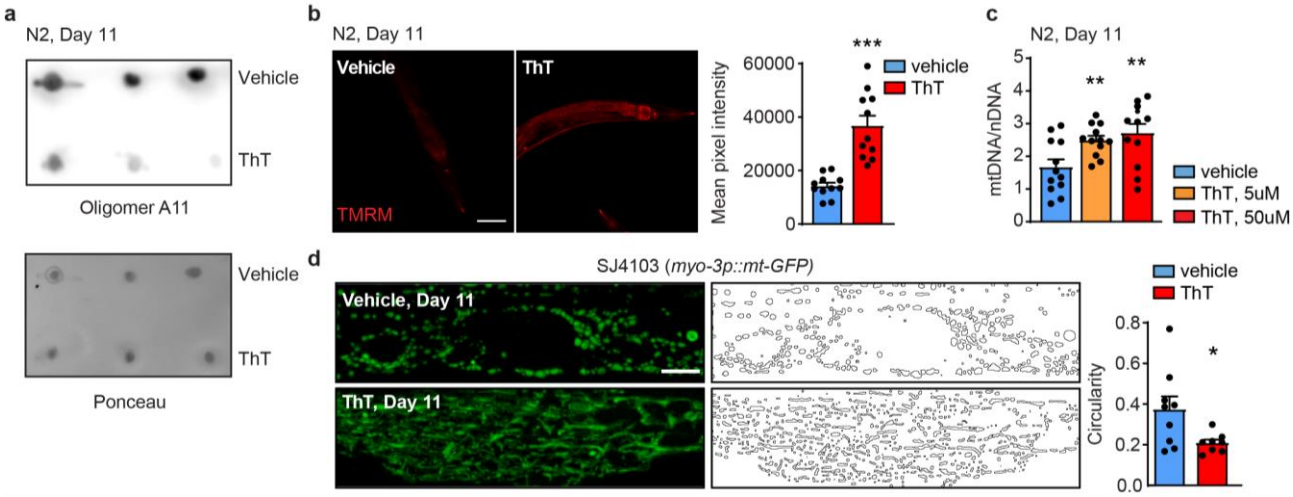

Fig. 3.4 | Thioflavin T prevents amyloid-like accumulation and improves mitochondrial homeostasis in aging. a, A11 dot blotting of aged (day 11) N2 worms treated with ThT (50uM) (n=3 biological replicates per group). Relative quantification of the blot intensities is reported in **Supplementary Table 5**. **b**, Confocal images of TMRM staining of aged (day 11) N2 worms treated ThT (50uM) (Vehicle, n=11; ThT, n=11 worms) and relative quantification. Scale bar, 100µm. **c**, mtDNA/nDNA ratio in aged (day 11) N2 worms treated with ThT (5 or 50uM) (n=12 worms per group). **d**, Representative confocal images of mitochondrial networks and corresponding morphology analyses including mitochondria outline and circularity assessment (in which 1 represents a perfect circle and 0 a line) in aged (day 11) SJ4103 (myo-3p::mt-GFP) worms treated with ThT (5uM) (Vehicle, n=9 ; ThT, n=8 worms). Scale bar, 10µm. Values in the figure are mean ± s.e.m. **P*<0.05; ***P*≤0.01; ****P*≤0.001. For all the individual p values, see the **Excel data source Fig. 4.**

Finally, we verified whether such late-life NAD^+ boosting interventions impact mitochondrial and protein homeostasis in a corrective, rather than preventive, fashion in a severe model of inducible amyloidosis in the worm. To that end, we treated the GMC101 strain during adulthood (starting from day 1) with NR and AZD only after the induction of Aβ aggregation,

achieved by shifting these worms from 20˚C to 25˚C at the L4 stage [337,343] (**Extended Fig. 3.4a**). Onset of amyloidosis in the GMC101 strain reduced worm fitness (**Extended Fig. 3.4b**) and mitochondrial membrane potential (**Extended Fig. 3.4c**) in line with previous work [337]. Moreover, amyloid aggregates accumulation in the AUW15 strain, generated from the cross of GMC101 with the SJ4103 strain expressing mitochondrial GFP in the body wall muscle, also resulted in a marked alteration of mitochondrial morphology when cultured at amyloid-promoting temperature (**Extended Fig. 3.4d**) or when compared to the strain AUW14, derived from a cross between SJ4103 and the control strain CL2122 [337] (**Fig. 3.5b: vehicle** and **Extended Fig. 3.4f: vehicle**). As observed for aged N2 worms, both NR and AZD normalized the mitochondrial membrane potential (**Fig. 3.5a** and **Extended Fig. 3.4e**) and dynamics in the GMC101 worms (**Fig. 3.5b** and **Extended Fig. 3.4f**), but also reduced protein aggregation (0.18 (NR) and 0.1 (AZD) relative signal compared with untreated worms) (**Fig. 3.5c** and **Supplementary Table 5**) and muscle damage (**Fig. 3.5d**), whereas they improved fitness and decreased death at day 8 of adulthood (**Fig. 3.5 e and Extended Fig. 3.4g,h**).

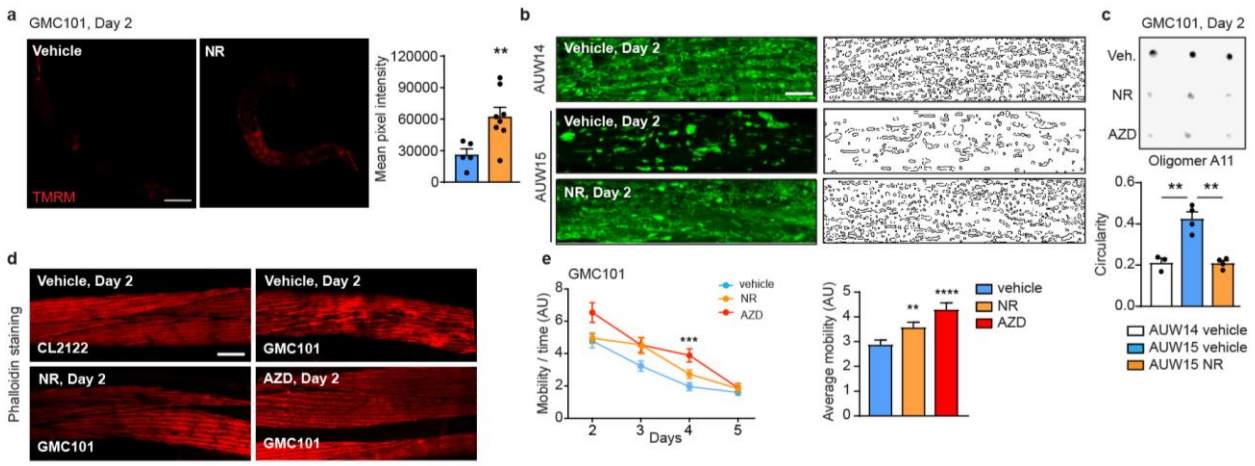

Fig. 3.5 | NAD⁺ boosting after the induction of proteotoxic stress in muscle of Aβ-expressing worms reduces amyloid deposits and improves mitochondria and healthspan. a, Confocal images of TMRM staining of aged (day 11) N2 worms treated ThT (50uM) (Vehicle, n=5 ; NR, n=8 worms) and relative quantification. Scale bar, 100µm. **b,** Representative confocal images of mitochondrial networks at day 2 and corresponding morphology analyses including mitochondria outline and circularity assessment (in which 1 represents a perfect circle and 0 a line), in control AUW14 and $A\beta_{1-42}$ expressing AUW15 worms treated with NR (1mM) and AZD (300 nM) (*n*=20 per group). Scale bar, 10µm. **c,** A11 dot blotting of day 2 GMC101 worms treated as indicated in **Extended Figure 4a**, with NR (1mM) and AZD (300nM) (*n*=3 biological replicates per group). Relative quantification of the blot intensities is reported in **Extended Data Table 5**. **d**, Confocal images of Phalloidin-stained muscle fibers on day 2 in CL2122 (control) and GMC101 worms treated as indicated in **Extended Figure 4a** (*n*=8 worms per group). Scale bar, 10µm. **e**, Spontaneous mobility and average mobiliity of GMC101 treated with vehicle, NR (1mM) or AZD (300nM) as in **Extended Figure 4a** (vehicle, *n*=38; NR, *n*=37 worms; AZD, *n*=36 worms). Overall differences between conditions were assessed by two-way ANOVA (Average mobility); differences between conditions at individual time points were assessed post-hoc Sidak's multiple comparison test. See **Methods** for further details. Values in the figure are mean ± s.e.m. **P*<0.05; ***P*≤0.01; ****P*≤0.001; *****P*≤0.0001. Differences for two groups were assessed using two-tailed *t* tests (95% confidence interval) in panel **a**, **b** (individual time points), **f** and **g**. All experiments were performed independently at least twice. AU, arbitrary units**.** For all the individual p values, see the **Excel data source Fig. 5.**

NAD⁺ boosting reduces amyloid formation and improves mitochondrial parameters during aging in mammals

To translate our findings in *C. elegans* to mammals, we also treated primary human myotubes obtained from aged subjects and IBM patients with NR and AZD, and assessed the presence of amyloid-like proteins by Proteostat staining (**Fig. 3.6a,b** and **Extended Fig. 3.5a,b**). Importantly, both treatments decreased the amount of Proteostat positive signal in cells derived from aged or IBM donors (**Fig. 3.6a,b** and **Extended Fig. 3.5a,b**). Protein aggregates were also reduced in C2C12-APP_{Swe} expressing myotubes following these interventions, both when scored by Proteostat-based staining (**Fig. 3.6c** and **Extended Fig. 3.5c**) and A11 dot blotting (0.4 (NR) and 0.15 (AZD) relative signal compared with untreated

cells) (**Extended Fig. 3.5d,e** and **Supplementary Table 5**). Importantly, co-treating cells with ISRIB, a global integrative stress response (ISR) inhibitor [307], attenuated the reduction in aggregates seen upon NAD^+ boosting (**Extended Fig. 3.5f**). This suggests the involvement of the ISR in resolving amyloid proteotoxic stress in mammalian cells, supporting our worm data (**Fig. 3.3b**). Reduction of amyloid-like deposits was mirrored by an improvement of the mitochondrial membrane potential (**Fig. 3.6d**), increased mitochondrial respiration (**Extended Fig. 3.5g**), and a more reticular mitochondrial network (**Extended Fig. 3.5h**). Together, the data in primary cells and C2C12 cells with Aβ-aggregates confirm that NAD^+ boosting, in addition to its established impact on mitochondrial function, also improves proteostasis and attenuates amyloid formation in mammalian cells.

Given that NR treatment *in vivo* beneficially impacts on mitochondrial and muscle homeostasis (including running performance), healthspan and lifespan in adult [356] and aged mice [357], and reduces brain amyloid plaques in AD mice [337], we assessed the effects of NR on age-associated muscle amyloid-like deposits *in vivo*. Dietary NR supplementation (8 weeks) consistently reduced protein deposits in TA and forelimbs muscles of old C57BL/6J mice as evidenced by A11 immunohistochemistry (**Fig. 3.6e**) and dot blotting (0.45 relative signal compared to untreated animals) (**Extended Fig. 3.5i** and **Supplementary Table 5**). In agreement with our previous work [337], the improved proteostasis after NR treatment was reflected by the increased expression of MSR signature genes in both young and old forelimbs tissues (**Fig. 3.6f** and **Extended Fig. 3.5l**). The expression of the OXPHOS proteins, MTCO1 and SDHB, which were decreased in aged forelimbs, was restored by NR treatment to levels similar to the ones observed in young animals (**Fig. 3.6g**).

To better characterize the composition of muscular age-associated amyloid-like aggregates, and given the fact that APP processing-related pathways appeared to be enriched in aging in skeletal muscle in our bioinformatic analysis (**Fig. 3.1**), we verified whether APP or peptides derived from APP-processing are part of the A11-positive deposits *in vivo*. We took advantage of the anti-Aβ 4G8 antibody, reactive also to murine endogenous APP, its cleavage products and to Aβ [358], and stained 2 types of muscles. Similar to what observed with the A11 antibody, histology analysis of TA muscles revealed increased signals for 4G8 reactive proteins in aged animals, compared to young, which were reduced following NR treatment (**Extended Fig. 3.6a**). Accordingly, accumulation of the 4G8-dependent signal was also reduced in lysates from the forelimbs from aged animals treated with NR (**Extended Fig. 3.6b**). While we cannot conclude which other proteins are part of these protein accumulations in aging, our data suggest that these amyloid-like deposits accumulating in aging muscles also contain APP, APP-byproducts and possibly Aβ, and show that NR treatment decreases the amount of these A11 and 4G8-positive aggregates.

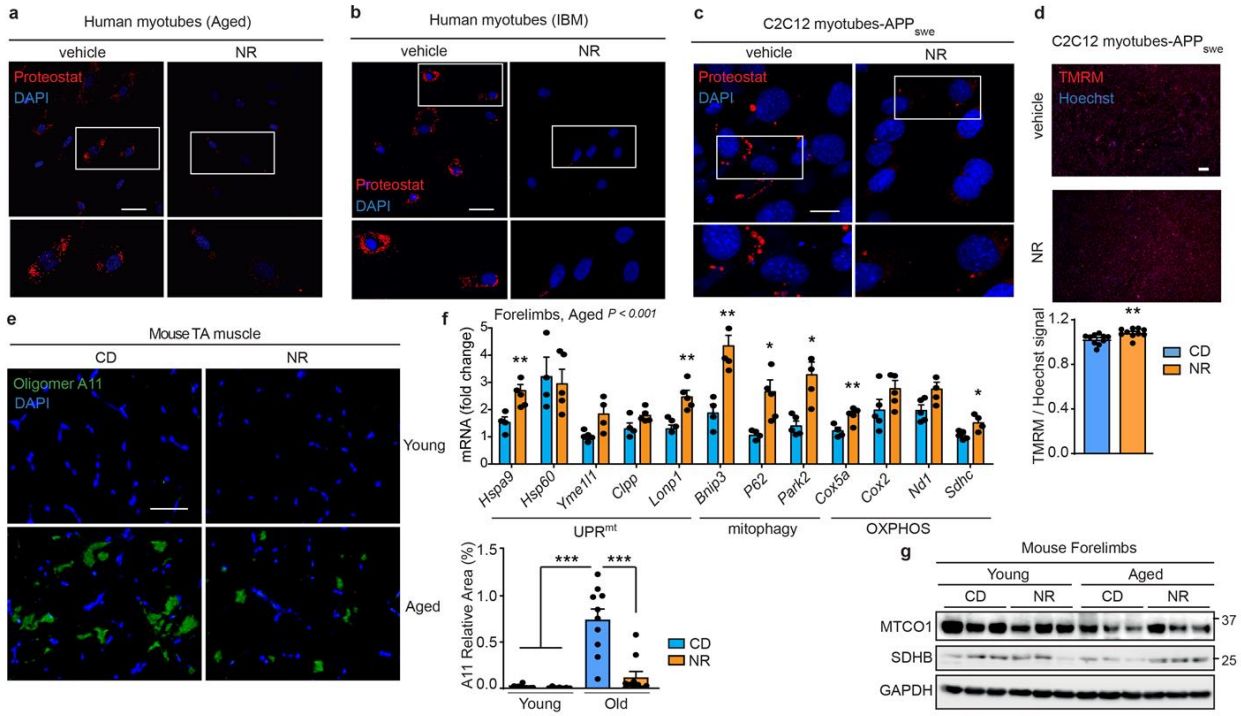

Fig. 3.6 | Boosting NAD$^+$ levels reduces amyloid-like deposits in muscle cells and *in vivo* in aged mice. a-c, Representative confocal images of primary human muscle cells from an aged and an IBM donor, (scale bar, 50µm) (**a,b**), or APP$_{Swe}$-expressing C2C12 myotubes (scale bar, 10µm) (**c**) treated with NR (3mM) and stained with the Proteostat fluorescent dye. See also **Extended Data Fig. 6a-c** for quantification. **d,** Microscopy images of TMRM staining of C2C12 APP$_{Swe}$ treated with NR (3mM) (n=10) and relative quantification. Scale bar, 200µm. **e,** Representative images and corresponding quantification of immunostainings of A11 positive protein deposits in Tibialis anterior (TA) muscles of young or aged male C57BL/6J mice, fed for 8 weeks with chow diet (CD) or chow diet supplemented with NR (400mg/kg/day) (young, *n=12* animals; young+NR, *n=7* animals; old, *n=12* animals; old+NR, *n=11* animals). Scale bar, 50µm. ***P<0.001 (relative % area). **f**, MSR transcript analysis of forelimbs muscles of aged male mice C57BL/6J following NR treatment (n=5 animals per group). **g**, Immunoblot of the Oxphos proteins, MTCO1 and SDHB, from forelimb muscles of the animals in **e** and **Extended data Figure 4 j** (n=3 animals per group). See **Methods** for further details. Values in the figure are mean ± s.e.m. *P<0.05; **P≤0.01; ***P≤0.001. Differences for two groups were assessed using two-tailed t tests (95% confidence interval). For all the individual p values, see the **Excel data source Fig. 6.**

Discussion

Aging is characterized by a collapse of cellular proteostasis and mitochondrial homeostasis, which in the neuro-muscular system is often associated with degenerative disorders, such as AD and IBM, characterized by detrimental protein aggregation [315,316,319,320]. Here, we provided bioinformatic and experimental evidence for the accumulation of amyloid-like deposits and mitochondrial dysfunction during muscle aging across different species, ranging from *C. elegans*, to human primary myotubes and mouse skeletal muscle. Interestingly, muscle aging phenocopies some key molecular features of IBM. These findings therefore indicate that muscle aging involves evolutionary conserved processes whose alteration results not only in mitochondrial dysfunction, but also in the onset of amyloidosis across the tested species. Importantly, our data indicate that prevention of amyloidosis in aging is sufficient to correct age-associated mitochondrial dysfunction, underlining the contribution of these protein aggregates to the general process of muscle aging (**Fig. 3.4**). While it is known that protein aggregation occurs not only in these disorders but can also be present during healthy aging in several species [359–361], the major types of protein aggregates occurring in physiological aging in different organs and tissues are yet to be defined. Recent work in *C. elegans* has shown that certain proteins form age-dependent insoluble aggregates with amyloid-like structure resembling that of protein aggregates observed in amyloidogenic diseases [362]; these observations are in line with our A11 dot blotting data in whole protein lysates from old N2 worms (**Fig. 3.2d**). Although the identity of the proteins forming the A11-positive accumulations we observed, both in aged

worms and mammals in muscle tissues remains to be determined, our data in mouse using the anti-Aβ 4G8 antibody suggest that APP, APP-byproducts and possibly Aβ could compose in part the observed aggregates (**Extended Fig. 3.6a,b**). Interestingly, marked accumulation of 4G8-positive deposits was also detected in brain tissues from aged (24 months) animals, and again decreased following NR supplementation (**Extended Fig. 3.6c**). This last observation is in line with recent work showing increased Proteostat dye reactivity in different brain regions of 24 months old mice [363]; therefore we speculate that similar amyloid-like protein aggregates to those we observed in aged muscles may characterize aging across different tissues. This knowledge will aid to identify novel aging biomarkers and potentially to better understand the aging process.

Our bioinformatic analyses also showed that the mitochondrial and proteostasis alterations observed in aging and IBM also occur in other muscle diseases, such as in various types of myositis and dystrophies (**Fig. 3.1a**). While these conditions are known to present a profound mitochondrial dysfunction [353,364,365], to the best of our knowledge they have not been investigated in depth for the occurrence of alterations in proteostasis that underpin protein aggregation or amyloidosis.

Mitochondrial dysfunction in aging and disease, and Aβ aggregation in the brain during AD, can be reversed by NAD^+ replenishment approaches, such as dietary supplementation with NR and treatment with PARP inhibitors, such as olaparib (AZD) [337,346,353]. Importantly, our current work now shows that direct targeting and reduction of amyloid aggregates using ThT in aged worms (**Fig. 3.4**) restores mitochondrial homeostasis. In addition, we also have demonstrated a critical role of NAD^+ homeostasis to control amyloid aggregates levels (**Fig. 3.2i** and **Extended Fig. 3.2m-p**). Conversely, NAD^+ boosting interventions also improve proteostasis in aging muscle, promoting the reduction of age-associated amyloid-like deposits. Additionally, and in line with our previous work [337], we show that the reversibility of these aggregates in *C. elegans* requires the MSR pathways of UPR^{mt} and mitophagy, and in Aβ-producing C2C12 cells a functional integrative stress response (ISR) (**Fig. 3.3b** and **Extended Fig. 3.5f**). Of note, NR and olaparib treatment decreased Proteostat levels also in primary cells from patients with IBM (**Fig. 3.6b**), an established example of muscle amyloidosis pathology [318]. The results in these cells are also in line with the data, obtained using A11 antibody, from the GMC101 worms (**Fig. 3.5**), which express the human Aβ isoform 1–42 mostly in the muscle, and develop age progressive paralysis, muscle degeneration and amyloid deposition [343]. This worm strain should hence be considered as a general model of Aβ disease that mimics the proteotoxic phenotypes of both AD and IBM. Therefore, our findings in IBM cells and GMC101 worms, supported also by the compound-dependent effects observed in APP_{Swe}-expressing C2C12 (**Fig. 3.6c**), strongly suggest a therapeutic potential for NAD^+ enhancing strategies in treating or delaying the progression of IBM and other amyloidogenic proteinopathies, such as AD [337].

Collectively, our results in *C. elegans*, mice and humans support the notion that natural aging is typified by muscle amyloidosis, and very importantly, that late-life treatments aimed at restoring metabolic and mitochondrial homeostasis also increase cellular and organismal proteostasis, therefore beneficially impacting on health- and lifespan in a more pleiotropic fashion than what reported so far.

STAR Methods

Resource availability

Lead Contact

Further information and requests for resources and reagents should be directed to and will be fulfilled by the Lead Contact, Johan Auwerx (admin.auwerx@epfl.ch).

Materials Availability

The worm strains generated in this study are available upon request from the corresponding author.

Data and Code Availability

All data generated during this study are included in this published article (and its Supplementary Information). Source Data for all the individual P values are provided in **Excel data source table**.
The datasets supporting the current study have been included in **Supplementary Table 1-4**.
The published article includes all datasets generated using GeneBridge: www.systems-genetics.org/mmad.

Experimental model and subject details

Animal experiments and ethical approval

Male 24 months old C57BL/6JRj mice were purchased from Janvier Labs. Mice were fed with pellets containing vehicle or NR (400 mg/kg/day) for 8 weeks. The pellets were prepared by mixing powdered chow diet (2016S, Harlan Laboratories) with water or with NR dissolved in water. Pellets were dried under a laminar flow hood for 48 h. Mice were housed in groups of two to four animals per cage and randomized to 7–8 animals per experimental group according to their body weight. All experiments were performed in compliance with all relevant ethical regulations and authorized by the local animal experimentation committee (Commission cantonale pour l'expérimentation animale) of the Canton de Vaud under license 2890.

Cell culture

The C2C12 cell line expressing the APP Swedish K670N/M671L double mutation (APP_{Swe}) was generated in house. The pCAX $APP_{Swe/Ind}$ plasmid was purchased from Addgene (Plasmid #30145) and the human $APP_{Swe/Ind}$ gene was cloned into pLX304 lentiviral vector (Addgene, Plasmid #25890) by gateway cloning. The newly generated pLX304-$APP_{Swe/Ind}$ vector and lentiviral plasmid packaging mix (pCMV-dR8.2 with pCMV-VSV-G) were transfected into HEK293T cells by Lipofectamine 2000 (Thermo, #11668019). 48 hours after transfection, the cell culture medium was collected as a source of viral particles. Then C2C12 myoblasts were infected with lentivirus-containing medium with polybrene for 24 hours. Cells were selected in 5 µg/ml blasticidin (Sigma-Aldrich, #15205). The C2C12 control and APP_{Swe}-expressing myoblast cells were cultured in high glucose DMEM (Gibco) supplemented with 10% fetal bovine serum (FBS, Gibco), penicillin-streptomycin (1x, Gibco) at 37°C under 5% CO_2. After cells reach confluence, differentiation was initiated by replacing 10% FBS to 2% horse serum. The differentiation media were changed every two days.

Human primary myoblasts lines were purchased from "Hospices Civils de Lyon". VCP IBM myoblasts were derived from a patient with heterozygote variation in the *VCP* gene: c.475C>T (p.Arg159Cys), previously associated with IBM in another study (Watts et al.,

2004). The IBM diagnosis in the patients was validated by the “Hospices Civils de Lyon” through scores for inflammation, p62-positive aggregates in fibers and vacuoles, mitochondrial dysfunction and indicative clinical signs. Cells were grown in DMEM/F-10, supplemented with 12% FBS (Gibco) and penicillin–streptomycin (1×, Gibco). Cells were cultured at 37°C in a 5% CO2 atmosphere and tested for mycoplasma using Mycoprobe (CUL001B, R&D systems).

C. elegans strains and RNAi experiments

C. elegans strains were cultured at 20°C on nematode growth medium (NGM) agar plates seeded with *E. coli* strain OP50 unless stated otherwise. Strains used in this study were the wild-type Bristol N2, SJ4103 (*myo-3::GFP(mit)*), GMC101 (*unc-54p::A-beta-1-42::unc-54 3'-UTR + mtl-2p::GFP*) (McColl et al., 2012), CL2122 *((pPD30.38) unc-54(vector) + (pCL26) mtl-2::GFP*) and RW1596 (*myo-3p::GFP*). Strains were provided by the Caenorhabditis Genetics Center (University of Minnesota). AUW14: (cross *CL2122+SJ4103*) and AUW15: (cross *GMC101+SJ4103*) strains were generated in house. Briefly, for the generation of these lines, SJ4103 males were generated after exposure of L4 worms to 30°C for 5.30 h, and allowed to mate with L4 hermaphrodites from CL2122 or GMC101 mutant strains. The derived progeny was selected for homozygosis of SJ4103 by the presence of GFP in body wall muscle and for homozygosis of CL2122 and GMC101 by the intestinal GFP marker for a few generations. For RNAi experiments, worms were exposed to *atfs-1* and *dct-1* RNAi starting from egg stage to ensure robust knock down of the investigated genes.

Methods details

Bioinformatics analysis

Human or mouse gene expression data from muscle aging or various muscle diseases were obtained from GEO under the respective accession identifiers (**Supplementary Table 1**). To identify the enriched gene sets across the different conditions, we performed gene set enrichment analysis (GSEA) (Subramanian et al., 2005) using the fgsea package (Sergushichev, 2016). Specifically, genes were ranked based on the fold change in muscle aging or muscle diseases against controls, and enriched gene sets were determined by enrichment analysis.

For the analysis using GTEx datasets (GTEx Consortium, 2013), the skeletal muscle RNA-seq data and covariates were obtained from the GTEx Portal (gtexportal.org) under version v7. The expression residuals after accounting for the known and hidden covariates were used for further analysis. To identify the enriched gene sets correlated with age of the sample donors, we ranked the genes based on their Pearson correlation coefficient against age and performed GSEA to determine the enriched gene sets.

The modules associated to the amyloid beta formation (GO:0034205) module were determined using muscle datasets with over 80 samples through GeneBridge at www.systems-genetics.org/mmad (Li et al., 2019).

Imaging and image processing

Confocal images were acquired with Zeiss LSM 700 Upright confocal microscope (Carl Zeiss AG) under non-saturating exposure conditions. The worms were immobilized with 7.5 mM solution of tetramisole hydrochloride (Sigma-Aldrich) in M9 and mounted on 6% agarose pads on glass slides. For immunostaining, cells were fixed with 1× Formal-Fixx (Thermo Scientific) for 15 min. After 15 min permeabilization with 0.1% Triton X-100, cells were

blocked in PBS supplemented with 5% FBS for 1 h and immuno-stained overnight at 4°C the anti-TOM20 antibody or stained using Proteostat. For aggregate detection with this dye, cells were fixed with 4% formaldehyde for 30 min at 21°C. Then cells were washed with PBS, followed by permeabilization for 30 min on ice using permeabilizing solution. Next, the cells were washed twice in PBS and incubated with Proteostat® dye for 30 min at 21°C. Cells were then washed with PBS, covered with glass cover slip, and observed by fluorescence microscopy. Proteostat® Aggresome Detection kit (ENZ-51035-K100) was purchased from Enzo Life Sciences, Inc and all components were prepared according to manufacturer's instruction. For cell immunostaining procedures, the secondary antibody was coupled to an Alexa-488 fluorochrome (Thermo Scientific) and nuclei were stained with DAPI (Invitrogen, D1306). Cell slides were mounted with DAKO mounting medium (DAKO, S3023) and analysed with a Zeiss LSM 700 confocal microscope. Image processing was performed with the Fiji software (http://imagej.nih.gov/ij; version 1.47b).

Mitochondrial circularity

To quantify mitochondrial morphology, we used an ImageJ macro publically available for download from the ImageJ Wiki site (https://imagejdocu.tudor.lu/plugin/morphology/mitochondrial_morphology_macro_plug-in/start) and previously validated(Dagda et al., 2009). Briefly, the color channel of cells stained with TOM20 or worms expressing mito-GFP was extracted to grayscale, inverted to show mitochondria-specific fluorescence as black pixels, and thresholded to optimally resolve individual mitochondria. The macro traces mitochondrial outlines using "analyze particles".

Gene expression analyses in C. elegans and mice

Total RNA was extracted from mouse tissues using TriPure RNA isolation reagent (Roche) according to the product manual. To analyze N2 worms at day 11 of adulthood a total of approximately 3,000 worms per condition, divided into three biological replicates, was recovered in M9 buffer from NGM plates and lysed in the TriPure RNA reagent. Each experiment was repeated twice. Total RNA was transcribed to cDNA using the QuantiTect Reverse Transcription Kit (Qiagen). Expression of selected genes was analysed using the LightCycler480 system (Roche) and LightCycler 480 SYBR Green I Master reagent (Roche). For worms two housekeeping genes were used to normalize the expression data, actin (*act-1*) and peroxisomal membrane protein 3 (*pmp-3*); for mice, the β2-microglobulin (B2m) gene was used as housekeeping reference.

Pharmacological treatment of C. elegans

Nicotinamide riboside triflate (NR) was custom synthesized by Novalix (http://www.novalix-pharma.com/) and dissolved in water, and used at a final concentration of 1 mM. Olaparib (AZD2281) was purchased from Sigma Aldrich dissolved in DMSO to experimental concentrations of 300 nM. Thioflavin T (ThT) was purchased from Sigma-Aldrich (reference T3516-5G) dissolved in methanol and used at final concentrations of 5 and 50 uM (provided from L4 stage). Paraquat was purchased from Sigma-Aldrich (reference 856177), dissolved in water and used at final concentration of 4mM. Compounds were added just before pouring the plates. To ensure a permanent exposure to the compound, plates were changed twice a week.

Worm phenotypic assays

Mobility

C. elegans movement analysis started from day 6 (N2) or day 1 (GMC101) of adulthood, using the Movement Tracker software (Mouchiroud et al., 2016). The experiments were repeated at least twice.

Paralysis and death score

45 to 60 worms per condition were manually scored for paralysis after poking, as described (McColl et al., 2012; Sorrentino et al., 2017). Worms that were unable to respond to any repeated stimulation were scored as dead. Results are representative of data obtained from at least two independent experiments.

TMRM staining

Worms were incubated 24h on NGM agar plates containing TMRM (5uM) added to the medium before pouring the plates. Before imaging, worms were washed 3 times with M9 and incubated 30 minutes on regular NGM agar plates in the dark.

Phalloidin staining

A population of 100 L4 worms was incubated for 24 h at 25°C. The worms were then washed in M9 and frozen in liquid nitrogen. Immediately after, worms were lyophilized using a centrifugal evaporator and permeabilized using acetone. 2 U of phalloidin (Thermo Scientific) was resuspended in 20 µl of a buffer containing: Na-phosphate pH 7.5 (final concentration 0.2 mM), MgCl2 (final concentration 1 mM), SDS (final concentration 0.004%) and dH2O to volume. The worms were incubated for 1 h in the dark and then washed twice in PBS.

Real-time PCR for mitochondrial:nuclear DNA ratio

Relative quantification of the mtDNA copy number in worms was performed by real-time PCR. Relative values for *mtce-26* and *act-3* were compared within each sample to generate a ratio representing the relative level of mitochondrial DNA per nuclear genome. The results obtained were confirmed with a second mitochondrial gene, *nd-1*. The average of at least two technical repeats was used for each biological data point. Each experiment was performed on at least ten independent biological samples.

Cell culture and treatments

Differentiated C2C12 cells were treated with 1uM AZD or 3mM NR in differentiation medium for 24 hours after 4 days differentiation. Human primary cells were treated with AZD or NR after 14 days myotubes differentiation. Then myotubes were collected or fixated for analysis. For TMRM staining, cells were exposed to medium containing TMRM (100 nM final) and Hoechst (5ug/mL) for 30 minutes at 37°C, then washed 3 times with PBS and imaged. Proteostat staining was performed using the manufacturer protocol.

Mitochondrial oxygen consumption

Mitochondrial oxygen consumption rate (OCR) was evaluated using Seahorse analyzer (XF96, Agilent Technologies). OCR was measured using 1 µM of oligomycin to inhibit ATP synthase, 2 µM of the protonophore Carbonyl cyanide p-trifluoromethoxyphenyl hydrazone (FCCP) to uncouple mitochondrial oxidative phosphorylation, and 1 µM rotenone/antimycin to block mitochondrial respiration and determine non-mitochondrial OCR. ATP-linked respiration was calculated by subtracting the uncoupled (after the addition of oligomycin) from the basal OCR. Maximum respiratory capacity was determined after FCCP addition, and spare capacity was determined by subtracting basal from the FCCP-induced OCR. All Seahorse measurements were normalized by protein quantified by Bradford assay.

Western and dot blot analysis

C.elegans were lysed by sonication with TBS buffer containing protease and phosphatase inhibitors (Roche), and analyzed by western and dot blot. The concentration of extracted protein was determined using the Bio-Rad Protein Assay. Membranes were blocked in 10% milk for 2h or overnight. Homogeneous loading was monitored by ponceau red. Antibody detection reactions for all immunoblot experiments were developed by enhanced chemiluminescence (Advansta) and imaged using the c300 imaging system (Azure Biosystems). Each immunoblot experiment was repeated at least twice using at least three biological replicates each containing approximately 1,000 worms.
C2C12 cell lysates were prepared for immunoblotting as for *C.elegans*. Each experiment was repeated at least twice using 3 biological replicates.
For mouse tissues, frozen forelimbs samples were lysed by mechanical homogenization with RIPA buffer containing protease and phosphatase inhibitors for westernblot analysis. Lysates were prepared and analyzed by dot blot as described for worms.

Histology

TA muscles and brains were harvested from anaesthetized mice and immediately frozen in Tissue-TEK® OCT compound (PST). 8-µm cryosections were fixed with 4% paraformaldehyde. For immunostainings, heat activated antigen retrieval was performed in pH 6.0 citrate buffer for 10min at 95°C. After washing with PBS-0.1% tween 20 (PBST), the sections were blocked with 10% affinipure Fab goat anti mouse IgG (Jackson Immunoresearch) in PBS for 60min and PBST containing 2% BSA and 5% goat serum for 30min at room temperature. The primary anti-Oligomer A11 (Thermo Scientific, AHB0052) or anti-Aβ 4G8 (Biolegend, 800701) or laminin (Sigma, L9393) antibodies were then applied over night at 4°C. Subsequently, the slides were washed in PBST and incubated with appropriate secondary antibodies and labeling dyes. For immunofluorescence, secondary antibodies were coupled to Alexa-488 or Alexa-568 fluorochromes (Life technology), and nuclei were stained with DAPI (Invitrogen, D1306). After washing in PBST, tissue sections were mounted with Dako mounting medium (Dako, S3023). Images were acquired using Leica DMI 4000 (Leica Microsystems) or Olympus Slide Scanner VS120 (Olympus) at the same exposure time. Quantitative analysis of the immunofluorescence data was carried out by histogram analysis of the fluorescence intensity at each pixel across the images using Image J (Fiji; National Institutes of Health). Appropriate thresholding was employed to all the images of each single experiment to eliminate background signal in the images before histogram analysis. Fluorescence intensity and signal positive areas were calculated using the integrated “analyse particles” tool of the Fiji software.

Quantification and statistical analysis

No statistical methods were used to predetermine sample size. Differences between two groups were assessed using two-tailed t-tests. Differences between more than two groups were assessed by using two-way ANOVA. Prism 6 (GraphPad Software, Inc.) was used for all statistical analyses. Variability in all plots and graphs is presented as the s.e.m. All $P < 0.05$ were considered to be significant. *$P < 0.05$; **$P \leq 0.01$; ***$P \leq 0.001$; ****$P \leq 0.0001$ unless stated otherwise. All mouse experiments were performed once. Animals that showed signs of severity, predefined by the animal authorizations were euthanized. These animals, together with those who died spontaneously during the experiments, were excluded from the analysis. These criteria were established before starting the experiments. For motility, fitness and death scoring in *C. elegans*, sample size was estimated based on the known variability of the assay. All experiments were done non-blinded and repeated at least twice.

Acknowledgments

We are grateful to the Caenorhabditis Genetics Center for providing worm strains, and to the “Hospices Civils de Lyon” for providing information on the disease characterization of the IBM patients. H.L. is supported by the China Scholarship Council. CM.O. is supported by the Basic Science Research Program through the National Research Foundation of Korea (NRF), which is funded by the Ministry of Education (2016R1A6A3A04010466 to C.M.O). T.L. is supported by FAPESP (2019/11171-7). The research project in the J.A. lab was supported by the EPFL, the European Research Council (ERC-AdG-787702), the Swiss National Science Foundation (SNSF 310030B_160318 and 31003A_179435), the National Research Foundation of Korea (GRL 2017K1A1A2013124), the Fondation Suisse de Recherche sur les Maladies Musculaires (FSRMM), and the Fondation Marcel Levaillant.

Author contributions

M.R., V.S. and J.A. conceived and designed the project. M.R., V.S. and CM.O. performed the experiments. M.R. and V.S. independently replicated worm experiments. CM.O. and T.L. generated the C2C12 APP_{Swe}-expressing cell line. M.R., CM.O. and T.L. performed the cell experiments. H.Z. performed the *in vivo* mouse experiments and H.L. performed the bioinformatics analyses. M.S. provided advice. J.A., CM.O., and M.S. contributed to the funding of the project. V.S., M.R. and J.A. wrote the manuscript, which was edited by all co-authors.

Declaration of Interests

The authors declare no competing interests related to this work.

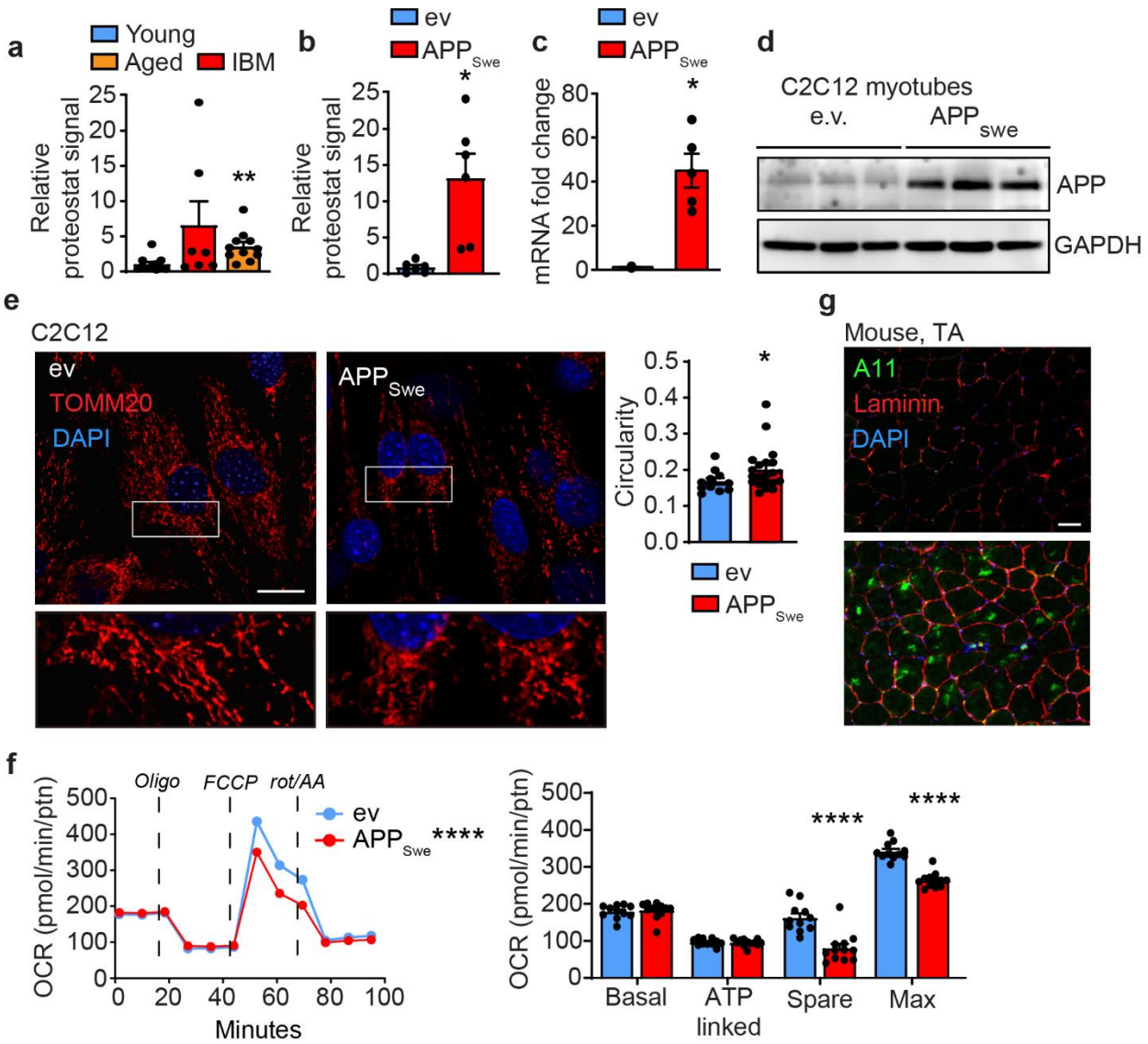

Extended Figure 3.1 | Proteostasis and mitochondrial alterations during aging and proteotoxic stress in muscle cells. a-b, Proteostat signal quantification normalized over the number of cells for experiments shown in **Figure 1a-b** (Young *n=11*, aged *n=7*, IBM *n=11*; C2C12 *n=6*). **c-d,** qRT-PCR RNA analysis (*n*=5 biological replicates) **(c)** and APP immunoblotting (*n*=3 biological replicates) **(d)** of control and APP_{Swe}-expressing C2C12 myotubes. **e**, Confocal images of control and APP_{Swe}-expressing C2C12 myotubes, stained using a TOMM20 antibody to reveal the mitochondrial network and relative circularity assessment (in which 1 represents a perfect circle and 0 a line) (scale bar, 50µm). **f**, Oxygen consumption rates in C2C12ev or APP_{Swe}-expressing C2C12 myoblasts treated with oligomycin (Oligo), FCCP and rotenone/antimycin A (Rot-AA). Error bars represent the mean ± SEM. **e**, Representative images of immunostainings of laminin and A11 positive deposits in Tibialis anterior (TA) muscles of young (3 months) or aged (24 months) male C57BL/6J mice. All experiments were performed independently at least twice. See **Methods** for further details. Values in the figure are mean ± s.e.m. *P<0.05; ****P≤0.0001.. For all the individual p values, see the **Excel data source Extended Fig. 1.**

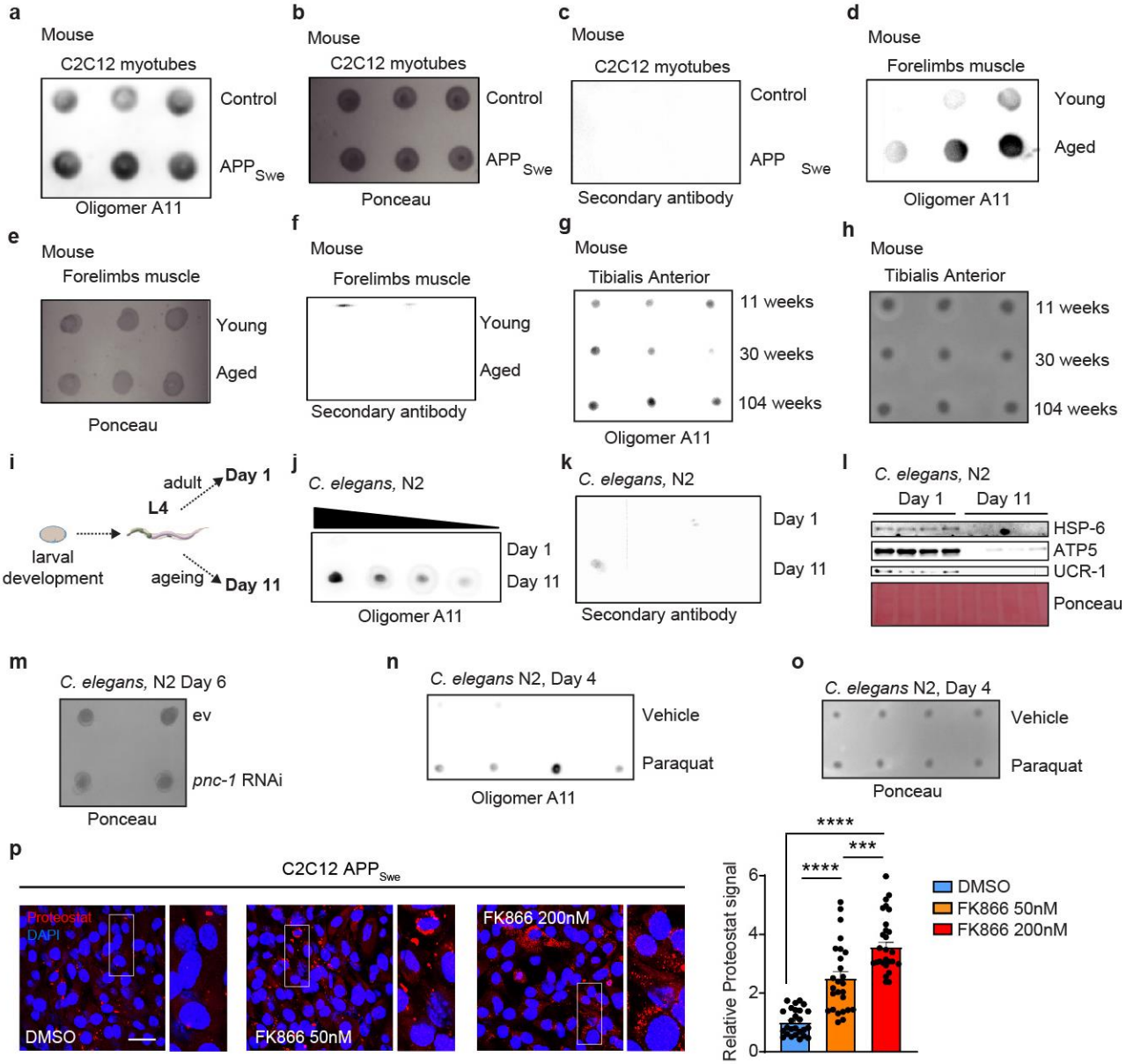

Extended Figure 3.2 | Dot blotting to detect amyloid-like deposits in mouse muscle and in *C. elegans*. a,d,g, Dot blot analyses based on A11 antibody detection of protein lysates from control and APP_{Swe}-expressing C2C12 myotubes (**a**, *n*=3 biological replicates per group), young (3 months) and old (24 months) male C57BL/6J mice (**d**, *n*=3 mice per group) and 11, 30 or 104 weeks old male C57BL/6J mice (**g**, *n*=3 mice per group). Relative quantification of the blot intensities is reported in **Extended Data Table 5**. **b,e,h,** Ponceau staining, as a loading control, of the membranes loaded with protein lysates from control and APP_{Swe}-expressing C2C12 cells (**b**, *n*=3 biological replicates per group), young and old mice (**e**, *n*=3 mice per group), and 11, 30 or 104 weeks old mice(**h**, *n*=3 mice per group). These blots correspond to **a**, **d** and **h**. **c,f,** Control experiment for the dot blotting analysis of the same samples as in **a** and **d**, using only the secondary antibody. **i,** Schematic for the *C. elegans* experimental observations in **Figure 2e,g,h,i** and **Extended Figure 2 j,k,m** using young (day 1) and aged (day 11) N2 worms. **j,** Serial dilutions of 1 biological sample from young (day 1) and aged (day 11) N2 worms, showing the specificity of detection of the A11 antibody in worm protein lysates. **k,** Control experiment for the dot blotting analysis of the samples in **Figure 2k**, using only the secondary antibody. **l,** Immunoblot of the mitochondrial proteins HSP-6, ATP5 and UCR-1 from young and old N2 worms. **m,** Ponceau staining, as a loading control, of the membrane loaded with protein lysates from **Figure 2i**. **n-o,** A11 dot blotting of N2 (day 4) worms treated with paraquat (50uM) (n=4 biological replicates per group) and relative ponceau staining. Relative quantification of the blot intensities is reported in **Supplementary Table 5**. **p,** Representative confocal images and relative quantification of APP_{Swe}-expressing C2C12 myoblasts (scale bar, 10µm) treated with FK866 (50 or 200nM) and stained with the Proteostat fluorescent dye. All experiments were performed independently twice. Values in the figure are mean ± s.e.m. ***P≤0.001; ****P≤0.0001. For all the individual p values, see the **Excel data source Extended Fig. 2**.

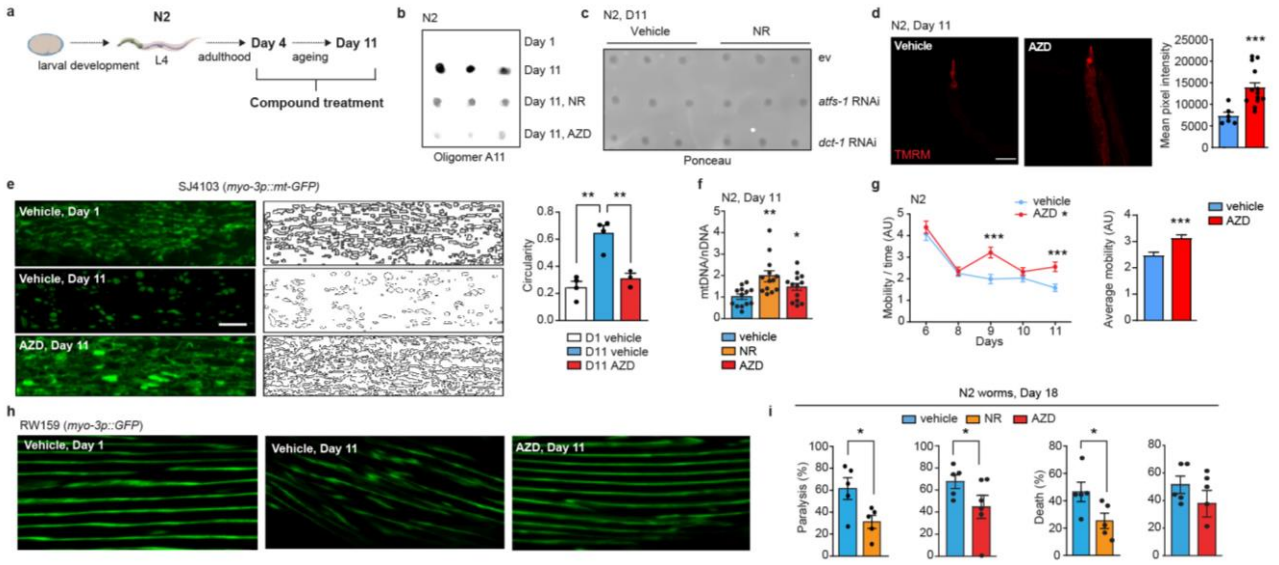

Extended Figure 3.3 | AZD treatment improves mitochondrial and fitness parameters in aged *C. elegans*. a, Scheme of the experimental design including compound interventions during aging in N2 worms. **b**, A11 dot blotting of young (day 1) and aged (day 11) N2 worms treated as indicated in **a**, with NR (1mM) and a PARP inhibitor (AZD; 300nM) (*n*=3 biological replicates per group). Day 1 and day 11 samples are the same as **Fig 2e**. Relative quantification of the blot intensities is reported in **Supplementary Table 5**. **c**, Ponceau staining, as a loading control, of the membrane loaded with protein lysates from **Figure 3b**. **d**, Confocal images of TMRM staining of aged (day 11) N2 worms treated as indicated in **Extended Fig 3a**, with AZD (300uM) (Vehicle, n=6; AZD, n=13 worms) and relative quantification. Scale bar, 100µm. **e**, Confocal images of mitochondrial networks and corresponding morphology analyses including mitochondria outline and circularity assessment (in which 1 represents a perfect circle and 0 a line) in young (day 1) and aged (day 11) SJ4103 (*myo-3p::mt-GFP*) worms treated with AZD (300 nM) following the experimental pipeline shown in **Fig. 3a** (D1, *n*=3; D11, *n*=4; D11 AZD, *n*=3). Scale bar, 10µm. **f**, mtDNA/nDNA ratio in N2 worms treated with NR (1mM) and AZD (300 nM) (*n*=13 animals per group). **g**, Spontaneous mobility and average mobility of N2 worms treated with vehicle or AZD (300 nM) as in **a** (vehicle, *n*=70; AZD, *n*=80 worms). Overall differences between conditions were assessed by two-way ANOVA (Average mobility); differences between conditions at individual time points were assessed using post hoc Sidak's multiple comparison test. **h**, Confocal images of GFP-labeled muscle fibers in young (day 1) and aged (day 11) RAW1596 (*myo-3p::GFP*) worms treated with AZD (300 nM) as in **a** (*n*=20 per group). Scale bar, 10µm. **i**, Percentage of paralyzed and dead D18 N2 worms after vehicle or AZD treatment (*n*=5 biological replicates). See **Methods** for further details. Values in the figure are mean ± s.e.m. **P*<0.05; ***P*≤0.01; ****P*≤0.001. Differences for two groups were assessed using two-tailed *t* tests (95% confidence interval) in panel **a**, **b**, **d**, and **e**. All experiments were performed independently at least twice. AU, arbitrary units. For all the individual p values, see the **Excel data source Extended Fig. 3**.

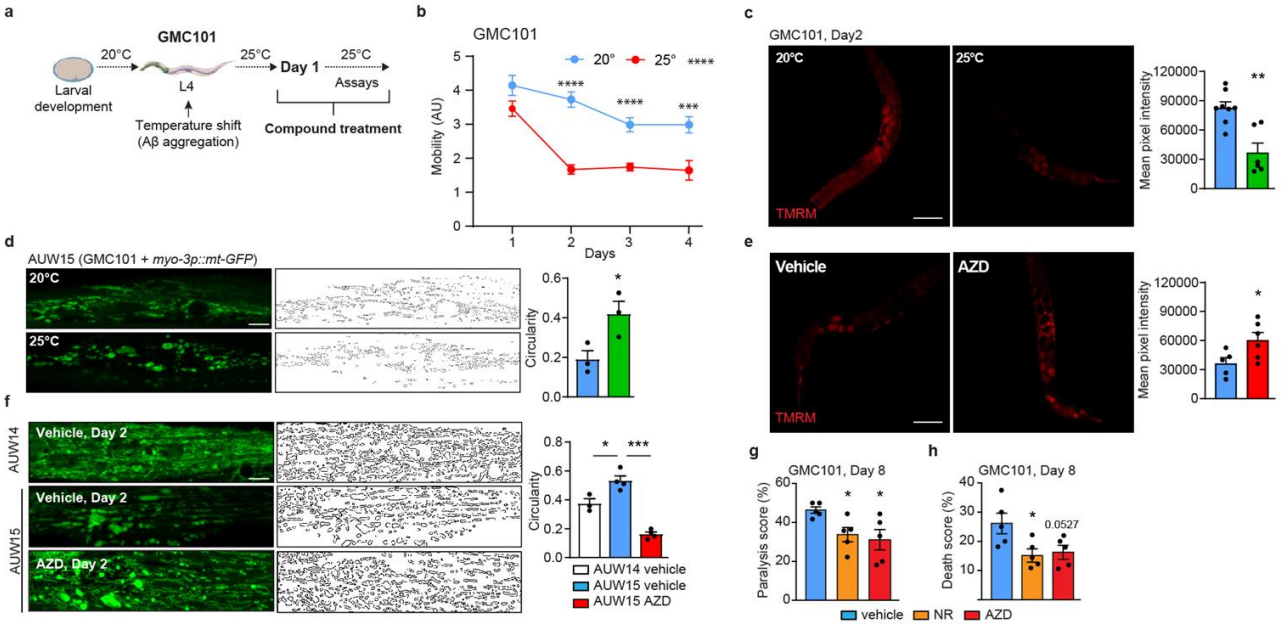

Extended Figure 3.4 | AZD beneficially impacts on Aβ -associated mitochondrial dysfunction in *C.elegans*. a, Scheme of the experimental design including activation of Aβ-aggregation and compound interventions in GMC101 worms. **b**, Spontaneous mobility of GMC101 worms cultured at 20° or 25°C as in **a** (20°C, *n*=46; 25°C, *n*=43 worms). Overall differences between conditions were assessed by two-way ANOVA; differences between conditions at individual time points were assessed using post hoc Sidak's multiple comparison test. **c**, Confocal images of TMRM staining of day 2 GMC101 worms cultured at 20° or 25°C (20°C, *n*=8; 25°C, *n*=6 worms) and relative quantification. Scale bar, 100µm. **d**, Confocal images of mitochondrial networks and corresponding morphology analyses including

mitochondria outline and circularity assessment (in which 1 represents a perfect circle and 0 a line) in Day 2 AUW15 (GMC101 + *myo-3p::mt-GFP*) worms cultured at 20° or 25°C (*n*=3 per group). Scale bar, 10µm. **e**, Confocal images of TMRM staining of day 2 GMC101 worms cultured at 25°C and treated with AZD (300nM) as in **a** (Vehicle, n=5; AZD, n=6 worms) and relative quantification. Scale bar, 100µm. **f**, Confocal images of mitochondrial networks and corresponding morphology analyses including mitochondria outline and circularity assessment (in which 1 represents a perfect circle and 0 a line) in Day 2 AUW14 (CL2122 + *myo-3p::mt-GFP*) and AUW15 (GMC101 + *myo-3p::mt-GFP*) worms cultured at 25°C and treated with AZD (300nM) as in **a** (AUW14, *n*=3; AUW15 Vehicle, *n*=4; AUW15 AZD, *n*=4 worms). Scale bar, 10µm. **g-h**, Percentage of paralyzed (**f**) and dead (**g**) D8 GMC101 worms after compound treatment (*n*=5 biological replicates). For all the individual p values, see the **Excel data source Extended Fig. 3**. Values in the figure are mean ± s.e.m. **P*<0.05; ***P*≤0.01; ****P*≤0.001; *****P*≤0.0001.

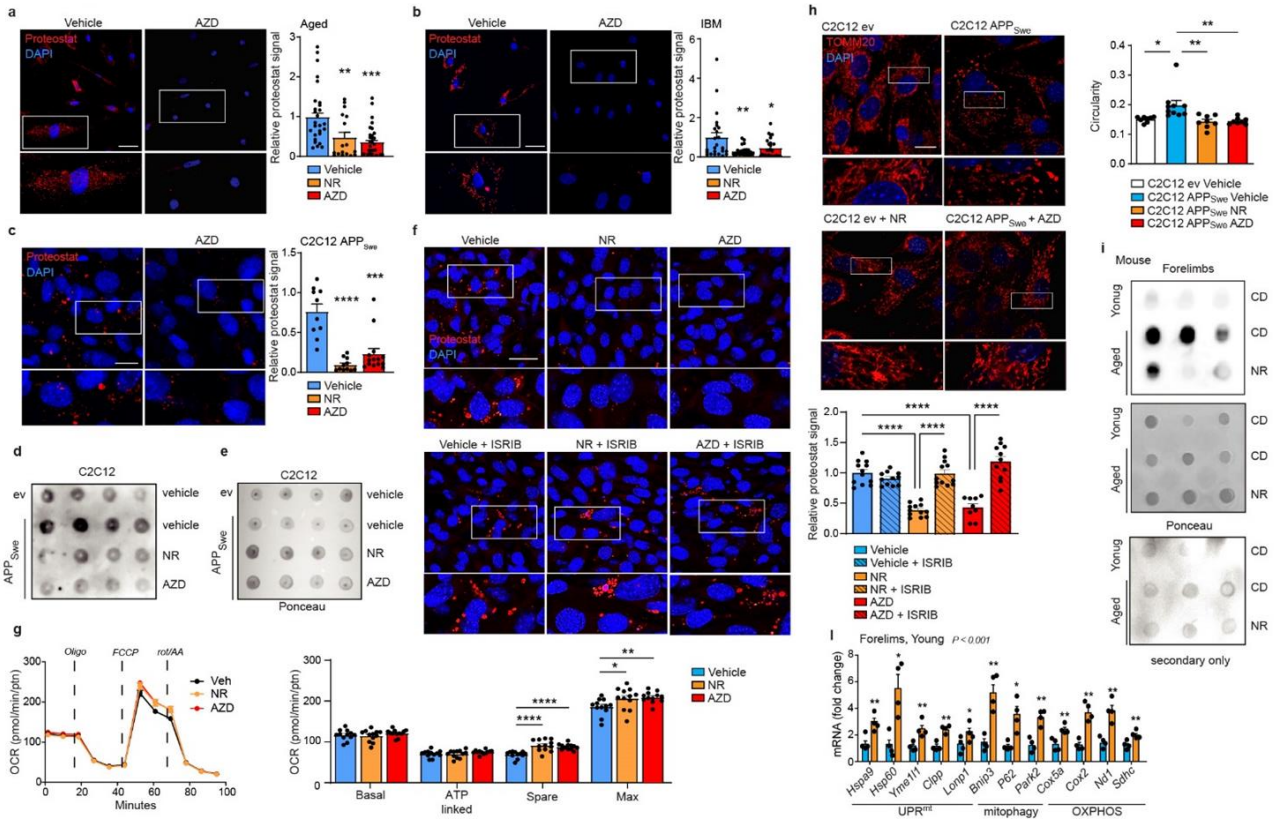

Extended Figure 3.5 | NAD$^+$ boosting interventions and their effects on proteostasis and mitochondria in cells and in vivo. a-c, Representative confocal images of primary human muscle cells from an aged and an IBM donor, (scale bar, 50µm) (**a,b**), or APP$_{Swe}$-expressing C2C12 myotubes (scale bar, 10µm) (**c**) treated with AZD (1uM) and stained with the Proteostat fluorescent dye and relative Proteostat signal quantification normalized on the number of cells for experiments shown in **Figure 5a-c** (Aged+vehicle *n=34*, aged+NR *n=17*, aged+AZD *n=33*; IBM+vehicle *n=25*, IBM+NR *n=25*, IBM+AZD *n=31*; C2C12+Vehicle *n=11*, C2C12+NR *n=11*, C2C12+AZD *n=14*). **d,e**, A11 dot blot analyses of protein lysates from APP$_{Swe}$-expressing C2C12 myotubes (*n*=4 biological replicates per group) after compound treatment (NR, 3mM; AZD, 1uM) and relative ponceau control. Relative quantification of the blot intensities is reported in **Extended Data Table 5**. **f**, Representative confocal images of APP$_{Swe}$-expressing C2C12 myoblast (scale bar, 10µm) treated with NR (1mM), AZD (1uM), and ISRIB (0,5uM) and stained with the Proteostat fluorescent dye and relative Proteostat signal quantification normalized on the number of cells (Vehicle *n=13*, Vehicle + ISRIB *n=11*, NR *n=12*, NR + ISRIB *n=12*, AZD *n=9*, AZD + ISRIB *n=11*). **g**, Oxygen consumption rates in C2C12ev or APP$_{Swe}$-expressing C2C12 myoblasts treated with NR (3mM) or AZD (1uM) and oligomycin (Oligo), FCCP and rotenone/antimycin A (Rot-AA). Error bars represent the mean ± SEM. **h**, Representative confocal images of control and APP$_{Swe}$-expressing C2C12 myotubes and corresponding morphology analyses including mitochondria outline and circularity assessment (in which 1 represents a perfect circle and 0 a line) after compound treatment (NR, 3mM; AZD, 1uM), stained using a TOMM20 antibody to reveal the mitochondrial network (scale bar, 50µm). **i**, A11 dot blot analyses and relative controls of protein lysates from young (3 months) and old (24 months) male C57BL/6J mice (*n*=3 mice per group) in control conditions and after compound treatment (NR, 3mM). Relative quantification of the blot intensities is reported in **Extended Data Table 5**. **l**, MSR transcript analysis of forelimbs muscles of young male mice C57BL/6J following NR treatment (*n*=4 animals). For all the individual p values, see the **Excel data source Extended Fig. 5.** Values in the figure are mean ± s.e.m. **P*<0.05; ***P*≤0.01; ****P*≤0.001; *****P*≤0.0001.

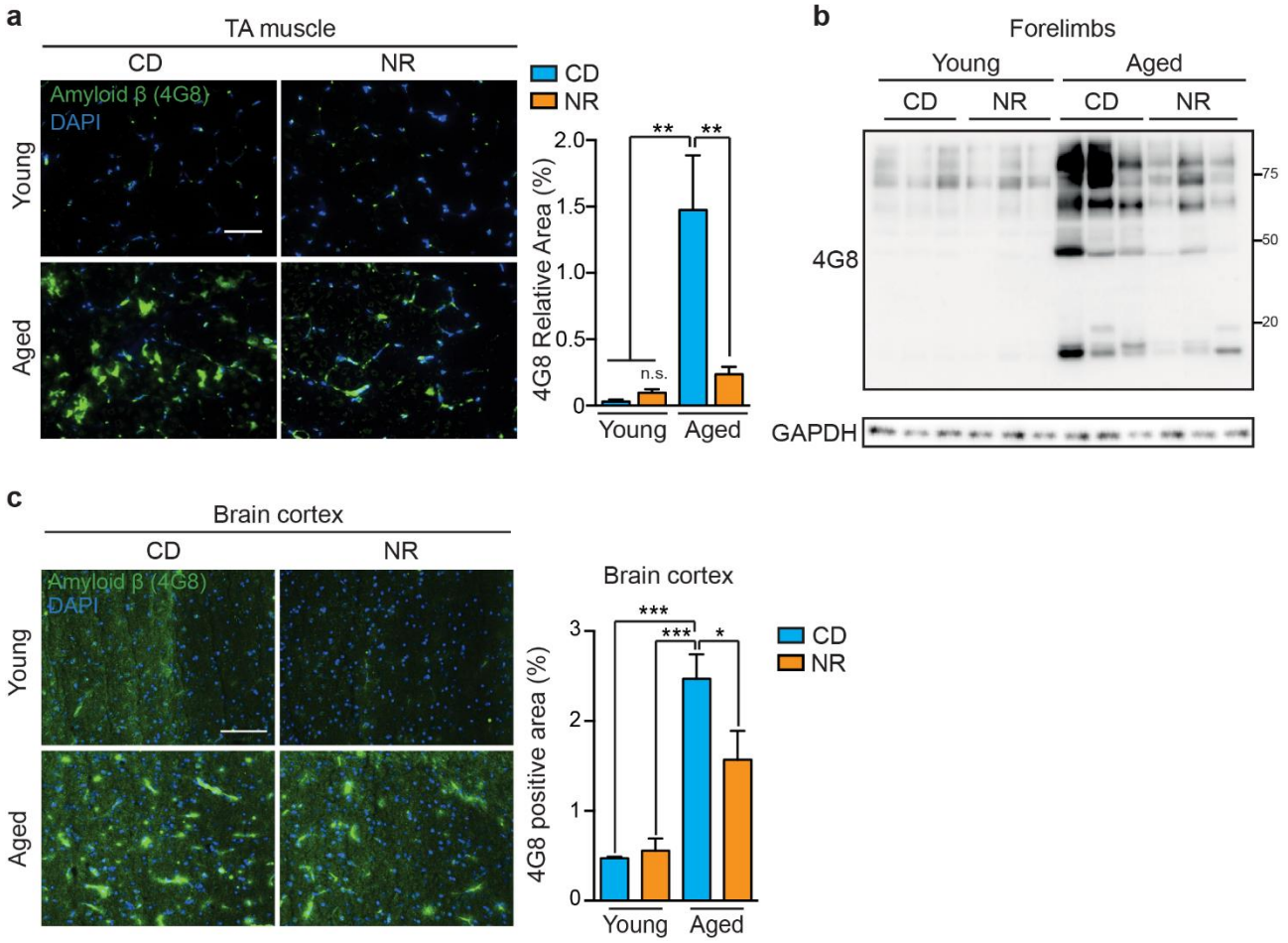

Extended Figure 3.6 | NAD⁺ boosting interventions and their effects on APP and its byproducts in vivo. a, Representative images and corresponding quantification of immunostainings of 4G8 positive protein deposits in Tibialis anterior (TA) muscles of young or aged male C57BL/6J mice, fed for 8 weeks with chow diet (CD) or chow diet supplemented with NR (400mg/kg/day) (*n* = 5-7 per group). Scale bar, 50µm. **b**, Immunoblot of 4G8 reactive proteins and byproducts from forelimb muscles of the animals in **a** (*n*=3 animals per group). **c**, Representative images and corresponding quantification of immunostainings of 4G8 positive protein deposits in brain of young or aged male C57BL/6J mice, fed for 8 weeks with chow diet (CD) or chow diet supplemented with NR (400mg/kg/day) (*n* = 5-7 per group). Scale bar, 50µm. Values in the figure are mean ± s.e.m. **P*<0.05; ***P*≤0.01; ****P*≤0.001. Differences for two groups were assessed using two-tailed *t* tests (95% confidence interval). For all the individual p values, see the **Excel data source Extended Fig. 6.**

Chapter 4

Discussion and future perspectives

Future of NAD^+ research: a land of opportunities and risks

Within the last decade the NAD^+ field has experienced a genuine scientific renaissance, resulting, as a consequence, in a general excitement around NAD^+-boosting and its therapeutic applications. Data on the beneficial effects of different approaches restoring NAD^+ content are accumulating fast with new reports appearing regularly. Although the therapeutic potential of boosting NAD^+ levels via several approaches is undeniable at the preclinical level, several issues have to be resolved in order to add a real translational value to all the research on NAD^+ that has been published until now.

A clear example of the controversy regarding the clinical use of NAD^+ boosters is represented by NR. The first trial of the natural NAD^+ booster NR in humans has been published in 2016 reporting that oral administration of NR to healthy volunteers lead to a dose-dependent increase in blood NAD^+ levels[366]. Several other studies have been completed since then and over 30 human clinical trials are currently ongoing or recruiting participants. The already published results point out that the translation from the rodent models to humans might be less straightforward than one might have expected. Indeed, while the performed studies report that different dosing and different durations of NR administration all lead to an increase in NAD^+ levels and show no serious adverse effects, the studies trying to assess the potential of NR in obesity, diabetes and aging did not show striking results so far[367,368]. Dietary supplementation with NR for 12 weeks (1000 mg twice daily) did not improve insulin sensitivity or glucose homeostasis in obese insulin-resistant men[367]; it also had no effects on β-cell function and on the levels of circulating bile acids and adipsin[368]. Despite these somehow disappointing outcomes of the first clinical trials, a few points require consideration. First, the doses of NAD^+ precursors used (mainly 1000 mg/day) are far lower than the doses used in preclinical animal models. Second, 12 weeks in the context of a human study might appear too short for NR to show its full therapeutic impact. It is moreover relevant to consider that clinical investigation of muscle function present also other challenges, such as incontrollable physiological status of the skeletal muscle of the participants, a potentially important cofounder, as NAD^+ levels in muscle tissue are strongly affected by exercise, which was shown to increase NAMPT activity restoring NAD^+ in aged rodents and humans[369–371]. In addition, another cofounding effect is the presence of sarcopenic individuals in the studies performed; indeed, a recent study showed that sarcopenia is accompanied by a decrease in NAD^+ biosynthesis and recycling[372]. It is furthermore important to mention that reduced levels of circulating inflammatory cytokines observed in aged subjects after 21 day of NR supplementation[373], as well as the trend in blood pressure reduction detected in patients after a 6 week NR treatment[374] look rather positive, as hypertension and meta-inflammation are important risk factors for cardiometabolic and neurodegenerative diseases.

In order to accomplish the leap from the bench to bedside, carefully planned clinical studies of longer duration and with higher doses, involving large number of patients should be performed. However, at this point the natural origin of NAD^+ precursors comes into play. Indeed, NAD^+ precursors as vitamins present a double-edged sword. On the one hand their use does not require Food and Drug Administration (FDA) approval, which significantly simplifies studies and sales of these compounds by the nutraceutical industry as food supplements. Large numbers of people are hence taking such supplements and side effects from this consumption, beyond the boundaries of clinical trials, go often unnoticed and are not reported. On the other hand, since NR, NA, NMN and NAM are all natural products, the

biopharmaceutical industry is hesitant to invest the important amounts of money required for large clinical trials in the setting of diseases. Consequently, the scientific and clinical community must not bend under the hype and pressure surrounding the beneficial effects of NAD^+ boosting and must by all means prevent the field from moving in the wrong direction on the basis of insufficient clinical evidence.

Even the knowledge of basic NAD^+ biology remains unexpectedly incomplete. Most published studies aiming to modulate NAD^+ metabolism have focused exclusively on measuring NAD^+ concentrations, unfortunately often with non-quantitative methods. Assessment of the entire NAD^+ metabolome constitutes a much more accurate way to obtain a comprehensive footprint of the effects of NAD^+ boosting, given that NAD^+ and its related metabolites undergo constant interconversion[375]. An additional level of complexity comes from every tissue possessing its own NAD^+ metabolome, which can still be affected by cross-talk with the NAD^+ systems of other organs and gut microbiome. Measuring fluxes through pathways of NAD^+ synthesis and degradation is hence another complementary strategy to better characterize the dynamics of NAD^+ homeostasis[154]. Methods for accurate and reproducible NAD^+ quantification should be applied more carefully. Of all the currently available techniques, mass spectrometry has the greatest analytical power and delivers the most robust results[375]. Fortunately, the field is constantly evolving: for example, the development of NAD^+ biosensors might shed light on different aspects of NAD^+ homeostasis by allowing for monitoring within different subcellular compartments in intact cells[376,377]. New techniques enabling the monitoring of NAD^+ and its metabolites at the 'point of care'[378] will also become essential for fast and simple, yet accurate and reproducible NAD^+ measurements in healthy individuals as well as in people with diseases to establish whether their NAD^+ dynamics are similar to those of animal disease models.

Only with systematic progress in both basic and clinical understanding of NAD^+ biology can the exciting observations be translated from the bench to the bedside, and the preventive and therapeutic potential associated with maintaining healthful NAD^+ homeostasis be exploited. My thesis work was indeed performed with this specific goal in mind.

Amyloidosis is a feature of aging

Age associated muscle dysfunction is related to frailty, physical disability and, ultimately, mortality[379]. Hospitalization costs for individuals with severe muscle dysfunction add up to USD $40.4 billion annually in the US (2004)[380]. The over 60 years-population is constantly raising in number and is predicted to increase to 22% in the next four decades[381], hence identification of new hallmarks of the aging process would provide potential novel targets for anti-aging approaches. Aging is a multifactorial time dependent loss of homeostasis that all living organism undergo. It is characterized by the qualitative or quantitative decline in numerous processes including mitochondrial function and proteostasis[382], which leads to a decline in cellular and organismal integrity, a primary risk factor for the development of pathologies including cancer[383,384], cardiovascular disorders[385–387], diabetes[14,388] and, particularly, neuromuscular degenerative diseases[389–391]. This last group of disorders entails proteotoxic stress diseases, including the examples described in this thesis of IBM and AD. These conditions are characterized, as mentioned before, by amyloidosis. However, whether their presence in natural aging is unexplored.

The goal of my thesis was to better understand the age-dependent proteostasis collapse experienced by muscle tissue and to identify new markers of this decline in muscle homeostasis. The bioinformatics approach presented in Chapter 3 revealed a striking similar alteration of mitochondria and proteostasis gene signatures between aging and muscle diseases including dystrophies and, notably, proteinopathies such as IBM. These shared alterations, suggestive of increased protein misfolding and amyloidosis, hence may

represent a major hallmark of muscle aging and disease. Indeed, we were able to detect Aβ-like aggregates in aged muscle tissue in a cross-species manner, from worms to human, which were associated with mitochondrial and muscle dysfunction. Previous work has shown that specific aggregated proteins, displaying differential abundance in aged human muscle, have orthologues that contribute functionally to aggregation and age-associated muscle loss in nematodes[392]. Despite these examples the exact protein composition of the amyloid deposits we identified is yet to be fully characterized.

Importantly, we proved the reversible nature of Aβ-like protein aggregates. In fact, activation of the MSR at the onset of aging mediated a decrease in endogenous Aβ-like protein aggregates *in vitro* and *in vivo* in a similar fashion as previously observed in Aβ-ovexpression proteotoxic models[393]. Moreover, the same results were corroborated by using inducible *in vitro* models of Aβ proteotoxicity and providing compounds after accumulation of amyloidosis.

Although aggregated proteins have been suggested to contribute to brain aging, their association and contribution to muscle aging is still largely unknown. Overall, we have provided compelling evidence of a novel hallmark of the muscle aging process, namely accumulation of amyloid-like aggregates which is associated with mitochondrial dysfunction and contribute to muscle degeneration in aging. We propose that this abnormal proteotoxic aggregates could serve as a novel biomarker for anti-aging interventions and a new target for these approaches. Indeed, we show that known anti-aging approaches which boost mitochondrial quality control can reverse age-related proteotoxic aggregates accumulation mediating a restoration of muscle homeostasis in both nematodes and mammals. The approach used in this study for the *C. elegans* tests differs from previous work from our and other laboratories. Traditionally used protocols consist in administration of NAD^+ boosting compounds in young, developing animals, to observe beneficial effects in later stages of life cycle. Instead, we started our treatment in *C. elegans* at day 4 of adulthood, a turning point in worms' aging process during which the production of eggs is stopped and fitness starts to decline[394,395]. Moreover, we administrated NR to 2-years-old mice, mimicking the treatment of human subjects of advanced age. We predict that amyloid-like aggregates could be an important and practical readout for anti-aging interventions, such as NAD^+ boosting strategies; however, accurate clinical investigation would be needed to verify this hypothesis. Finally, taking into account our brain and muscle data we speculate that oligomeric aggregates could contribute to aging also in other tissues (e.g. kidney, pancreatic beta-cell). Accordingly, we propose amyloid-like aggregates as possible novel direct targets of new drugs or interventions aiming at improving health- and lifespan as their removal restores mitochondrial function (chapter 3) and fitness, while prolonging lifespan in worms[396]. To verify these hypothesis further pre-clinical and clinical investigation will be required.

A novel way of targeting amyloidosis

Amyloidosis is a group of multifactorial diseases typified by different pathological processes including accumulation of misfolded proteins (typically Aβ)[397,398], chronic inflammatory state[51], abnormal activation of the immune system[399] and mitochondrial dysfunction[13,400]. It has been proposed that different pathological features of amyloidosis can affect each other, thus worsening the disease progression in return. It is no surprise that different interventions have been tested to treat these conditions, each one tackling a different aspect of the diseases.

Proteotoxicity featuring impaired Aβ clearance, has been an appealing target for many years as drugs available for treatment of AD, mainly aiming at reducing Aβ accumulation, have been shown to inhibit dementia symptoms for a limited period of time. Major industrial

companies have launched large clinical trials to test the efficacy of different inhibitors of β-Site APP cleaving enzyme 1 (BACE1), which plays a central role in the production of toxic Aβ peptide. In 2016, Merck reported that treatment by verubecestat, an inhibitor of BACE1 and BACE2 enzymes involved in APP cleavage, mediated a reduction of Aβ in the cerebrospinal fluid of mild-to-moderate AD patients in a dose-dependent fashion. However, verubecestat failed to show efficacy in a phase 3 study forcing Merck to stop the clinical trial in 2017[401]. The same grim fate has been experienced by Lilly and its compound lanabecestat, whose clinical trial was stopped due to lack of efficacy[402]. These were major setbacks for AD drug development and promoted investigation of new potential targets. An example is aducanumab, a monoclonal antibody that was shown to reduce Aβ plaques in mild AD cases by selectively targeting aggregated Aβ. Also in this case, despite the promising initial results, the drug was dismissed during the phase 3 clinical trial. However, recently, FDA approved a priority review for aducanumab as some of the patients of the phase 3 clinical trial showed some beneficial outcomes, giving some hope for this treatment. In the same frame, a clinical trial has been recently launched, using the heat shock response amplifier and anti-aggregation drug Arimoclomol[403], aiming at ameliorate IBM pathology. Unfortunately, the COVID-19 pandemic impacted on this trial since many IBM patients are over 50 years of age and may have dysphagia and weakness of their respiratory muscles, and are considered therefore at high risk.
From these disappointing examples it is evident that only impacting Aβ proteotoxicity is not sufficient to counteract progression of amyloidosis.

In Chapter 2, my thesis focuses on a novel way of ameliorating proteinopathies by targeting mitochondrial dysfunction through activation of the mitochondrial quality control. In fact, we identified a cross-species MSR that characterizes mitochondria undergoing proteotoxic stress. This stress response entails key pathways involved in mitochondrial proteostasis including the UPR^{mt} and mitophagy. Importantly, MSR pathways are necessary for survival under Aβ proteotoxic stress. The discovery of a novel set of pathways involved in adaptation to this insult gave us a potential new approach to treat amyloidosis. We speculated that boosting these pathways could potentially help mitochondria to face Aβ proteotoxicity. Using mitochondrial quality control enhancers such as the mitochondrial translation inhibitor Doxycycline and the NAD^+ booster NR we were able not only to restore mitochondrial homeostasis but also ameliorate cellular proteostasis in a cross-species manner. Indeed, UPR^{mt} and mitophagy induction led to a reduction of protein aggregates from *C. elegans* to mouse models of Aβ proteotoxicity. This decrease was accompanied by a restoration of cognitive function *in vivo*.

Our approach is different from traditional treatment strategies for proteinopathies as it targets different pathological features of amyloidosis concomitantly. Yet, the exact mechanism through which mitochondrial quality control reduces Aβ accumulation and proteotoxicity is still under investigation. We have shown that APP expression is not impacted by our approach, suggesting the involvement of post-translational events:
1. *Interaction with mitochondria and MSR.* As mentioned above, Aβ can directly interact with mitochondria, on the outside as well as inside of their membranes. Enhancing mitochondrial quality control can potentially affect Aβ folding and stability. Indeed, on one side, the UPR^{mt} acting inside the mitochondria, could mediate refolding of Aβ and/or its degradation through chaperones and proteases respectively. On the other hand, mitochondria which are strongly damaged by Aβ proteotoxic stress could undergo mitophagy with consequent digestion of misfolded proteins.
2. *Cytosolic stress responses*. Cytoplasmic protein quality control is another group of stress responses pivotal in facing proteotoxic stress, which is tightly linked to mitochondrial stress pathways. Crucial components of the cytoplasmic proteostasis mechanisms are the heat

shock response (HSR) and the autophagy process. Despite acting in different cellular organelles, cross-talk between the stress response in different cell compartments ensures an orchestrated activation of these proteostatic pathways, providing an efficient response to proteotoxic stress at the cellular level[311,314,404,405]. In particular, perturbation of mitochondrial function through alteration of lipid metabolism or impairment of mitochondrial chaperone HSP70 can activate the UPR^{mt} and, consecutively, the HSR[311]. Moreover, genetically induced mitochondrial stress is also able to preserve the HSR during aging, whose efficacy would otherwise gradually fade in adulthood[406]. Therefore, we could speculate that boosting mitochondrial quality control would in return activate the cytoplasmic protein surveillance promoting proteotoxic aggregates removal through chaperones along with digestion through lysosomes. Moreover, mitochondrial proteostatic pathways also play a crucial role in mediating ER stress response and vice versa[405,407]. Key regulators of the mammalian UPR^{mt} such as eIF2α, CHOP and ATF4/5 are also pivotal UPR^{er} mediators[405,408], hence, ER defenses could also participate to restoration of cellular proteostasis.

3. *Impact on inflammation.* Finally, reduced inflammation might play a role in decreasing Aβ proteotoxicity by normalizing microglial response. Different groups independently replicated our data on Aβ load diminution using mitochondrial quality control boosting compounds with a concomitant improvement of the inflammatory status. In particular, mitophagy activation reduced Aβ aggregates content with a concomitant reduction in the production of several key pro-inflammatory cytokines, including interleukin-6 and tumor necrosis factor-α and a normalization of microglial activity[409,410]. Moreover, doxycycline treatment of AD mice shown an improvement in cognitive function which was associated with a lower neuroinflammation[411].

Our work and research from other groups are currently bringing a new perspective to the field of amyloid disease and consequently promoted investment in new clinical trials aiming at restoring mitochondrial function to ameliorate proteinopathies. Rapamycin and pioglitazone, two compounds known for their beneficial effect on mitochondria, are currently being tested in IBM patients[412,413]; while NA and NR are under investigation as potential treatments for neurodegenerative diseases, such as AD and PD[414–417]. Indeed, the anti-aggregation properties of mitochondrial quality control boosters have also been proved in proteinopathies not involving Aβ such as PD[352] and ALS[418], potentially expanding the application of such interventions to a wider panel of diseases characterized by misfolded proteins.

Chapter 5

Curriculum Vitae

Mario Romani

romani.mario.rm@gmail.com, +41762041723

Avenue de la Gare 69C, 1022 Chavannes-pres-Renens

Education

Ph.D. in Biotechnology and Bioengineering, 2021
École polytechnique fédérale de Lausanne (EPFL), Switzerland

M.Sc in Pharmaceutical Biotecnology, 2016
Alma Mater Studiorum, Università di Bologna

B.Sc in Biological Sciences, 2014
Alma Mater Studiorum, Università di Bologna

Research experience

Laboratory of Integrative System Physiology - Nestlè chair energy metabolism, École polytechnique fédérale de Lausanne (EPFL), Switzerland, 2017-2021
Ph.D. thesis under the supervision of Prof. Johan Auwerx "Enhancing mitochondrial quality control to fight neuro-muscolar degeneration in aging and disease"

Laboratory of Integrative System Physiology - Nestlè chair energy metabolism, École polytechnique fédérale de Lausanne (EPFL), Switzerland, 2016
Master thesis under the supervision of Prof. Johan Auwerx "Testing a new assessment of NAD+ boosters and their novel physiological role"

Department of Pharmacy & Biotechnology, Alma mater studiorum University Bologna, Italy, 2014
Bachelor thesis under the supervision of Prof. Moreno Paolini "Modulation of the "Drug metabolism" enzymes in the Sprague Dawley rats in anti-oxidant key through the administration of Raphanus Sativus sprouts extract"

Publications

Romani M*, Sorrentino V*, Oh C-M*, Li H, Zhang H, Shong M, Auwerx J. NAD+ boosting reduces age-associated amyloidosis and restores mitochondrial homeostasis in muscle. *Cell reports* Jan 19;34(3):108660

Romani M, Hofer DC, Katsyuba E, Auwerx J. Niacin: an old lipid drug in a new NAD+ dress. *J. Lipid Res.* 2019. 552:187-193

Sorrentino V, Romani M, Mouchiroud L, Beck JS, Zhang H, D'Amico D, Moullan N, Potenza F, Schmid AW, Rietsch S, Counts SE, Auwerx J. Enhancing mitochondrial proteostasis reduces amyloid-β proteotoxicityy. *Nature* 2017. 552:187-193

D'Amico D, Mottis A, Potenza F, Sorrentino V, Li H, Romani M, Lemos V, Schoonjans K, Zamboni N, Knott G, Schneider BL, Auwerx J. The RNA-Binding Protein PUM2 Impairs Mitochondrial Dynamics and Mitophagy During Aging. *Mol Cell.* 2019 Feb 21;73(4):775-787.e10.

Katsyuba E, Romani M, Hofer D, Auwerx J. NAD^+ homeostasis in health and disease. *Nature Metabolism* 2020 volume 2, pages9–31

Wohlwend M, Laurila P-P, Williams K, Romani M, Imamura de Lima T, Pattawaran P, Benegiamo G, Salonen M, Schneider BL, Lahti J, Eriksson JG, Barres R, Wisloff U, Moreira JBN, Auwerx J. The exercise-induced long noncoding RNA CYTOR promotes fast-twitch myogenesis in aging. *Science Translational Medicine* (under revision)

Scientific meetings

Protein homeostasis in health and disease, virtual meeting, 2020 (poster)

“HealthAge”, Heraklion (GR), 2019 (oral lecture)

LIMNA, Lausanne (CH), 2019 (local organiser)

SV in extensor, Lausanne (CH), 2019 (invited speaker)

“Future leadership dialogue” Novartis, Basel (CH), 2019 (meeting participant)

“FSRMM” Swiss meeting on muscle research, Magglingen (CH), 2018 (poster)

Frontiers in Metabolism: Mechanisms of Metabolic Diseases, Madison (USA), 2018 (poster)

Emerging concepts in mitochondrial biology, Rehovot (IL), 2018 (poster)

LIMNA, Lausanne (CH), 2017-2018 (poster)

References

1. The New Arthurian Encyclopedia: New edition. *CRC Press* https://www.routledge.com/The-New-Arthurian-Encyclopedia-New-edition/Lacy-Ashe-Ihle-Kalinke-Thompson/p/book/9780815323037.
2. Cormack, M. J. & PH.D, P. of R. S. M. C. *Saints and Their Cults in the Atlantic World*. (Univ of South Carolina Press, 2007).
3. Flamel, N. *Nicolas Flamel: His Exposition of the Hieroglyphicall Figures (1624)*. (Garland Pub., 1994).
4. Werner, E. T. C. (Edward T. C. *Myths and Legends of China*. (2005).
5. Gupta, B. B. *India Through the Ages*. (Niyogi Books, 2006).
6. Viña, J., Borrás, C. & Miquel, J. Theories of ageing. *IUBMB Life* **59**, 249–254 (2007).
7. Warner, H. R., Sprott, R. L., Schneider, E. L. & Butler, R. N. Modern biological theories of aging. (1987).
8. Franceschi, C., Garagnani, P., Vitale, G., Capri, M. & Salvioli, S. Inflammaging and 'Garb-aging'. *Trends in Endocrinology & Metabolism* **28**, 199–212 (2017).
9. Dufour, E. & Larsson, N.-G. Understanding aging: revealing order out of chaos. *Biochim. Biophys. Acta* **1658**, 122–132 (2004).
10. Lee, H. C. & Wei, Y. H. Mitochondrial role in life and death of the cell. *J. Biomed. Sci.* **7**, 2–15 (2000).
11. Roger, A. J., Muñoz-Gómez, S. A. & Kamikawa, R. The Origin and Diversification of Mitochondria. *Curr. Biol.* **27**, R1177–R1192 (2017).
12. Martin, W. F., Garg, S. & Zimorski, V. Endosymbiotic theories for eukaryote origin. *Philos Trans R Soc Lond B Biol Sci* **370**, (2015).
13. Rockstein, M. & Brandt, K. F. Enzyme changes in flight muscle correlated with aging and flight ability in the male housefly. *Science* **139**, 1049–1051 (1963).
14. Petersen, K. F. *et al.* Mitochondrial dysfunction in the elderly: possible role in insulin resistance. *Science* **300**, 1140–1142 (2003).
15. Beregi, E., Regius, O., Hüttl, T. & Göbl, Z. Age-related changes in the skeletal muscle cells. *Z Gerontol* **21**, 83–86 (1988).
16. Boffoli, D. *et al.* Decline with age of the respiratory chain activity in human skeletal muscle. *Biochim. Biophys. Acta* **1226**, 73–82 (1994).
17. Minet, A. D. & Gaster, M. Cultured senescent myoblasts derived from human vastus lateralis exhibit normal mitochondrial ATP synthesis capacities with correlating concomitant ROS production while whole cell ATP production is decreased. *Biogerontology* **13**, 277–285 (2012).
18. Palomero, J., Vasilaki, A., Pye, D., McArdle, A. & Jackson, M. J. Aging increases the oxidation of dichlorohydrofluorescein in single isolated skeletal muscle fibers at rest, but not during contractions. *Am. J. Physiol. Regul. Integr. Comp. Physiol.* **305**, R351-358 (2013).
19. Möller, P., Bergström, J., Fürst, P. & Hellström, K. Effect of aging on energy-rich phosphagens in human skeletal muscles. *Clin. Sci.* **58**, 553–555 (1980).

20. Möller, P. & Brandt, R. The effect of physical training in elderly subjects with special reference to energy-rich phosphagens and myoglobin in leg skeletal muscle. *Clin Physiol* **2**, 307–314 (1982).

21. Das, S. *et al.* ATP citrate lyase improves mitochondrial function in skeletal muscle. *Cell Metab.* **21**, 868–876 (2015).

22. Santanasto, A. J. *et al.* Skeletal Muscle Mitochondrial Function and Fatigability in Older Adults. *J. Gerontol. A Biol. Sci. Med. Sci.* **70**, 1379–1385 (2015).

23. Alway, S. E., Mohamed, J. S. & Myers, M. J. Mitochondria Initiate and Regulate Sarcopenia. *Exerc Sport Sci Rev* **45**, 58–69 (2017).

24. Catalán-García, M. *et al.* Mitochondrial DNA disturbances and deregulated expression of oxidative phosphorylation and mitochondrial fusion proteins in sporadic inclusion body myositis. *Clin. Sci.* **130**, 1741–1751 (2016).

25. Shepherd, G. M. & Harris, K. M. Three-dimensional structure and composition of CA3-->CA1 axons in rat hippocampal slices: implications for presynaptic connectivity and compartmentalization. *J. Neurosci.* **18**, 8300–8310 (1998).

26. Rangaraju, V., Calloway, N. & Ryan, T. A. Activity-driven local ATP synthesis is required for synaptic function. *Cell* **156**, 825–835 (2014).

27. Venkateshappa, C., Harish, G., Mahadevan, A., Srinivas Bharath, M. M. & Shankar, S. K. Elevated oxidative stress and decreased antioxidant function in the human hippocampus and frontal cortex with increasing age: implications for neurodegeneration in Alzheimer's disease. *Neurochem. Res.* **37**, 1601–1614 (2012).

28. Sastre, J. *et al.* A Ginkgo biloba extract (EGb 761) prevents mitochondrial aging by protecting against oxidative stress. *Free Radic. Biol. Med.* **24**, 298–304 (1998).

29. Navarro, A. & Boveris, A. Rat brain and liver mitochondria develop oxidative stress and lose enzymatic activities on aging. *Am. J. Physiol. Regul. Integr. Comp. Physiol.* **287**, R1244-1249 (2004).

30. Short, K. R. *et al.* Impact of aerobic exercise training on age-related changes in insulin sensitivity and muscle oxidative capacity. *Diabetes* **52**, 1888–1896 (2003).

31. Safdar, A. *et al.* Aberrant mitochondrial homeostasis in the skeletal muscle of sedentary older adults. *PLoS ONE* **5**, e10778 (2010).

32. Gill, J. F., Santos, G., Schnyder, S. & Handschin, C. PGC-1α affects aging-related changes in muscle and motor function by modulating specific exercise-mediated changes in old mice. *Aging Cell* **17**, (2018).

33. Gusdon, A. M. *et al.* Exercise increases mitochondrial complex I activity and DRP1 expression in the brains of aged mice. *Exp. Gerontol.* **90**, 1–13 (2017).

34. Steiner, J. L., Murphy, E. A., McClellan, J. L., Carmichael, M. D. & Davis, J. M. Exercise training increases mitochondrial biogenesis in the brain. *J. Appl. Physiol.* **111**, 1066–1071 (2011).

35. Scarpulla, R. C. Transcriptional paradigms in mammalian mitochondrial biogenesis and function. *Physiol. Rev.* **88**, 611–638 (2008).

36. Dillon, L. M. *et al.* Increased mitochondrial biogenesis in muscle improves aging phenotypes in the mtDNA mutator mouse. *Hum. Mol. Genet.* **21**, 2288–2297 (2012).

37. Yeo, D., Kang, C., Gomez-Cabrera, M. C., Vina, J. & Ji, L. L. Intensified mitophagy in skeletal muscle with aging is downregulated by PGC-1alpha overexpression in vivo. *Free Radic. Biol. Med.* **130**, 361–368 (2019).

38. Wenz, T. Mitochondria and PGC-1α in Aging and Age-Associated Diseases. *J Aging Res* **2011**, 810619 (2011).

39. Iismaa, S. E. *et al.* Comparative regenerative mechanisms across different mammalian tissues. *npj Regenerative Medicine* **3**, 1–20 (2018).

40. Wagner, W. *et al.* Aging and replicative senescence have related effects on human stem and progenitor cells. *PLoS ONE* **4**, e5846 (2009).

41. Zhang, H. *et al.* NAD(+) repletion improves mitochondrial and stem cell function and enhances life span in mice. *Science* **352**, 1436–43 (2016).

42. Khacho, M. *et al.* Mitochondrial dysfunction underlies cognitive defects as a result of neural stem cell depletion and impaired neurogenesis. *Hum Mol Genet* **26**, 3327–3341 (2017).

43. Carey, B. W., Finley, L. W. S., Cross, J. R., Allis, C. D. & Thompson, C. B. Intracellular α-ketoglutarate maintains the pluripotency of embryonic stem cells. *Nature* **518**, 413–416 (2015).

44. Trifunovic, A. *et al.* Premature ageing in mice expressing defective mitochondrial DNA polymerase. *Nature* **429**, 417–423 (2004).

45. Kujoth, G. C. *et al.* Mitochondrial DNA mutations, oxidative stress, and apoptosis in mammalian aging. *Science* **309**, 481–484 (2005).

46. Clark-Matott, J. *et al.* Metabolomic Analysis of Exercise Effects in the POLG Mitochondrial DNA Mutator Mouse Brain. *Neurobiol Aging* **36**, 2972–2983 (2015).

47. Tomaru, U. *et al.* Decreased proteasomal activity causes age-related phenotypes and promotes the development of metabolic abnormalities. *Am. J. Pathol.* **180**, 963–972 (2012).

48. Lipinski, M. M. *et al.* Genome-wide analysis reveals mechanisms modulating autophagy in normal brain aging and in Alzheimer's disease. *Proc. Natl. Acad. Sci. U.S.A.* **107**, 14164–14169 (2010).

49. Tóth, M. L. *et al.* Longevity pathways converge on autophagy genes to regulate life span in Caenorhabditis elegans. *Autophagy* **4**, 330–338 (2008).

50. Powers, E. T., Morimoto, R. I., Dillin, A., Kelly, J. W. & Balch, W. E. Biological and chemical approaches to diseases of proteostasis deficiency. *Annu. Rev. Biochem.* **78**, 959–991 (2009).

51. Salminen, A., Kaarniranta, K. & Kauppinen, A. Inflammaging: disturbed interplay between autophagy and inflammasomes. *Aging (Albany NY)* **4**, 166–175 (2012).

52. Collado, M., Blasco, M. A. & Serrano, M. Cellular senescence in cancer and aging. *Cell* **130**, 223–233 (2007).

53. Harman, D. THE FREE RADICAL THEORY OF AGING: EFFECT OF AGE ON SERUM COPPER LEVELS. *J Gerontol* **20**, 151–153 (1965).

54. Crane, J. D., Devries, M. C., Safdar, A., Hamadeh, M. J. & Tarnopolsky, M. A. The effect of aging on human skeletal muscle mitochondrial and intramyocellular lipid ultrastructure. *J. Gerontol. A Biol. Sci. Med. Sci.* **65**, 119–128 (2010).

55. Short, K. R. *et al.* Decline in skeletal muscle mitochondrial function with aging in humans. *Proc. Natl. Acad. Sci. U.S.A.* **102**, 5618–5623 (2005).

56. Simmons, Z. & Specht, C. S. The neuromuscular manifestations of amyloidosis. *J Clin Neuromuscul Dis* **11**, 145–157 (2010).

57. Alzheimer's and Dementia: Global Resources. *Alzheimer's & Dementia: Global Resources* //www.alz.org/global/overview.asp (2014).

58. Kumar, A., Singh, A. & Ekavali. A review on Alzheimer's disease pathophysiology and its management: an update. *Pharmacological Reports* **67**, 195–203 (2015).

59. Callan, A., Capkun, G., Vasanthaprasad, V., Freitas, R. & Needham, M. A Systematic Review and Meta-Analysis of Prevalence Studies of Sporadic Inclusion Body Myositis. *Journal of Neuromuscular Diseases* **4**, 127–137 (2017).

60. Ivanidze, J. *et al.* Inclusion Body Myositis. *Am J Pathol* **179**, 1347–1359 (2011).

61. Greenberg, S. A. Inclusion body myositis: clinical features and pathogenesis. *Nature Reviews Rheumatology* **15**, 257–272 (2019).

62. Miller, F. W., Lamb, J. A., Schmidt, J. & Nagaraju, K. Risk Factors and Disease Mechanisms in Myositis. *Nat Rev Rheumatol* **14**, 255–268 (2018).

63. Ryman, D. C. *et al.* Symptom onset in autosomal dominant Alzheimer disease: a systematic review and meta-analysis. *Neurology* **83**, 253–260 (2014).

64. Mendez, M. F. Early-Onset Alzheimer's Disease. *Neurol Clin* **35**, 263–281 (2017).

65. Jansen, I. E. *et al.* Genome-wide meta-analysis identifies new loci and functional pathways influencing Alzheimer's disease risk. *Nature Genetics* **51**, 404–413 (2019).

66. Karch, C. M. & Goate, A. M. Alzheimer's disease risk genes and mechanisms of disease pathogenesis. *Biol Psychiatry* **77**, 43–51 (2015).

67. Akaaboune, M. *et al.* Developmental regulation of amyloid precursor protein at the neuromuscular junction in mouse skeletal muscle. *Mol. Cell. Neurosci.* **15**, 355–367 (2000).

68. Hoffmann, J., Twiesselmann, C., Kummer, M. P., Romagnoli, P. & Herzog, V. A possible role for the Alzheimer amyloid precursor protein in the regulation of epidermal basal cell proliferation. *Eur. J. Cell Biol.* **79**, 905–914 (2000).

69. Lee, Y.-H. *et al.* Amyloid precursor protein expression is upregulated in adipocytes in obesity. *Obesity (Silver Spring)* **16**, 1493–1500 (2008).

70. Puig, K. L., Swigost, A. J., Zhou, X., Sens, M. A. & Combs, C. K. Amyloid precursor protein expression modulates intestine immune phenotype. *J Neuroimmune Pharmacol* **7**, 215–230 (2012).

71. Weggen, S. & Beher, D. Molecular consequences of amyloid precursor protein and presenilin mutations causing autosomal-dominant Alzheimer's disease. *Alzheimers Res Ther* **4**, 9 (2012).

72. Patterson, B. W. *et al.* Age and Amyloid Effects on Human CNS Amyloid-Beta Kinetics. *Ann Neurol* **78**, 439–453 (2015).

73. Verdier, Y. & Penke, B. Binding sites of amyloid beta-peptide in cell plasma membrane and implications for Alzheimer's disease. *Curr. Protein Pept. Sci.* **5**, 19–31 (2004).

74. Tan, J. Z. A. & Gleeson, P. A. The trans-Golgi network is a major site for α-secretase processing of amyloid precursor protein in primary neurons. *J. Biol. Chem.* **294**, 1618–1631 (2019).

75. Tam, J. H. K., Seah, C. & Pasternak, S. H. The Amyloid Precursor Protein is rapidly transported from the Golgi apparatus to the lysosome and where it is processed into beta-amyloid. *Mol Brain* **7**, 54 (2014).

76. Resende, R., Ferreiro, E., Pereira, C. & Oliveira, C. R. ER stress is involved in Abeta-induced GSK-3beta activation and tau phosphorylation. *J. Neurosci. Res.* **86**, 2091–2099 (2008).

77. Costa, R. O., Ferreiro, E., Cardoso, S. M., Oliveira, C. R. & Pereira, C. M. F. ER stress-mediated apoptotic pathway induced by Abeta peptide requires the presence of functional mitochondria. *J. Alzheimers Dis.* **20**, 625–636 (2010).

78. Brunetti, D. *et al.* Defective PITRM1 mitochondrial peptidase is associated with Aβ amyloidotic neurodegeneration. *EMBO Mol Med* **8**, 176–190 (2016).

79. Greenfield, J. P. *et al.* Endoplasmic reticulum and trans-Golgi network generate distinct populations of Alzheimer beta-amyloid peptides. *Proc. Natl. Acad. Sci. U.S.A.* **96**, 742–747 (1999).

80. Cha, M.-Y. *et al.* Mitochondria-specific accumulation of amyloid β induces mitochondrial dysfunction leading to apoptotic cell death. *PLoS ONE* **7**, e34929 (2012).

81. Caspersen, C. *et al.* Mitochondrial Abeta: a potential focal point for neuronal metabolic dysfunction in Alzheimer's disease. *FASEB J.* **19**, 2040–2041 (2005).

82. Manczak, M. *et al.* Mitochondria are a direct site of A beta accumulation in Alzheimer's disease neurons: implications for free radical generation and oxidative damage in disease progression. *Hum. Mol. Genet.* **15**, 1437–1449 (2006).

83. Cipolat, S., Brito, O. M. de, Zilio, B. D. & Scorrano, L. OPA1 requires mitofusin 1 to promote mitochondrial fusion. *PNAS* **101**, 15927–15932 (2004).

84. Bleazard, W. *et al.* The dynamin-related GTPase Dnm1 regulates mitochondrial fission in yeast. *Nat. Cell Biol.* **1**, 298–304 (1999).

85. Cereghetti, G. M. *et al.* Dephosphorylation by calcineurin regulates translocation of Drp1 to mitochondria. *Proc Natl Acad Sci U S A* **105**, 15803–15808 (2008).

86. Itoh, K., Nakamura, K., Iijima, M. & Sesaki, H. Mitochondrial dynamics in neurodegeneration. *Trends Cell Biol.* **23**, 64–71 (2013).

87. Nogalska, A., D'Agostino, C., Terracciano, C., Engel, W. K. & Askanas, V. Impaired autophagy in sporadic inclusion-body myositis and in endoplasmic reticulum stress-provoked cultured human muscle fibers. *Am. J. Pathol.* **177**, 1377–1387 (2010).

88. Wang, X. *et al.* Amyloid-beta overproduction causes abnormal mitochondrial dynamics via differential modulation of mitochondrial fission/fusion proteins. *Proc. Natl. Acad. Sci. U.S.A.* **105**, 19318–19323 (2008).

89. Trushina, E. *et al.* Defects in mitochondrial dynamics and metabolomic signatures of evolving energetic stress in mouse models of familial Alzheimer's disease. *PLoS ONE* **7**, e32737 (2012).

90. Wang, X., Su, B., Fujioka, H. & Zhu, X. Dynamin-Like Protein 1 Reduction Underlies Mitochondrial Morphology and Distribution Abnormalities in Fibroblasts from Sporadic Alzheimer's Disease Patients. *Am J Pathol* **173**, 470–482 (2008).

91. Manczak, M., Calkins, M. J. & Reddy, P. H. Impaired mitochondrial dynamics and abnormal interaction of amyloid beta with mitochondrial protein Drp1 in neurons from patients with Alzheimer's disease: implications for neuronal damage. *Hum. Mol. Genet.* **20**, 2495–2509 (2011).

92. Wang, X. *et al.* Impaired balance of mitochondrial fission and fusion in Alzheimer's disease. *J. Neurosci.* **29**, 9090–9103 (2009).

93. Wang, X. *et al.* Amyloid-β overproduction causes abnormal mitochondrial dynamics via differential modulation of mitochondrial fission/fusion proteins. *Proc Natl Acad Sci U S A* **105**, 19318–19323 (2008).

94. Züchner, S. *et al.* Mutations in the mitochondrial GTPase mitofusin 2 cause Charcot-Marie-Tooth neuropathy type 2A. *Nat. Genet.* **36**, 449–451 (2004).

95. Alexander, C. *et al.* OPA1, encoding a dynamin-related GTPase, is mutated in autosomal dominant optic atrophy linked to chromosome 3q28. *Nat. Genet.* **26**, 211–215 (2000).

96. Anandatheerthavarada, H. K., Biswas, G., Robin, M.-A. & Avadhani, N. G. Mitochondrial targeting and a novel transmembrane arrest of Alzheimer's amyloid precursor protein impairs mitochondrial function in neuronal cells. *J. Cell Biol.* **161**, 41–54 (2003).

97. Devi, L., Prabhu, B. M., Galati, D. F., Avadhani, N. G. & Anandatheerthavarada, H. K. Accumulation of amyloid precursor protein in the mitochondrial import channels of human Alzheimer's disease brain is associated with mitochondrial dysfunction. *J. Neurosci.* **26**, 9057–9068 (2006).

98. Rhein, V. *et al.* Amyloid-beta and tau synergistically impair the oxidative phosphorylation system in triple transgenic Alzheimer's disease mice. *Proc. Natl. Acad. Sci. U.S.A.* **106**, 20057–20062 (2009).

99. Hauptmann, S. *et al.* Mitochondrial dysfunction: an early event in Alzheimer pathology accumulates with age in AD transgenic mice. *Neurobiol. Aging* **30**, 1574–1586 (2009).

100. Gillardon, F. *et al.* Proteomic and functional alterations in brain mitochondria from Tg2576 mice occur before amyloid plaque deposition. *Proteomics* **7**, 605–616 (2007).

101. Askanas, V., Alvarez, R. B. & Engel, W. K. beta-Amyloid precursor epitopes in muscle fibers of inclusion body myositis. *Ann. Neurol.* **34**, 551–560 (1993).

102. Gibson, G. E. *et al.* Reduced activities of thiamine-dependent enzymes in the brains and peripheral tissues of patients with Alzheimer's disease. *Arch. Neurol.* **45**, 836–840 (1988).

103. Beutner, G., Ruck, A., Riede, B., Welte, W. & Brdiczka, D. Complexes between kinases, mitochondrial porin and adenylate translocator in rat brain resemble the permeability transition pore. *FEBS Lett.* **396**, 189–195 (1996).

104. Zamzami, N. & Kroemer, G. The mitochondrion in apoptosis: how Pandora's box opens. *Nat. Rev. Mol. Cell Biol.* **2**, 67–71 (2001).

105. Du, H. *et al.* Cyclophilin D deficiency attenuates mitochondrial and neuronal perturbation and ameliorates learning and memory in Alzheimer's disease. *Nat. Med.* **14**, 1097–1105 (2008).

106. Du, H., Guo, L., Zhang, W., Rydzewska, M. & Yan, S. Cyclophilin D deficiency improves mitochondrial function and learning/memory in aging Alzheimer disease mouse model. *Neurobiol. Aging* **32**, 398–406 (2011).

107. Bieganowski, P. & Brenner, C. Discoveries of nicotinamide riboside as a nutrient and conserved NRK genes establish a Preiss-Handler independent route to NAD+ in fungi and humans. *Cell* **117**, 495–502 (2004).

108. Preiss, J. & Handler, P. Biosynthesis of diphosphopyridine nucleotide. I. Identification of intermediates. *The Journal of biological chemistry* **233**, 488–92 (1958).

109. Ma, X. *et al.* Nicotinamide mononucleotide adenylyltransferase uses its NAD+ substrate-binding site to chaperone phosphorylated Tau. *eLife* **9**, (2020).

110. Zhu, Y. *et al.* Nmnat restores neuronal integrity by neutralizing mutant Huntingtin aggregate-induced progressive toxicity. *PNAS* **116**, 19165–19175 (2019).

111. Zhang, S., Ma, X., Li, D. & Liu, C. Mechanistic Basis for Client Recognition and Amyloid Inhibition of NMNAT. *Biophysical Journal* **114**, 413a (2018).

112. Johnson, V. E., Stewart, W. & Smith, D. H. Axonal pathology in traumatic brain injury. *Experimental neurology* **246**, 35–43 (2013).

113. Lingor, P., Koch, J. C., Tonges, L. & Bahr, M. Axonal degeneration as a therapeutic target in the CNS. *Cell and tissue research* **349**, 289–311 (2012).

114. LoCoco, P. M. *et al.* Pharmacological augmentation of nicotinamide phosphoribosyltransferase (NAMPT) protects against paclitaxel-induced peripheral neuropathy. *Elife* **6**, (2017).

115. Ghosh, D., LeVault, K. R., Barnett, A. J. & Brewer, G. J. A reversible early oxidized redox state that precedes macromolecular ROS damage in aging nontransgenic and 3xTg-AD mouse neurons. *J. Neurosci.* **32**, 5821–5832 (2012).

116. Pieper, A. A. *et al.* Discovery of a proneurogenic, neuroprotective chemical. *Cell* **142**, 39–51 (2010).

117. De Jesus-Cortes, H. *et al.* Neuroprotective efficacy of aminopropyl carbazoles in a mouse model of Parkinson disease. *Proceedings of the National Academy of Sciences of the United States of America* **109**, 17010–5 (2012).

118. Wang, G. *et al.* P7C3 neuroprotective chemicals function by activating the rate-limiting enzyme in NAD salvage. *Cell* **158**, 1324–34 (2014).

119. Tesla, R. *et al.* Neuroprotective efficacy of aminopropyl carbazoles in a mouse model of amyotrophic lateral sclerosis. *Proceedings of the National Academy of Sciences of the United States of America* **109**, 17016–21 (2012).

120. Yin, T. C. *et al.* P7C3 neuroprotective chemicals block axonal degeneration and preserve function after traumatic brain injury. *Cell reports* **8**, 1731–40 (2014).

121. Voorhees, J. R. *et al.* (-)-P7C3-S243 Protects a Rat Model of Alzheimer's Disease From Neuropsychiatric Deficits and Neurodegeneration Without Altering Amyloid Deposition or Reactive Glia. *Biol. Psychiatry* **84**, 488–498 (2018).

122. Choi, S. H. *et al.* Combined adult neurogenesis and BDNF mimic exercise effects on cognition in an Alzheimer's mouse model. *Science* **361**, (2018).

123. Katsyuba, E. *et al.* De novo NAD + synthesis enhances mitochondrial function and improves health. *Nature* **563**, 354 (2018).

124. Palzer, L. *et al.* Alpha-Amino-Beta-Carboxy-Muconate-Semialdehyde Decarboxylase Controls Dietary Niacin Requirements for NAD+ Synthesis. *Cell Rep* **25**, 1359-1370.e4 (2018).

125. Widner, B. *et al.* Tryptophan degradation and immune activation in Alzheimer's disease. *J Neural Transm (Vienna)* **107**, 343–353 (2000).

126. Guillemin, G. J., Brew, B. J., Noonan, C. E., Takikawa, O. & Cullen, K. M. Indoleamine 2,3 dioxygenase and quinolinic acid immunoreactivity in Alzheimer's disease hippocampus. *Neuropathol. Appl. Neurobiol.* **31**, 395–404 (2005).

127. Ogawa, T. *et al.* Kynurenine pathway abnormalities in Parkinson's disease. *Neurology* **42**, 1702–1706 (1992).

128. Stoy, N. *et al.* Tryptophan metabolism and oxidative stress in patients with Huntington's disease. *J. Neurochem.* **93**, 611–623 (2005).

129. Minhas, P. S. *et al.* Macrophage de novo NAD + synthesis specifies immune function in aging and inflammation. *Nature Immunology* **20**, 50–63 (2019).

130. Ryu, D. *et al.* NAD+ repletion improves muscle function in muscular dystrophy and counters global PARylation. *Science translational medicine* **8**, 361ra139 (2016).

131. Nogalska, A., D'Agostino, C., Engel, W. K., Davies, K. J. A. & Askanas, V. Decreased SIRT1 deacetylase activity in sporadic inclusion-body myositis muscle fibers. *Neurobiol. Aging* **31**, 1637–1648 (2010).

132. Albani, D. *et al.* The SIRT1 activator resveratrol protects SK-N-BE cells from oxidative stress and against toxicity caused by alpha-synuclein or amyloid-beta (1-42) peptide. *J. Neurochem.* **110**, 1445–1456 (2009).

133. Lutz, M. I., Milenkovic, I., Regelsberger, G. & Kovacs, G. G. Distinct patterns of sirtuin expression during progression of Alzheimer's disease. *Neuromolecular Med.* **16**, 405–414 (2014).

134. Julien, C. *et al.* Sirtuin 1 reduction parallels the accumulation of tau in Alzheimer disease. *J. Neuropathol. Exp. Neurol.* **68**, 48–58 (2009).

135. Qin, W. *et al.* Calorie restriction attenuates Alzheimer's disease type brain amyloidosis in Squirrel monkeys (Saimiri sciureus). *J. Alzheimers Dis.* **10**, 417–422 (2006).

136. Marques, S. C. F. *et al.* Epigenetic regulation of BACE1 in Alzheimer's disease patients and in transgenic mice. *Neuroscience* **220**, 256–266 (2012).

137. Singh, P., Hanson, P. S. & Morris, C. M. SIRT1 ameliorates oxidative stress induced neural cell death and is down-regulated in Parkinson's disease. *BMC Neurosci* **18**, 46 (2017).

138. Mouton, P. R., Chachich, M. E., Quigley, C., Spangler, E. & Ingram, D. K. Caloric restriction attenuates amyloid deposition in middle-aged dtg APP/PS1 mice. *Neurosci. Lett.* **464**, 184–187 (2009).

139. Porquet, D. *et al.* Neuroprotective role of trans-resveratrol in a murine model of familial Alzheimer's disease. *J. Alzheimers Dis.* **42**, 1209–1220 (2014).

140. Porquet, D. *et al.* Dietary resveratrol prevents Alzheimer's markers and increases life span in SAMP8. *Age (Dordr)* **35**, 1851–1865 (2013).

141. Koo, J.-H., Kang, E.-B., Oh, Y.-S., Yang, D.-S. & Cho, J.-Y. Treadmill exercise decreases amyloid-β burden possibly via activation of SIRT-1 signaling in a mouse model of Alzheimer's disease. *Exp. Neurol.* **288**, 142–152 (2017).

142. Bonda, D. J. *et al.* The sirtuin pathway in ageing and Alzheimer disease: mechanistic and therapeutic considerations. *Lancet Neurol* **10**, 275–279 (2011).

143. Liu, D. *et al.* Nicotinamide forestalls pathology and cognitive decline in Alzheimer mice: evidence for improved neuronal bioenergetics and autophagy procession. *Neurobiology of Aging* **34**, 1564–80 (2013).

144. Zhou, M. *et al.* Neuronal death induced by misfolded prion protein is due to NAD+ depletion and can be relieved in vitro and in vivo by NAD+ replenishment. *Brain : a journal of neurology* **138**, 992–1008 (2015).

145. Buzkova, J. *et al.* Metabolomes of mitochondrial diseases and inclusion body myositis patients: treatment targets and biomarkers. *EMBO Mol Med* **10**, (2018).

146. Guse, A. H. Regulation of calcium signaling by the second messenger cyclic adenosine diphosphoribose (cADPR). *Curr. Mol. Med.* **4**, 239–248 (2004).

147. Aksoy, P., White, T. A., Thompson, M. & Chini, E. N. Regulation of intracellular levels of NAD: a novel role for CD38. *Biochemical and biophysical research communications* **345**, 1386–1392 (2006).

148. Blacher, E. *et al.* Alzheimer's disease pathology is attenuated in a CD38-deficient mouse model. *Ann. Neurol.* **78**, 88–103 (2015).

149. Dzangué-Tchoupou, G. *et al.* CD8+T-bet+ cells as a predominant biomarker for inclusion body myositis. *Autoimmunity Reviews* **18**, 325–333 (2019).

150. Durkacz, B. W., Omidiji, O., Gray, D. A. & Shall, S. (ADP-ribose)n participates in DNA excision repair. *Nature* **283**, 593–596 (1980).

151. Poirier, G. G., de Murcia, G., Jongstra-Bilen, J., Niedergang, C. & Mandel, P. Poly(ADP-ribosyl)ation of polynucleosomes causes relaxation of chromatin structure. *Proc. Natl. Acad. Sci. U.S.A.* **79**, 3423–3427 (1982).

152. Berger, N. A., Sims, J. L., Catino, D. M. & Berger, S. J. Poly(ADP-ribose) polymerase mediates the suicide response to massive DNA damage: studies in normal and DNA-repair defective cells. *Int. Symp. Princess Takamatsu Cancer Res. Fund* **13**, 219–226 (1983).

153. Bai, P. & Canto, C. The role of PARP-1 and PARP-2 enzymes in metabolic regulation and disease. *Cell metabolism* **16**, 290–5 (2012).

154. Liu, L. *et al.* Quantitative Analysis of NAD Synthesis-Breakdown Fluxes. *Cell metabolism* (2018) doi:10.1016/j.cmet.2018.03.018.

155. Mouchiroud, L. *et al.* The NAD(+)/Sirtuin Pathway Modulates Longevity through Activation of Mitochondrial UPR and FOXO Signaling. *Cell* **154**, 430–441 (2013).

156. Braidy, N. *et al.* Age related changes in NAD+ metabolism oxidative stress and Sirt1 activity in wistar rats. *PLoS One* **6**, e19194 (2011).

157. Berger, N. A. Poly(ADP-ribose) in the cellular response to DNA damage. *Radiation research* **101**, 4–15 (1985).

158. Love, S., Barber, R. & Wilcock, G. K. Increased poly(ADP-ribosyl)ation of nuclear proteins in Alzheimer's disease. *Brain* **122 (Pt 2)**, 247–253 (1999).

159. Vis, J. C. *et al.* Expression pattern of apoptosis-related markers in Huntington's disease. *Acta Neuropathol.* **109**, 321–328 (2005).

160. Kim, S. H. *et al.* Widespread increased expression of the DNA repair enzyme PARP in brain in ALS. *Neurology* **62**, 319–322 (2004).

161. McGurk, L. *et al.* Nuclear poly(ADP-ribose) activity is a therapeutic target in amyotrophic lateral sclerosis. *Acta Neuropathol Commun* **6**, 84 (2018).

162. Martire, S. *et al.* Bioenergetic Impairment in Animal and Cellular Models of Alzheimer's Disease: PARP-1 Inhibition Rescues Metabolic Dysfunctions. *J. Alzheimers Dis.* **54**, 307–324 (2016).

163. Summers, D. W., Gibson, D. A., DiAntonio, A. & Milbrandt, J. SARM1-specific motifs in the TIR domain enable NAD+ loss and regulate injury-induced SARM1 activation. *Proc. Natl. Acad. Sci. U.S.A.* **113**, E6271–E6280 (2016).

164. Essuman, K. *et al.* The SARM1 Toll/Interleukin-1 Receptor Domain Possesses Intrinsic NAD+ Cleavage Activity that Promotes Pathological Axonal Degeneration. *Neuron* **93**, 1334-1343.e5 (2017).

165. Gerdts, J., Brace, E. J., Sasaki, Y., DiAntonio, A. & Milbrandt, J. SARM1 activation triggers axon degeneration locally via NAD(+) destruction. *Science* **348**, 453–7 (2015).

166. Frederick, D. W. *et al.* Loss of NAD Homeostasis Leads to Progressive and Reversible Degeneration of Skeletal Muscle. *Cell Metab.* **24**, 269–282 (2016).

167. Harlan, B. A. *et al.* Evaluation of the NAD+ biosynthetic pathway in ALS patients and effect of modulating NAD+ levels in hSOD1-linked ALS mouse models. *Experimental Neurology* **327**, 113219 (2020).

168. Araki, T., Sasaki, Y. & Milbrandt, J. Increased nuclear NAD biosynthesis and SIRT1 activation prevent axonal degeneration. *Science* **305**, 1010–3 (2004).

169. Yoshino, J., Mills, K. F., Yoon, M. J. & Imai, S. Nicotinamide mononucleotide, a key NAD+ intermediate, treats the pathophysiology of diet- and age-induced diabetes in mice. *Cell Metab* **14**, 528–536 (2011).

170. Lee, C. F. *et al.* Normalization of NAD+ Redox Balance as a Therapy for Heart Failure. *Circulation* **134**, 883–94 (2016).

171. Zhou, C.-C. *et al.* Hepatic NAD(+) deficiency as a therapeutic target for non-alcoholic fatty liver disease in ageing. *Br. J. Pharmacol.* **173**, 2352–2368 (2016).

172. Gariani, K. *et al.* Eliciting the mitochondrial unfolded protein response by nicotinamide adenine dinucleotide repletion reverses fatty liver disease in mice. *Hepatology* **63**, 1190–204 (2016).

173. Shi, H. *et al.* NAD Deficiency, Congenital Malformations, and Niacin Supplementation. *The New England journal of medicine* **377**, 544–552 (2017).

174. Tran, M. T. *et al.* PGC1α drives NAD biosynthesis linking oxidative metabolism to renal protection. *Nature* **531**, 528–532 (2016).

175. Houtkooper, R. H., Canto, C., Wanders, R. J. & Auwerx, J. The secret life of NAD+: an old metabolite controlling new metabolic signaling pathways. *Endocrine reviews* **31**, 194–223 (2010).

176. Yoshino, J., Baur, J. A. & Imai, S. NAD+ intermediates: The biology and therapeutic potential of NMN and NR. *Cell Metab* **27**, 513–528 (2018).

177. Imai, S. & Guarente, L. It takes two to tango: NAD+ and sirtuins in aging/longevity control. *npj Aging and Mechanisms of Disease* **2**, (2016).

178. Yang, Y., Mohammed, F. S., Zhang, N. & Sauve, A. A. Dihydronicotinamide riboside is a potent NAD+ concentration enhancer in vitro and in vivo. *J. Biol. Chem.* **294**, 9295–9307 (2019).

179. Hsu, C. P., Oka, S., Shao, D., Hariharan, N. & Sadoshima, J. Nicotinamide phosphoribosyltransferase regulates cell survival through NAD+ synthesis in cardiac myocytes. *Circulation Research* **105**, 481–91 (2009).

180. Yoshida, M. *et al.* Extracellular Vesicle-Contained eNAMPT Delays Aging and Extends Lifespan in Mice. *Cell Metab.* **30**, 329-342.e5 (2019).

181. Gardell, S. J. *et al.* Boosting NAD+ with a small molecule that activates NAMPT. *Nat Commun* **10**, 3241 (2019).

182. Sasaki, Y., Araki, T. & Milbrandt, J. Stimulation of nicotinamide adenine dinucleotide biosynthetic pathways delays axonal degeneration after axotomy. *J Neurosci* **26**, 8484–91 (2006).

183. Williams, P. A. *et al.* Vitamin B3 modulates mitochondrial vulnerability and prevents glaucoma in aged mice. *Science* **355**, 756–760 (2017).

184. Diaz-Ruiz, A. *et al.* Overexpression of CYB5R3 and NQO1, two NAD+-producing enzymes, mimics aspects of caloric restriction. *Aging Cell* **17**, e12767 (2018).

185. Khadka, D. *et al.* Augmentation of NAD+ levels by enzymatic action of NAD(P)H quinone oxidoreductase 1 attenuates adriamycin-induced cardiac dysfunction in mice. *J. Mol. Cell. Cardiol.* **124**, 45–57 (2018).

186. Kim, H.-J. *et al.* Augmentation of NAD(+) by NQO1 attenuates cisplatin-mediated hearing impairment. *Cell Death Dis* **5**, e1292 (2014).

187. Nazari Soltan Ahmad, S. *et al.* Dunnione protects against experimental cisplatin-induced nephrotoxicity by modulating NQO1 and NAD+ levels. *Free Radic. Res.* **52**, 808–817 (2018).

188. Oh, G.-S. *et al.* Pharmacological activation of NQO1 increases NAD^+ levels and attenuates cisplatin-mediated acute kidney injury in mice. *Kidney Int.* **85**, 547–560 (2014).

189. Pandit, A. *et al.* Dunnione ameliorates cisplatin-induced small intestinal damage by modulating NAD(+) metabolism. *Biochem. Biophys. Res. Commun.* **467**, 697–703 (2015).

190. Shen, A. *et al.* NAD+ augmentation ameliorates acute pancreatitis through regulation of inflammasome signalling. *Sci Rep* **7**, 3006 (2017).

191. Oh, G.-S. *et al.* Increased Cellular NAD+ Level through NQO1 Enzymatic Action Has Protective Effects on Bleomycin-Induced Lung Fibrosis in Mice. *Tuberc Respir Dis (Seoul)* **79**, 257–266 (2016).

192. Son, H. J. *et al.* Induction of NQO1 and Neuroprotection by a Novel Compound KMS04014 in Parkinson's Disease Models. *J. Mol. Neurosci.* **56**, 263–272 (2015).

193. Pellicciari, R. *et al.* alpha-Amino-beta-carboxymuconate-epsilon-semialdehyde Decarboxylase (ACMSD) Inhibitors as Novel Modulators of De Novo Nicotinamide Adenine Dinucleotide (NAD(+)) Biosynthesis. *Journal of medicinal chemistry* **61**, 745–759 (2018).

194. Kraus, D. *et al.* Nicotinamide N-methyltransferase knockdown protects against diet-induced obesity. *Nature* **508**, 258–262 (2014).

195. Neelakantan, H. *et al.* Small molecule nicotinamide N-methyltransferase inhibitor activates senescent muscle stem cells and improves regenerative capacity of aged skeletal muscle. *Biochem. Pharmacol.* **163**, 481–492 (2019).

196. Neelakantan, H. *et al.* Selective and membrane-permeable small molecule inhibitors of nicotinamide N-methyltransferase reverse high fat diet-induced obesity in mice. *Biochem. Pharmacol.* **147**, 141–152 (2018).

197. Gariani, K. *et al.* Inhibiting poly ADP-ribosylation increases fatty acid oxidation and protects against fatty liver disease. *Journal of hepatology* **66**, 132–141 (2017).

198. Bai, P. *et al.* PARP-1 inhibition increases mitochondrial metabolism through SIRT1 activation. *Cell Metab.* **13**, 461–468 (2011).

199. Pirinen, E. *et al.* Pharmacological Inhibition of poly(ADP-ribose) polymerases improves fitness and mitochondrial function in skeletal muscle. *Cell metabolism* **19**, 1034–1041 (2014).

200. Waldman, M. *et al.* PARP-1 inhibition protects the diabetic heart through activation of SIRT1-PGC-1α axis. *Exp. Cell Res.* **373**, 112–118 (2018).

201. Wang, H. *et al.* PARP-1 inhibition attenuates cardiac fibrosis induced by myocardial infarction through regulating autophagy. *Biochem. Biophys. Res. Commun.* **503**, 1625–1632 (2018).

202. Xia, Q. *et al.* PARP-1 Inhibition Rescues Short Lifespan in Hyperglycemic C. Elegans And Improves GLP-1 Secretion in Human Cells. *Aging Dis* **9**, 17–30 (2018).

203. Aksoy, P. *et al.* Regulation of SIRT 1 mediated NAD dependent deacetylation: a novel role for the multifunctional enzyme CD38. *Biochemical and biophysical research communications* **349**, 353–359 (2006).

204. Barbosa, M. T. *et al.* The enzyme CD38 (a NAD glycohydrolase, EC 3.2.2.5) is necessary for the development of diet-induced obesity. *FASEB journal : official publication of the Federation of American Societies for Experimental Biology* **21**, 3629–39 (2007).

205. Boslett, J., Hemann, C., Zhao, Y. J., Lee, H. C. & Zweier, J. L. Luteolinidin Protects the Postischemic Heart through CD38 Inhibition with Preservation of NAD(P)(H). *The Journal of pharmacology and experimental therapeutics* **361**, 99–108 (2017).

206. Boslett, J., Helal, M., Chini, E. & Zweier, J. L. Genetic deletion of CD38 confers post-ischemic myocardial protection through preserved pyridine nucleotides. *J. Mol. Cell. Cardiol.* **118**, 81–94 (2018).

207. Boslett, J., Reddy, N., Alzarie, Y. A. & Zweier, J. L. Inhibition of CD38 with the Thiazoloquin(az)olin(on)e 78c Protects the Heart against Postischemic Injury. *J. Pharmacol. Exp. Ther.* **369**, 55–64 (2019).

208. Camacho-Pereira, J. *et al.* CD38 Dictates Age-Related NAD Decline and Mitochondrial Dysfunction through an SIRT3-Dependent Mechanism. *Cell metabolism* **23**, 1127–39 (2016).

209. Tarragó, M. G. *et al.* A Potent and Specific CD38 Inhibitor Ameliorates Age-Related Metabolic Dysfunction by Reversing Tissue NAD+ Decline. *Cell Metab.* **27**, 1081-1095.e10 (2018).

210. Geisler, S. *et al.* Gene therapy targeting SARM1 blocks pathological axon degeneration in mice. *J. Exp. Med.* **216**, 294–303 (2019).

211. Qin, W. *et al.* Neuronal SIRT1 activation as a novel mechanism underlying the prevention of Alzheimer disease amyloid neuropathology by calorie restriction. *The Journal of biological chemistry* **281**, 21745–54 (2006).

212. Liu, D. *et al.* Nicotinamide forestalls pathology and cognitive decline in Alzheimer mice: evidence for improved neuronal bioenergetics and autophagy procession. *Neurobiology of Aging* **34**, 1564–80 (2013).

213. Gong, B. *et al.* Nicotinamide riboside restores cognition through an upregulation of proliferator-activated receptor-γ coactivator 1α regulated β-secretase 1 degradation and mitochondrial gene expression in Alzheimer's mouse models. *Neurobiology of Aging* **34**, 1581–1588 (2013).

214. Turunc Bayrakdar, E., Uyanikgil, Y., Kanit, L., Koylu, E. & Yalcin, A. Nicotinamide treatment reduces the levels of oxidative stress, apoptosis, and PARP-1 activity in Abeta(1-42)-induced rat model of Alzheimer's disease. *Free radical research* **48**, 146–58 (2014).

215. Wang, X., Hu, X., Yang, Y., Takata, T. & Sakurai, T. Nicotinamide mononucleotide protects against beta-amyloid oligomer-induced cognitive impairment and neuronal death. *Brain research* **1643**, 1–9 (2016).

216. Voorhees, J. R. *et al.* (-)-P7C3-S243 Protects a Rat Model of Alzheimer's Disease From Neuropsychiatric Deficits and Neurodegeneration Without Altering Amyloid Deposition or Reactive Glia. *Biol. Psychiatry* **84**, 488–498 (2018).

217. Choi, S. H. *et al.* Combined adult neurogenesis and BDNF mimic exercise effects on cognition in an Alzheimer's mouse model. *Science* **361**, (2018).

218. Zhou, M. *et al.* Neuronal death induced by misfolded prion protein is due to NAD+ depletion and can be relieved in vitro and in vivo by NAD+ replenishment. *Brain : a journal of neurology* **138**, 992–1008 (2015).

219. Stoyas, C. A. *et al.* Nicotinamide Pathway-Dependent Sirt1 Activation Restores Calcium Homeostasis to Achieve Neuroprotection in Spinocerebellar Ataxia Type 7. *Neuron* **105**, 630-644.e9 (2020).

220. Hamity, M. V. *et al.* Nicotinamide riboside, a form of vitamin B3 and NAD+ precursor, relieves the nociceptive and aversive dimensions of paclitaxel-induced peripheral neuropathy in female rats. *Pain* **158**, 962–972 (2017).

221. Trammell, S. A. *et al.* Nicotinamide Riboside Opposes Type 2 Diabetes and Neuropathy in Mice. *Scientific reports* **6**, 26933 (2016).

222. Sadanaga-Akiyoshi, F. *et al.* Nicotinamide attenuates focal ischemic brain injury in rats: with special reference to changes in nicotinamide and NAD+ levels in ischemic core and penumbra. *Neurochemical research* **28**, 1227–34 (2003).

223. Kabra, D. G., Thiyagarajan, M., Kaul, C. L. & Sharma, S. S. Neuroprotective effect of 4-amino-1,8-napthalimide, a poly(ADP ribose) polymerase inhibitor in middle cerebral artery occlusion-induced focal cerebral ischemia in rat. *Brain research bulletin* **62**, 425–33 (2004).

224. Kaundal, R. K., Shah, K. K. & Sharma, S. S. Neuroprotective effects of NU1025, a PARP inhibitor in cerebral ischemia are mediated through reduction in NAD depletion and DNA fragmentation. *Life sciences* **79**, 2293–302 (2006).

225. Feng, Y., Paul, I. A. & LeBlanc, M. H. Nicotinamide reduces hypoxic ischemic brain injury in the newborn rat. *Brain research bulletin* **69**, 117–22 (2006).

226. Zheng, C. B. *et al.* NAD(+) administration decreases ischemic brain damage partially by blocking autophagy in a mouse model of brain ischemia. *Neuroscience letters* **512**, 67–71 (2012).

227. Xie, L., Wang, Z., Li, C., Yang, K. & Liang, Y. Protective effect of nicotinamide adenine dinucleotide (NAD+) against spinal cord ischemia-reperfusion injury via reducing oxidative stress-induced neuronal apoptosis. *Journal of clinical neuroscience : official journal of the Neurosurgical Society of Australasia* **36**, 114–119 (2017).

228. Yin, T. C. *et al.* P7C3 neuroprotective chemicals block axonal degeneration and preserve function after traumatic brain injury. *Cell reports* **8**, 1731–40 (2014).

229. Demarin, V., Podobnik, S. S., Storga-Tomic, D. & Kay, G. Treatment of Alzheimer's disease with stabilized oral nicotinamide adenine dinucleotide: a randomized, double-blind study. *Drugs Exp Clin Res* **30**, 27–33 (2004).

230. Wakade, C., Chong, R., Bradley, E. & Morgan, J. C. Low-dose niacin supplementation modulates GPR109A, niacin index and ameliorates Parkinson's disease symptoms without side effects. *Clin Case Rep* **3**, 635–637 (2015).

231. Alisky, J. M. Niacin improved rigidity and bradykinesia in a Parkinson's disease patient but also caused unacceptable nightmares and skin rash--a case report. *Nutr Neurosci* **8**, 327–329 (2005).

232. Pirinen, E. *et al.* Niacin Cures Systemic NAD+ Deficiency and Improves Muscle Performance in Adult-Onset Mitochondrial Myopathy. *Cell Metab* **31**, 1078-1090.e5 (2020).

233. Phelan, M. J. Phase II Clinical Trial of Nicotinamide for the Treatment of Mild to Moderate Alzheimer's Disease. *Journal of Geriatric Medicine and Gerontology* **3**, (2017).

234. Vestergaard, E. T., Cichosz, S. L., Møller, N., Jørgensen, J. O. L. & Fleischer, J. Short-term acipimox treatment is associated with decreased cardiac parasympathetic modulation. *Br J Clin Pharmacol* **83**, 2671–2677 (2017).

235. Rubia, J. E. de la *et al.* Efficacy and tolerability of EH301 for amyotrophic lateral sclerosis: a randomized, double-blind, placebo-controlled human pilot study. *Amyotrophic Lateral Sclerosis and Frontotemporal Degeneration* **0**, 1–8 (2019).

236. Brunet, A. *et al.* Stress-dependent regulation of FOXO transcription factors by the SIRT1 deacetylase. *Science* **303**, 2011–5 (2004).

237. Papa, L. & Germain, D. SirT3 regulates the mitochondrial unfolded protein response. *Mol. Cell. Biol.* **34**, 699–710 (2014).

238. Meng, H. *et al.* SIRT3 Regulation of Mitochondrial Quality Control in Neurodegenerative Diseases. *Front Aging Neurosci* **11**, (2019).

239. Pagliarini, D. J. *et al.* A mitochondrial protein compendium elucidates complex I disease biology. *Cell* **134**, 112–123 (2008).

240. Anderson, S. *et al.* Sequence and organization of the human mitochondrial genome. *Nature* **290**, 457–465 (1981).

241. Nargund, A. M., Fiorese, C. J., Pellegrino, M. W., Deng, P. & Haynes, C. M. Mitochondrial and nuclear accumulation of the transcription factor ATFS-1 promotes OXPHOS recovery during the UPR(mt). *Mol. Cell* **58**, 123–133 (2015).

242. Oliveira, R. P. *et al.* Condition-adapted stress and longevity gene regulation by Caenorhabditis elegans SKN-1/Nrf. *Aging Cell* **8**, 524–541 (2009).

243. Nargund, A. M., Pellegrino, M. W., Fiorese, C. J., Baker, B. M. & Haynes, C. M. Mitochondrial Import Efficiency of ATFS-1 Regulates Mitochondrial UPR Activation. *Science* **337**, 587–590 (2012).

244. Yu, A. Y. H. & Houry, W. A. ClpP: a distinctive family of cylindrical energy-dependent serine proteases. *FEBS Lett.* **581**, 3749–3757 (2007).

245. Haynes, C. M., Yang, Y., Blais, S. P., Neubert, T. A. & Ron, D. The matrix peptide exporter HAF-1 signals a mitochondrial UPR by activating the transcription factor ZC376.7 in C. elegans. *Molecular cell* **37**, 529–40 (2010).

246. Tian, Y. *et al.* Mitochondrial stress induces chromatin reorganization to promote longevity and UPRmt. *Cell* **165**, 1197–1208 (2016).

247. Merkwirth, C. *et al.* Two Conserved Histone Demethylases Regulate Mitochondrial Stress-Induced Longevity. *Cell* **165**, 1209–1223 (2016).

248. Martinus, R. D. *et al.* Selective induction of mitochondrial chaperones in response to loss of the mitochondrial genome. *Eur. J. Biochem.* **240**, 98–103 (1996).

249. Fiorese, C. J. *et al.* The Transcription Factor ATF5 Mediates a Mammalian Mitochondrial UPR. *Curr. Biol.* **26**, 2037–2043 (2016).

250. Wang, Y. T. *et al.* Cardioprotection by the mitochondrial unfolded protein response requires ATF5. *American Journal of Physiology-Heart and Circulatory Physiology* **317**, H472–H478 (2019).

251. Teske, B. F. *et al.* CHOP induces activating transcription factor 5 (ATF5) to trigger apoptosis in response to perturbations in protein homeostasis. *Mol. Biol. Cell* **24**, 2477–2490 (2013).

252. Fusakio, M. E. *et al.* Transcription factor ATF4 directs basal and stress-induced gene expression in the unfolded protein response and cholesterol metabolism in the liver. *Mol. Biol. Cell* **27**, 1536–1551 (2016).

253. Chandalia, A. *et al.* MBX-102/JNJ39659100, a novel non-TZD selective partial PPAR-γ agonist lowers triglyceride independently of PPAR-α activation. *PPAR Res* **2009**, 706852 (2009).

254. Ding, W.-X. & Yin, X.-M. Sorting, recognition and activation of the misfolded protein degradation pathways through macroautophagy and the proteasome. *Autophagy* **4**, 141–150 (2008).

255. Haynes, C. M., Fiorese, C. J. & Lin, Y.-F. Evaluating and responding to mitochondrial dysfunction: the mitochondrial unfolded-protein response and beyond. *Trends Cell Biol.* **23**, 311–318 (2013).

256. Narendra, D. P. *et al.* PINK1 Is Selectively Stabilized on Impaired Mitochondria to Activate Parkin. *PLoS Biol* **8**, (2010).

257. Lazarou, M. *et al.* The ubiquitin kinase PINK1 recruits autophagy receptors to induce mitophagy. *Nature* **524**, 309–314 (2015).

258. Quirós, P. M., Langer, T. & López-Otín, C. New roles for mitochondrial proteases in health, ageing and disease. *Nat. Rev. Mol. Cell Biol.* **16**, 345–359 (2015).

259. Thomas, R. E., Andrews, L. A., Burman, J. L., Lin, W.-Y. & Pallanck, L. J. PINK1-Parkin pathway activity is regulated by degradation of PINK1 in the mitochondrial matrix. *PLoS Genet.* **10**, e1004279 (2014).

260. Bezawork-Geleta, A., Brodie, E. J., Dougan, D. A. & Truscott, K. N. LON is the master protease that protects against protein aggregation in human mitochondria through direct degradation of misfolded proteins. *Sci Rep* **5**, 17397 (2015).

261. Houtkooper, R. H. *et al.* Mitonuclear protein imbalance as a conserved longevity mechanism. *Nature* **497**, 451–7 (2013).

262. Palikaras, K., Lionaki, E. & Tavernarakis, N. Coordination of mitophagy and mitochondrial biogenesis during ageing in C. elegans. *Nature* **521**, 525–528 (2015).

263. Fang, E. F. *et al.* Tomatidine enhances lifespan and healthspan in C. elegans through mitophagy induction via the SKN-1/Nrf2 pathway. *Sci Rep* **7**, 46208 (2017).

264. Eisenberg, T. *et al.* Induction of autophagy by spermidine promotes longevity. *Nat. Cell Biol.* **11**, 1305–1314 (2009).

265. Ryu, D. *et al.* Urolithin A induces mitophagy and prolongs lifespan in C. elegans and increases muscle function in rodents. *Nat. Med.* **22**, 879–888 (2016).

266. Manczak, M. & Reddy, P. H. Abnormal interaction between the mitochondrial fission protein Drp1 and hyperphosphorylated tau in Alzheimer's disease neurons: implications for mitochondrial dysfunction and neuronal damage. *Hum Mol Genet* **21**, 2538–2547 (2012).

267. Noelker, C. *et al.* Heat shock protein 60: an endogenous inducer of dopaminergic cell death in Parkinson disease. *Journal of Neuroinflammation* **11**, 86 (2014).

268. Valente, E. M. *et al.* Localization of a Novel Locus for Autosomal Recessive Early-Onset Parkinsonism, PARK6, on Human Chromosome 1p35-p36. *Am J Hum Genet* **68**, 895–900 (2001).

269. Matsumine, H. *et al.* Localization of a gene for an autosomal recessive form of juvenile Parkinsonism to chromosome 6q25.2-27. *Am J Hum Genet* **60**, 588–596 (1997).

270. Bulteau, A.-L. *et al.* Dysfunction of mitochondrial Lon protease and identification of oxidized protein in mouse brain following exposure to MPTP: Implications for Parkinson disease. *Free Radical Biology & Medicine* **108**, 236–246 (2017).

271. Shirendeb, U. *et al.* Abnormal mitochondrial dynamics, mitochondrial loss and mutant huntingtin oligomers in Huntington's disease: implications for selective neuronal damage. *Human Molecular Genetics* **20**, 1438–1455 (2011).

272. Kim, J. *et al.* Mitochondrial loss, dysfunction and altered dynamics in Huntington's disease. *Human Molecular Genetics* **19**, 3919–3935 (2010).

273. Berendzen, K. M. *et al.* Neuroendocrine Coordination of Mitochondrial Stress Signaling and Proteostasis. *Cell* **166**, 1553-1563.e10 (2016).

274. Khalil, B. *et al.* PINK1-induced mitophagy promotes neuroprotection in Huntington's disease. *Cell Death & Disease* **6**, e1617–e1617 (2015).

275. Liu, S. & Lu, B. Reduction of protein translation and activation of autophagy protect against PINK1 pathogenesis in Drosophila melanogaster. *PLoS genetics* **6**, e1001237 (2010).

276. Kim, N. C. *et al.* VCP is essential for mitochondrial quality control by PINK1/Parkin and this function is impaired by VCP mutations. *Neuron* **78**, 65–80 (2013).

277. Komatsu, M., Kageyama, S. & Ichimura, Y. p62/SQSTM1/A170: physiology and pathology. *Pharmacological Research* **66**, 457–462 (2012).

278. Koo, J.-H., Kang, E.-B. & Cho, J.-Y. Resistance Exercise Improves Mitochondrial Quality Control in a Rat Model of Sporadic Inclusion Body Myositis. *Gerontology* **65**, 240–252 (2019).

279. 2020 Alzheimer's disease facts and figures. *Alzheimers Dement* (2020) doi:10.1002/alz.12068.

280. Dember, L. M. Amyloidosis-associated kidney disease. *J. Am. Soc. Nephrol.* **17**, 3458–3471 (2006).

281. Askanas, V. & Engel, W. K. Sporadic inclusion-body myositis: conformational multifactorial ageing-related degenerative muscle disease associated with proteasomal and lysosomal inhibition, endoplasmic reticulum stress, and accumulation of amyloid-β42 oligomers and phosphorylated tau. *Presse Med* **40**, e219-235 (2011).

282. Gauthier, S. *et al.* Why has therapy development for dementia failed in the last two decades? *Alzheimers Dement* **12**, 60–64 (2016).

283. Soejitno, A., Tjan, A. & Purwata, T. E. Alzheimer's Disease: Lessons Learned from Amyloidocentric Clinical Trials. *CNS Drugs* **29**, 487–502 (2015).

284. Herrup, K. *et al.* Beyond Amyloid: Getting Real about Non-Amyloid Targets in Alzheimer's Disease. *Alzheimers Dement* **9**, 452-458.e1 (2013).

285. Selfridge, J. E., E, L., Lu, J. & Swerdlow, R. H. Role of mitochondrial homeostasis and dynamics in Alzheimer's disease. *Neurobiol. Dis.* **51**, 3–12 (2013).

286. Pellegrino, M. W. & Haynes, C. M. Mitophagy and the mitochondrial unfolded protein response in neurodegeneration and bacterial infection. *BMC Biol* **13**, (2015).

287. Beck, J. S., Mufson, E. J. & Counts, S. E. Evidence for Mitochondrial UPR Gene Activation in Familial and Sporadic Alzheimer's Disease. *Curr Alzheimer Res* **13**, 610–614 (2016).

288. Mufson, E. J. *et al.* Mild Cognitive Impairment: Pathology and mechanisms. *Acta Neuropathol* **123**, 13–30 (2012).

289. Oddo, S. *et al.* Triple-transgenic model of Alzheimer's disease with plaques and tangles: intracellular Abeta and synaptic dysfunction. *Neuron* **39**, 409–421 (2003).

290. Jovaisaite, V., Mouchiroud, L. & Auwerx, J. The mitochondrial unfolded protein response, a conserved stress response pathway with implications in health and disease. *Journal of Experimental Biology* **217**, 137–143 (2014).

291. Cohen, E., Bieschke, J., Perciavalle, R. M., Kelly, J. W. & Dillin, A. Opposing activities protect against age-onset proteotoxicity. *Science* **313**, 1604–1610 (2006).

292. Link, C. D. C. elegans models of age-associated neurodegenerative diseases: lessons from transgenic worm models of Alzheimer's disease. *Exp. Gerontol.* **41**, 1007–1013 (2006).

293. McColl, G. *et al.* Utility of an improved model of amyloid-beta ($A\beta_{1-42}$) toxicity in Caenorhabditis elegans for drug screening for Alzheimer's disease. *Mol Neurodegener* **7**, 57 (2012).

294. Mouchiroud, L. *et al.* The Movement Tracker: A Flexible System for Automated Movement Analysis in Invertebrate Model Organisms. *Curr Protoc Neurosci* **77**, 8.37.1-8.37.21 (2016).

295. Prahlad, V. & Morimoto, R. I. Integrating the stress response: lessons for neurodegenerative diseases from C. elegans. *Trends Cell Biol* **19**, 52–61 (2009).

296. Benedetti, C., Haynes, C. M., Yang, Y., Harding, H. P. & Ron, D. Ubiquitin-like protein 5 positively regulates chaperone gene expression in the mitochondrial unfolded protein response. *Genetics* **174**, 229–39 (2006).

297. Wong, A., Boutis, P. & Hekimi, S. Mutations in the Clk-1 Gene of Caenorhabditis Elegans Affect Developmental and Behavioral Timing. *Genetics* **139**, 1247–1259 (1995).

298. Yang, W. & Hekimi, S. Two modes of mitochondrial dysfunction lead independently to lifespan extension in Caenorhabditis elegans. *Aging Cell* **9**, 433–447 (2010).

299. Moullan, N. *et al.* Tetracyclines disturb mitochondrial function across eukaryotic models: a call for caution in biomedical research. *Cell Rep* **10**, 1681–1691 (2015).

300. Zheng, L. *et al.* Macroautophagy-generated increase of lysosomal amyloid β-protein mediates oxidant-induced apoptosis of cultured neuroblastoma cells. *Autophagy* **7**, 1528–1545 (2011).

301. Forloni, G., Colombo, L., Girola, L., Tagliavini, F. & Salmona, M. Anti-amyloidogenic activity of tetracyclines: studies in vitro. *FEBS Letters* **487**, 404–407 (2001).

302. Costa, R., Speretta, E., Crowther, D. C. & Cardoso, I. Testing the therapeutic potential of doxycycline in a Drosophila melanogaster model of Alzheimer disease. *J Biol Chem* **286**, 41647–41655 (2011).

303. Loeb, M. B. *et al.* A randomized, controlled trial of doxycycline and rifampin for patients with Alzheimer's disease. *J Am Geriatr Soc* **52**, 381–387 (2004).

304. Quirós, P. M. *et al.* Multi-omics analysis identifies ATF4 as a key regulator of the mitochondrial stress response in mammals. *J Cell Biol* **216**, 2027–2045 (2017).

305. Münch, C. & Harper, J. W. Mitochondrial unfolded protein response controls matrix pre-RNA processing and translation. *Nature* **534**, 710–713 (2016).

306. Bao, X. R. *et al.* Mitochondrial dysfunction remodels one-carbon metabolism in human cells. *Elife* **5**, (2016).

307. Sidrauski, C., McGeachy, A. M., Ingolia, N. T. & Walter, P. The small molecule ISRIB reverses the effects of eIF2α phosphorylation on translation and stress granule assembly. *Elife* **4**, (2015).

308. Fang, E. F. *et al.* NAD+ Replenishment Improves Lifespan and Healthspan in Ataxia Telangiectasia Models via Mitophagy and DNA Repair. *Cell metabolism* **24**, 566–581 (2016).

309. Corcoran, K. A., Lu, Y., Turner, R. S. & Maren, S. Overexpression of hAPPswe Impairs Rewarded Alternation and Contextual Fear Conditioning in a Transgenic Mouse Model of Alzheimer's Disease. *Learn Mem* **9**, 243–252 (2002).

310. Cenini, G., Rüb, C., Bruderek, M. & Voos, W. Amyloid β-peptides interfere with mitochondrial preprotein import competence by a coaggregation process. *Mol Biol Cell* **27**, 3257–3272 (2016).

311. Kim, H.-E. *et al.* Lipid Biosynthesis Coordinates a Mitochondrial-to-Cytosolic Stress Response. *Cell* **166**, 1539-1552.e16 (2016).

312. Wang, X. & Chen, X. J. A Cytosolic Network Suppressing Mitochondria-Mediated Proteostatic Stress and Cell Death. *Nature* **524**, 481–484 (2015).

313. Wrobel, L. *et al.* Mistargeted mitochondrial proteins activate a proteostatic response in the cytosol. *Nature* **524**, 485–488 (2015).

314. D'Amico, D., Sorrentino, V. & Auwerx, J. Cytosolic Proteostasis Networks of the Mitochondrial Stress Response. *Trends Biochem. Sci.* **42**, 712–725 (2017).

315. Riera, C. E., Merkwirth, C., De Magalhaes Filho, C. D. & Dillin, A. Signaling Networks Determining Life Span. *Annu. Rev. Biochem.* **85**, 35–64 (2016).

316. Labbadia, J. & Morimoto, R. I. The biology of proteostasis in aging and disease. *Annu. Rev. Biochem.* **84**, 435–464 (2015).

317. D'Amico, D., Sorrentino, V. & Auwerx, J. Cytosolic Proteostasis Networks of the Mitochondrial Stress Response. *Trends Biochem. Sci.* **42**, 712–725 (2017).

318. Irvine, G. B., El-Agnaf, O. M., Shankar, G. M. & Walsh, D. M. Protein aggregation in the brain: the molecular basis for Alzheimer's and Parkinson's diseases. *Mol. Med.* **14**, 451–464 (2008).

319. Joshi, P. R. *et al.* Functional relevance of mitochondrial abnormalities in sporadic inclusion body myositis. *J Clin Neurosci* **21**, 1959–1963 (2014).

320. Askanas, V. & Engel, W. K. Sporadic inclusion-body myositis: conformational multifactorial ageing-related degenerative muscle disease associated with proteasomal and lysosomal inhibition, endoplasmic reticulum stress, and accumulation of amyloid-β42 oligomers and phosphorylated tau. *Presse Med* **40**, e219-235 (2011).

321. Benveniste, O. *et al.* Amyloid deposits and inflammatory infiltrates in sporadic inclusion body myositis: the inflammatory egg comes before the degenerative chicken. *Acta Neuropathol* **129**, 611–624 (2015).

322. Needham, M. *et al.* Prevalence of sporadic inclusion body myositis and factors contributing to delayed diagnosis. *J Clin Neurosci* **15**, 1350–1353 (2008).

323. Goodpaster, B. H. *et al.* The loss of skeletal muscle strength, mass, and quality in older adults: the health, aging and body composition study. *J. Gerontol. A Biol. Sci. Med. Sci.* **61**, 1059–1064 (2006).

324. Short, K. R. *et al.* Decline in skeletal muscle mitochondrial function with aging in humans. *PNAS* **102**, 5618–5623 (2005).

325. Husom, A. D. *et al.* Altered proteasome function and subunit composition in aged muscle. *Arch. Biochem. Biophys.* **421**, 67–76 (2004).

326. Wohlgemuth, S. E., Seo, A. Y., Marzetti, E., Lees, H. A. & Leeuwenburgh, C. Skeletal muscle autophagy and apoptosis during aging: effects of calorie restriction and life-long exercise. *Exp. Gerontol.* **45**, 138–148 (2010).

327. Ryu, D. *et al.* NAD+ repletion improves muscle function in muscular dystrophy and counters global PARylation. *Sci Transl Med* **8**, 361ra139 (2016).

328. Sergushichev, A. A. An algorithm for fast preranked gene set enrichment analysis using cumulative statistic calculation. *bioRxiv* 060012 (2016) doi:10.1101/060012.

329. Li, H. *et al.* Identifying gene function and module connections by the integration of multispecies expression compendia. *Genome Res.* **29**, 2034–2045 (2019).

330. Schmidt, J. *et al.* Interrelation of inflammation and APP in sIBM: IL-1β induces accumulation of β-amyloid in skeletal muscle. *Brain* **131**, 1228–1240 (2008).

331. Kayed, R. *et al.* Common structure of soluble amyloid oligomers implies common mechanism of pathogenesis. *Science* **300**, 486–489 (2003).

332. Sontag, E. M. *et al.* Detection of Mutant Huntingtin Aggregation Conformers and Modulation of SDS-Soluble Fibrillar Oligomers by Small Molecules. *J Huntingtons Dis* **1**, 119–132 (2012).

333. Watts, G. D. J. *et al.* Inclusion body myopathy associated with Paget disease of bone and frontotemporal dementia is caused by mutant valosin-containing protein. *Nat. Genet.* **36**, 377–381 (2004).

334. Shen, D. *et al.* Novel cell- and tissue-based assays for detecting misfolded and aggregated protein accumulation within aggresomes and inclusion bodies. *Cell Biochem. Biophys.* **60**, 173–185 (2011).

335. Laor, D. *et al.* Fibril formation and therapeutic targeting of amyloid-like structures in a yeast model of adenine accumulation. *Nat Commun* **10**, (2019).

336. Navarro, S. & Ventura, S. Fluorescent dye ProteoStat to detect and discriminate intracellular amyloid-like aggregates in Escherichia coli. *Biotechnol J* **9**, 1259–1266 (2014).

337. Sorrentino, V. *et al.* Enhancing mitochondrial proteostasis reduces amyloid-β proteotoxicity. *Nature* **552**, 187–193 (2017).

338. Zheng, L. *et al.* Macroautophagy-generated increase of lysosomal amyloid β-protein mediates oxidant-induced apoptosis of cultured neuroblastoma cells. *Autophagy* **7**, 1528–1545 (2011).

339. Kowaltowski, A. J. *et al.* Mitochondrial morphology regulates organellar Ca2+ uptake and changes cellular Ca2+ homeostasis. *FASEB J.* **33**, 13176–13188 (2019).

340. Upadhaya, A. R., Lungrin, I., Yamaguchi, H., Fändrich, M. & Thal, D. R. High-molecular weight Aβ oligomers and protofibrils are the predominant Aβ species in the native soluble protein fraction of the AD brain. *J. Cell. Mol. Med.* **16**, 287–295 (2012).

341. Condello, C., Yuan, P., Schain, A. & Grutzendler, J. Microglia constitute a barrier that prevents neurotoxic protofibrillar Aβ42 hotspots around plaques. *Nat Commun* **6**, 6176 (2015).

342. Alavez, S., Vantipalli, M. C., Zucker, D. J. S., Klang, I. M. & Lithgow, G. J. Amyloid-binding compounds maintain protein homeostasis during ageing and extend lifespan. *Nature* **472**, 226–229 (2011).

343. McColl, G. *et al.* Utility of an improved model of amyloid-beta (Aβ1-42) toxicity in Caenorhabditis elegansfor drug screening for Alzheimer's disease. *Molecular Neurodegeneration* **7**, 57 (2012).

344. D'Amico, D. *et al.* The RNA-Binding Protein PUM2 Impairs Mitochondrial Dynamics and Mitophagy During Aging. *Molecular Cell* (2019) doi:10.1016/j.molcel.2018.11.034.

345. Gomes, A. P. *et al.* Declining NAD+ Induces a Pseudohypoxic State Disrupting Nuclear-Mitochondrial Communication during Aging. *Cell* **155**, 1624–1638 (2013).

346. Mouchiroud, L. *et al.* The NAD(+)/Sirtuin Pathway Modulates Longevity through Activation of Mitochondrial UPR and FOXO Signaling. *Cell* **154**, 430–441 (2013).

347. Vrablik, T. L., Huang, L., Lange, S. E. & Hanna-Rose, W. Nicotinamidase modulation of NAD+ biosynthesis and nicotinamide levels separately affect reproductive development and cell survival in C. elegans. *Development* **136**, 3637–3646 (2009).

348. Vrablik, T. L., Wang, W., Upadhyay, A. & Hanna-Rose, W. Muscle type-specific responses to NAD+ salvage biosynthesis promote muscle function in Caenorhabditis elegans. *Developmental biology* **349**, 387–94 (2011).

349. Hasmann, M. & Schemainda, I. FK866, a highly specific noncompetitive inhibitor of nicotinamide phosphoribosyltransferase, represents a novel mechanism for induction of tumor cell apoptosis. *Cancer Res* **63**, 7436–7442 (2003).

350. Oakey, L. A. *et al.* Metabolic tracing reveals novel adaptations to skeletal muscle cell energy production pathways in response to NAD + depletion. *Wellcome Open Res* **3**, 147 (2018).

351. Houtkooper, R. H. *et al.* Mitonuclear protein imbalance as a conserved longevity mechanism. *Nature* **497**, 451–457 (2013).

352. Schöndorf, D. C. *et al.* The NAD+ Precursor Nicotinamide Riboside Rescues Mitochondrial Defects and Neuronal Loss in iPSC and Fly Models of Parkinson's Disease. *Cell Rep* **23**, 2976–2988 (2018).

353. Gong, B. *et al.* Nicotinamide riboside restores cognition through an upregulation of proliferator-activated receptor-γ coactivator 1α regulated β-secretase 1 degradation and mitochondrial gene expression in Alzheimer's mouse models. *Neurobiol. Aging* **34**, 1581–1588 (2013).

354. Fang, E. F. *et al.* Defective mitophagy in XPA via PARP-1 hyperactivation and NAD(+)/SIRT1 reduction. *Cell* **157**, 882–896 (2014).

355. Mouchiroud, L. *et al.* The Movement Tracker: A Flexible System for Automated Movement Analysis in Invertebrate Model Organisms. *Curr Protoc Neurosci* **77**, 8.37.1-8.37.21 (2016).

356. Cantó, C. *et al.* The NAD+ Precursor Nicotinamide Riboside Enhances Oxidative Metabolism and Protects against High-Fat Diet-Induced Obesity. *Cell Metabolism* **15**, 838–847 (2012).

357. Zhang, H. *et al.* NAD^+ repletion improves mitochondrial and stem cell function and enhances life span in mice. *Science* **352**, 1436–1443 (2016).

358. Teich, A. F., Patel, M. & Arancio, O. A reliable way to detect endogenous murine β-amyloid. *PLoS ONE* **8**, e55647 (2013).

359. Walther, D. M. *et al.* Widespread Proteome Remodeling and Aggregation in Aging C. elegans. *Cell* **161**, 919–932 (2015).

360. Ayyadevara, S. *et al.* Proteins that accumulate with age in human skeletal-muscle aggregates contribute to declines in muscle mass and function in Caenorhabditis elegans. *Aging (Albany NY)* **8**, 3486–3497 (2016).

361. Basisty, N. B. *et al.* Stable Isotope Labeling Reveals Novel Insights Into Ubiquitin-Mediated Protein Aggregation With Age, Calorie Restriction, and Rapamycin Treatment. *J. Gerontol. A Biol. Sci. Med. Sci.* **73**, 561–570 (2018).

362. Huang, C. *et al.* Intrinsically aggregation-prone proteins form amyloid-like aggregates and contribute to tissue aging in C. elegans. *eLife* **8**, e43059 (2019).

363. Vonk, W. I. M. *et al.* Differentiation Drives Widespread Rewiring of the Neural Stem Cell Chaperone Network. *Mol. Cell* **78**, 329-345.e9 (2020).

364. Temiz, P., Weihl, C. C. & Pestronk, A. Inflammatory myopathies with mitochondrial pathology and protein aggregates. *J. Neurol. Sci.* **278**, 25–29 (2009).

365. Alhatou, M. I., Sladky, J. T., Bagasra, O. & Glass, J. D. Mitochondrial abnormalities in dermatomyositis: characteristic pattern of neuropathology. *J. Mol. Histol.* **35**, 615–619 (2004).

366. Trammell, S. A. *et al.* Nicotinamide riboside is uniquely and orally bioavailable in mice and humans. *Nature communications* **7**, 12948 (2016).

367. Dollerup, O. L. *et al.* A randomized placebo-controlled clinical trial of nicotinamide riboside in obese men: safety, insulin-sensitivity, and lipid-mobilizing effects. *Am. J. Clin. Nutr.* **108**, 343–353 (2018).

368. Dollerup, O. L. *et al.* Effects of Nicotinamide Riboside on Endocrine Pancreatic Function and Incretin Hormones in Nondiabetic Men With Obesity. *J. Clin. Endocrinol. Metab.* **104**, 5703–5714 (2019).

369. Koltai, E. *et al.* Exercise alters SIRT1, SIRT6, NAD and NAMPT levels in skeletal muscle of aged rats. *Mech. Ageing Dev.* **131**, 21–28 (2010).

370. Costford, S. R. *et al.* Skeletal muscle NAMPT is induced by exercise in humans. *American journal of physiology. Endocrinology and metabolism* **298**, E117-26 (2010).

371. de Guia, R. M. *et al.* Aerobic and resistance exercise training reverses age-dependent decline in NAD+ salvage capacity in human skeletal muscle. *Physiol Rep* **7**, e14139 (2019).

372. Migliavacca, E. *et al.* Mitochondrial oxidative capacity and NAD+ biosynthesis are reduced in human sarcopenia across ethnicities. *Nat Commun* **10**, 5808 (2019).

373. Elhassan, Y. S. *et al.* Nicotinamide Riboside Augments the Aged Human Skeletal Muscle NAD+ Metabolome and Induces Transcriptomic and Anti-inflammatory Signatures. *Cell Rep* **28**, 1717-1728.e6 (2019).

374. Martens, C. R. *et al.* Chronic nicotinamide riboside supplementation is well-tolerated and elevates NAD+ in healthy middle-aged and older adults. *Nat Commun* **9**, 1286 (2018).

375. Trammell, S. A. & Brenner, C. Targeted, LCMS-based Metabolomics for Quantitative Measurement of NAD(+) Metabolites. *Computational and structural biotechnology journal* **4**, e201301012 (2013).

376. Cambronne, X. A. *et al.* Biosensor reveals multiple sources for mitochondrial NAD(+). *Science* **352**, 1474–7 (2016).

377. Sallin, O. *et al.* Semisynthetic biosensors for mapping cellular concentrations of nicotinamide adenine dinucleotides. *Elife* **7**, (2018).

378. Yu, Q. *et al.* A biosensor for measuring NAD + levels at the point of care. *Nature Metabolism* **1**, 1219–1225 (2019).

379. McCormick, R. & Vasilaki, A. Age-related changes in skeletal muscle: changes to life-style as a therapy. *Biogerontology* **19**, 519–536 (2018).

380. Goates, S. *et al.* Economic Impact of Hospitalizations in US Adults with Sarcopenia. *J Frailty Aging* **8**, 93–99 (2019).

381. Bloom, D. E. *et al.* Macroeconomic implications of population ageing and selected policy responses. *Lancet* **385**, 649–657 (2015).

382. Labbadia, J. & Morimoto, R. I. The biology of proteostasis in aging and disease. *Annu. Rev. Biochem.* **84**, 435–464 (2015).

383. Tomasetti, C. & Vogelstein, B. Variation in cancer risk among tissues can be explained by the number of stem cell divisions. *Science* **347**, 78–81 (2015).

384. Ames, B. N. Endogenous Oxidative DNA Damage, Aging, and Cancer. *Free Radical Research Communications* **7**, 121–128 (1989).

385. Hyman, L., Schachat, A. P., He, Q. & Leske, M. C. Hypertension, Cardiovascular Disease, and Age-Related Macular Degeneration. *Arch Ophthalmol* **118**, 351–358 (2000).

386. Csiszar, A. *et al.* Aging-induced phenotypic changes and oxidative stress impair coronary arteriolar function. *Circ. Res.* **90**, 1159–1166 (2002).

387. Jacobson, A. *et al.* Aging enhances pressure-induced arterial superoxide formation. *Am J Physiol Heart Circ Physiol* **293**, H1344–H1350 (2007).

388. Meneilly, G. S. & Elliott, T. Metabolic alterations in middle-aged and elderly obese patients with type 2 diabetes. *Diabetes Care* **22**, 112–118 (1999).

389. Baumgartner, R. N. *et al.* Epidemiology of sarcopenia among the elderly in New Mexico. *Am. J. Epidemiol.* **147**, 755–763 (1998).

390. Collier, T. J., Kanaan, N. M. & Kordower, J. H. Ageing as a primary risk factor for Parkinson's disease: evidence from studies of non-human primates. *Nat. Rev. Neurosci.* **12**, 359–366 (2011).

391. Forbes, R. B., Colville, S., Swingler, R. J. & Scottish ALS/MND Register. The epidemiology of amyotrophic lateral sclerosis (ALS/MND) in people aged 80 or over. *Age Ageing* **33**, 131–134 (2004).

392. Ayyadevara, S. *et al.* Proteins that accumulate with age in human skeletal-muscle aggregates contribute to declines in muscle mass and function in Caenorhabditis elegans. *Aging (Albany NY)* **8**, 3486–3497 (2016).

393. Sorrentino, V. *et al.* Enhancing mitochondrial proteostasis reduces amyloid-β proteotoxicity. *Nature* **552**, 187–193 (2017).

394. Herndon, L. A. *et al.* Stochastic and genetic factors influence tissue-specific decline in ageing C. elegans. *Nature* **419**, 808–814 (2002).

395. Hosono, R., Sato, Y., Aizawa, S. I. & Mitsui, Y. Age-dependent changes in mobility and separation of the nematode Caenorhabditis elegans. *Exp. Gerontol.* **15**, 285–289 (1980).

396. Alavez, S., Vantipalli, M. C., Zucker, D. J. S., Klang, I. M. & Lithgow, G. J. Amyloid-binding compounds maintain protein homeostasis during ageing and extend lifespan. *Nature* **472**, 226–229 (2011).

397. Falk, R. H., Comenzo, R. L. & Skinner, M. The systemic amyloidoses. *N. Engl. J. Med.* **337**, 898–909 (1997).

398. Sipe, J. D. Amyloidosis. *Annu. Rev. Biochem.* **61**, 947–975 (1992).

399. Yan, S. D. *et al.* Receptor-dependent cell stress and amyloid accumulation in systemic amyloidosis. *Nature Medicine* **6**, 643–651 (2000).

400. Parker, W. D., Filley, C. M. & Parks, J. K. Cytochrome oxidase deficiency in Alzheimer's disease. *Neurology* **40**, 1302–1303 (1990).

401. Egan, M. F. *et al.* Randomized Trial of Verubecestat for Mild-to-Moderate Alzheimer's Disease. *New England Journal of Medicine* **378**, 1691–1703 (2018).

402. Wessels, A. M. *et al.* Efficacy and Safety of Lanabecestat for Treatment of Early and Mild Alzheimer Disease: The AMARANTH and DAYBREAK-ALZ Randomized Clinical Trials. *JAMA Neurol* (2019) doi:10.1001/jamaneurol.2019.3988.

403. Fog, C. K. *et al.* The heat shock protein amplifier arimoclomol improves refolding, maturation and lysosomal activity of glucocerebrosidase. *EBioMedicine* **38**, 142–153 (2018).

404. Ron, D. & Walter, P. Signal integration in the endoplasmic reticulum unfolded protein response. *Nat. Rev. Mol. Cell Biol.* **8**, 519–529 (2007).

405. Senft, D. & Ronai, Z. A. UPR, autophagy, and mitochondria crosstalk underlies the ER stress response. *Trends Biochem. Sci.* **40**, 141–148 (2015).

406. Labbadia, J. *et al.* Mitochondrial stress restores the heat shock response and prevents proteostasis collapse during aging. *Cell Rep* **21**, 1481–1494 (2017).

407. Bouman, L. *et al.* Parkin is transcriptionally regulated by ATF4: evidence for an interconnection between mitochondrial stress and ER stress. *Cell Death & Differentiation* **18**, 769–782 (2011).

408. Malhotra, J. D. & Kaufman, R. J. ER Stress and Its Functional Link to Mitochondria: Role in Cell Survival and Death. *Cold Spring Harb Perspect Biol* **3**, (2011).

409. Fang, E. F. *et al.* Mitophagy inhibits amyloid-β and tau pathology and reverses cognitive deficits in models of Alzheimer's disease. *Nat. Neurosci.* **22**, 401–412 (2019).

410. Gong, Z. *et al.* Urolithin A attenuates memory impairment and neuroinflammation in APP/PS1 mice. *J Neuroinflammation* **16**, 62 (2019).

411. Balducci, C. *et al.* Doxycycline counteracts neuroinflammation restoring memory in Alzheimer's disease mouse models. *Neurobiol. Aging* **70**, 128–139 (2018).

412. Institut National de la Santé Et de la Recherche Médicale, France. *Étude de l'Effet de la Rapamycine Sur la Force Musculaire et la réponse Immunitaire au Cours de la Myosite à Inclusions: étude RAPAMI"*. https://clinicaltrials.gov/ct2/show/NCT02481453 (2019).

413. Johns Hopkins University. *An Open-Label Pilot Study of Pioglitazone in Sporadic Inclusion Body Myositis*. https://clinicaltrials.gov/ct2/show/NCT03440034 (2020).

414. Grill, J. *A Double-Blind-Randomized, Placebo-Controlled Adaptive Design Trial of Nicotinamide in Mild Cognitive Impairment Due to Alzheimer's Disease and Mild Alzheimer's Disease Dementia*. https://clinicaltrials.gov/ct2/show/NCT03061474 (2019).

415. VA Office of Research and Development. *NAPS: Niacin for Parkinsons Disease*. https://clinicaltrials.gov/ct2/show/NCT03808961 (2020).

416. Haukeland University Hospital. *A Randomized Controlled Trial of Nicotinamide Supplementation in Early Parkinson's Disease: the NOPARK Study*. https://clinicaltrials.gov/ct2/show/NCT03568968 (2020).

417. Effects of Nicotinamide Riboside on Bioenergetics and Oxidative Stress in Mild Cognitive Impairment/Alzheimer's Dementia - Full Text View - ClinicalTrials.gov. https://clinicaltrials.gov/ct2/show/NCT04430517.

418. Blacher, E. *et al.* Potential roles of gut microbiome and metabolites in modulating ALS in mice. *Nature* **572**, 474–480 (2019).